© Copyright by Weijie Wang 2015

All Rights Reserved

GAN CHARACTRIZATION BY X-RAY TECHNIQUES

A Thesis

Presented to

the Faculty of the Department of Mechanical Engineering

University of Houston

In Partial Fulfillment

of the Requirements for the Degree

Master of Science

in Mechanical Engineering

by

Weijie Wang

August 2015

GAN CHARACTERIZATION BY X-RAY TECHNIQUES

Weijie Wang

Approved:

Committee Chair, Jae Hyun Ryou,
Assistant Professor, Department of
Mechanical Engineering

Committee Members:

Li Sun, Associate Professor
Department of Mechanical
Engineering

Jiming Bao, Associate Professor
Department of Electrical and
Computer Engineering

Suresh K. Khator, Associate Dean,
Cullen College of Engineering

Pradeep Sharma, Professor and
Department Chair of Mechanical
Engineering

GAN CHARACTRIZATION BY X-RAY TECHNIQUES

An Abstract

of a

Thesis

Presented to

the Faculty of the Department of Mechanical Engineering

University of Houston

In Partial Fulfillment

of the Requirements for the Degree

Master of Science

in Mechanical Engineering

by

Weijie Wang

August 2015

Abstract

Gallium nitride (GaN) is a binary III/V direct bandgap semiconductor. In recent years, due to its unique characteristics such as hard, mechanically stable, superior carrier saturation velocity, high heat capacity, and thermal conductivity, GaN is widely applied in the advanced fabrication of bright light-emitting diodes, optoelectronics, high-power and high frequency electronic devices.

However, large differences in the coefficient of thermal expansion and lattice constant between GaN epitaxial layers and a substrate exist. These thermal mismatch and lattice mismatch lead to strain and the generation of defects in the GaN and affect the performance of the devices.

Techniques of X-ray diffraction are applied for characterization: reciprocal space mapping is applied to analyze strain and relaxation in epitaxial layers; high resolution rocking curves are applied for dislocation density calculation; and X-ray reflectivity is also applied to characterize the thickness and roughness information. For structural simulation of the GaN-based devices, software LEPTOS is applied.

Table of Contents

Page

Abstract vi
Table of Contents vii
List of Figures ix
List of Tables xii
1 INTRODUCTION 1
2 THEORY 3
2.1 Introduction to X-Rays 3
2.2 Electromagnetic radiation 3
2.3 X-Ray Spectrum 5
2.4 X-ray Scattering and the Bragg Law 8
2.5 Intensity of Bragg Reflections 15
2.5.1 Atomic Form Factors 15
2.5.2 Structure Factors 16
2.5.3 Absorption Factor 19
2.5.4 Multiplicity 21
2.5.5 Geometry Factor 22
2.5.6 Preferred Orientation 22
2.5.7 Diffracted Beam Intensity 23
2.6 Reciprocal Lattice 24
2.6.1 Definition of Reciprocal Lattice Vector 24
2.6.2 Diffraction In Reciprocal Space 26
2.7 Different Scan Techniques in X-Ray Diffraction Measurement 28
2.7.1 θ/2θ scan 28
2.7.2 Omega scan/Rocking curve 29
2.8 Reciprocal Space Mapping 31
2.8.1 Coordinates Set Up In the Reciprocal Space 31
2.8.2 Different Scan In Reciprocal Space 32
2.8.3 Accessible Region in Reciprocal Space 33

2.8.4 Reciprocal Space Mapping Measurement 34
2.8.5 Lattice Mismatch and Strain 35
2.8.6 RSM of Epitaxial Layers 37
2.9 Dislocations in Epitaxial GaN Layers 39
2.10 X-Ray Reflectivity 41
2.10.1 Refractive Index for X-Rays 41
2.10.2 Total External Reflection and Critical Angle 42
2.10.3 Reflectivity of a Single Layer 43
3 EXPERIMENT 45
3.1 Introduction of the X-Ray Diffractometer 45
3.2 Sample Description 47
3.3 HR-XRD measurement 50
3.3.1 Symmetric θ/2θ Scan 50
3.3.2 Skew Geometry Rocking Curve Measurement 50
3.3.3 RSM measurement 50
3.4 XRR Measurements 52
4 RESULTS AND DISCUSSION 53
4.1 Symmetric θ/2θ Scan 53
4.1.1 GaN on Sapphire 53
4.1.2 GaN on Si 56
4.2 Rocking Curve and Dislocation Density (DD) Calculation 58
4.3 RSM 65
4.4 Composition Simulation by XRD 71
4.5 Simulation by XRR 76
4.6 Comparison of XRD Simulation and XRR Simulation 79
5 SUMMARY 80
Reference 84

List of Figures

Page

FIG. 1-1 An example of blue LED 1

FIG. 1-2 An example of high electron mobility transistor (HEMT) 1

FIG. 2-1 Plane polarized x-ray beam travel in *x* direction 4

FIG. 2-2 X-ray spectrum of Mo with different applied voltage 6

FIG. 2-3 Atomic energy levels. Excitation and emission process 8

FIG. 2-4 Scattering of x-rays by a single electron 9

FIG. 2-5 Scattering of x-rays by a simple cubic crystal 11

FIG. 2-6 Course of the function $\sin^2 Nx/\sin^2 x$ 13

FIG. 2-7 Visualization of the Bragg equation 14

FIG. 2-8 Atomic form factors of some metallic atoms 16

FIG. 2-9 Hexagonal wurtzite unit cell structure 18

FIG. 2-10 Absorption coefficient of GaN of different energy 19

FIG. 2-11 Schematic representation of the absorption effect for a thin film sample 20

FIG. 2-12 Absorption factor A of GaN of different thickness plotted by Origin 21

FIG. 2-13 Scattering in $\{l_i\}$ frame to derive the geometry factor G 22

FIG. 2-14 XRD pattern of polycrystalline Si 24

FIG. 2-15 Transfer from crystal lattice to reciprocal lattice 26

FIG. 2-16 ($h0l$) planes in real space and ($h0l$) point in reciprocal space 27

FIG. 2-17 Visualization of Laue condition in reciprocal space 27

FIG. 2-18 Schematic representation of a θ/2θ scan 28

FIG. 2-19 θ/2θ scan pattern of GaN/AlGaN on sapphire 29

FIG. 2-20 Schematic representation of a rocking curve scan 30

FIG. 2-21 Rocking curve of Copper with and without defects 30

FIG. 2-22 Defects like mosaicity and curvature 31

FIG. 2-23 Representation of (a) symmetric θ/2θ scan, (b) rocking curve scan and
(c) asymmetric ω/2θ scan in (Q_x Q_z) plane 32

FIG. 2-24 Reciprocal space of a single atom cubic crystal 33

FIG. 2-25 Accessible region in reciprocal space 34

FIG. 2-26 Two different ways to measure RSM (a) subsequent rocking curve scan or

(b) subsequent radial scans 35
FIG. 2-27 Compressive strain induced when grow $Si_{1-x}Ge_x$ on Si 36
FIG. 2-28 Tensile strain induced when grow $Si_{1-x}C_x$ on Si 36
FIG. 2-29 Epitaxial layers in reciprocal space with fully relaxed (left) and fully strain (right) 38
FIG. 2-30 Relaxation line 39
FIG. 2-31 Tilt and twist caused by different Burger's in GaN 40
FIG. 2-32 Sketch of skew geometry x-ray diffraction, Ψ is the inclination angle 41
FIG. 2-33 Schematic representation of reflected and refracted beams for the derivation of their phase difference Δ 43
FIG. 2-34 Effect of roughness in XRR measurement 44
FIG. 3-1 Bruker D8 Diffractometer Configuration 45
FIG. 3-1 Bruker D8 Diffractometer Configuration 47
FIG. 3-3 GaN on sapphire samples 48
FIG. 3-4 Sketch of (a) Green LED (b) HEMT on sapphire structure 48
FIG. 3-5 GaN on Si samples 49
FIG. 3-6 Sketch of GaN on Si with buffer layer 49
FIG. 3-7 Accessible region for GaN in XRD Wizard 51
FIG. 3-8 Scan area in XRD Wizard 51
FIG. 4-1 θ/2θ Scan of GaN A 53
FIG. 4-2 Φ scan of (102) plane 54
FIG. 4-3 θ/2θ Scan of HEMT A 54
FIG. 4-4 θ/2θ Scan of Green LED 55
FIG. 4-5 θ/2θ Scan of HEMT B 56
FIG. 4-6 θ/2θ Scan of HEMT D 57
FIG. 4-7 θ/2θ Scan of HEMT C 58
FIG. 4-8 Rocking curve of HEMT C 002 plane 59
FIG. 4-9 FWHM plotted against Chi by Origin 60
FIG. 4-10 Comparison of 2 inch HEMT on different substrate 61
FIG. 4-11 Linear fit of: (a) GaN A (b) Green LED 61
FIG. 4-12 Linear fit of: (a) HEMT A (b) HEMT C 62

FIG. 4-13 Linear fit of: (a) HEMT B (b) HEMT D 63
FIG. 4-14 RSM of HEMT A (a) 104 (b) 002 66
FIG. 4-15 RSM of HEMT B (a) 104 (b) 002 67
FIG. 4-16 RSM of HEMT C (a) 104 (b) 002 68
FIG. 4-17 RSM of HEMT D (a) 104 (b) 002 69
FIG. 4-18 RSM of Green LED (a) 104 (b) 002 70
FIG. 4-19 Simulation result of HEMT A 71
FIG. 4-20 Simulation result of HEMT B 72
FIG. 4-21 Simulation result of HEMT C 73
FIG. 4-22 Simulation result of HEMT D 74
FIG. 4-23 Simulation result of Green LED from -3 to +1 satellite peaks 75
FIG. 4-24 XRR Simulation result of HEMT A 77
FIG. 4-25 XRR Simulation result of HEMT B 77
FIG. 4-26 XRR Simulation result of HEMT C 78
FIG. 4-27 XRR Simulation result of HEMT D 78
FIG. 5-1 Schematic structure of HEMT A 81
FIG. 5-2 Schematic structure of HEMT B 81
FIG. 5-3 Schematic structure of HEMT C 82
FIG. 5-4 Schematic structure of HEMT D 82

List of Tables

Page

Table 2-1 Normalized diffraction intensity for random orientation Si from calculation 23

Table 4-1 FWHM values for different Chi angles 59

Table 4-2 Concluded data of DD calculation 64

Table 4-3 XRD simulation compared with XRR simulation of HEMT A 79

1.Introduction

In recent years, epitaxial gallium nitride (GaN) has become a key material for the fabrication of advanced photonic components, such as ultraviolet to visible light-emitting diodes, photodiodes, transistors, etc. [1] and is a promising semiconductor for power electronics. [2] As shown in Figure 1-1 and 1-2.

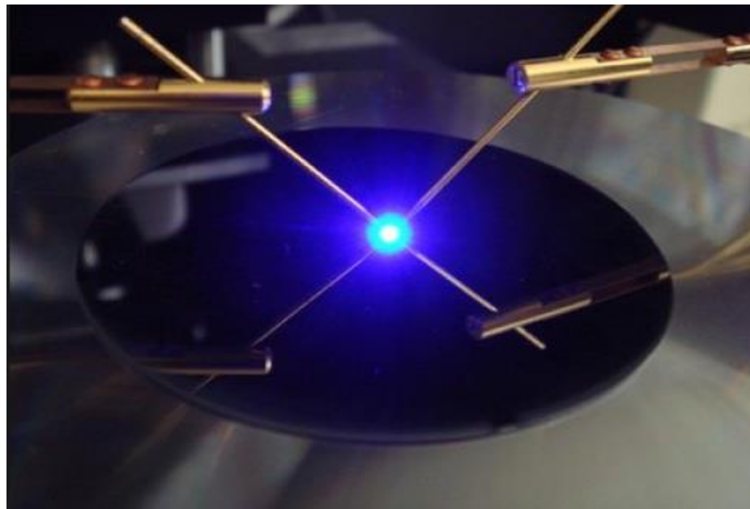

FIG. 1-1 An example of blue LED

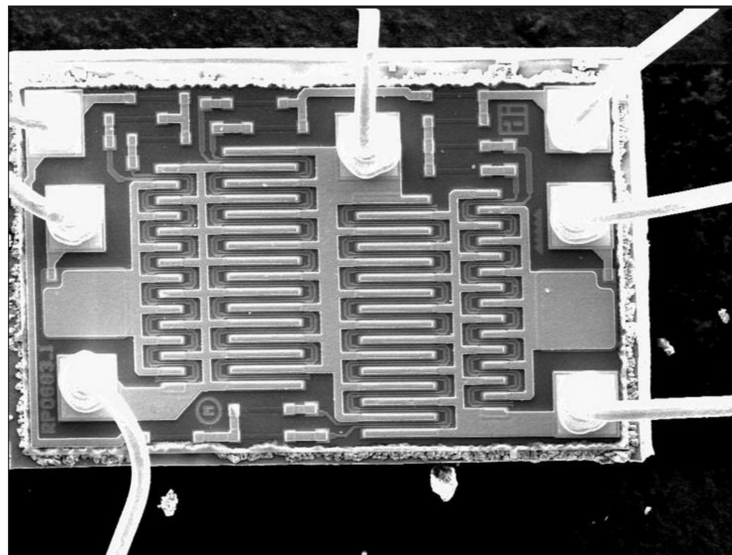

FIG. 1-2 An example of high electron mobility transistor (HEMT)

However, large differences exist in the coefficient of thermal expansion and lattice constant between GaN epitaxial layers and a substrate (Si or sapphire). [3] These thermal mismatch and lattice mismatch may lead to the generation of defects in the GaN and even cracking when the hetero-epitaxial layer and the substrate are cooled from the growth temperature to room temperature. If the strain is not relieved through thread dislocations, cracking and even a significant bowing can occur and destroy the device.

High resolution X-ray diffraction is one of the best approaches for characterization. Threading dislocation as an important type of crystal imperfection in GaN epitaxial layer can be evaluated by rocking curve measurements. GaN composed of columnar structure can be estimated by coherence length, out of plane tilt and in plane misorientations (twist), as measured by high-resolution x-ray rocking curves. Two dominant parameters of threading dislocation density are found as tilt and twist.

Reciprocal space mapping (RSM) can be applied to analyze the strain in the epitaxial layers. The effect of both strain and composition on the lattice constant is investigated.

X-ray reflectivity and simulation software Leptos are applied to analyze the detailed structure of GaN devices including green light-emitting-diodes (LED) and high-electron mobility transistors (HEMT). It is found that 6-inch-diamter GaN epitaxial layers always has a higher density of defects than 2-inch GaN layers, while 2-inch GaN epitaxial layers on different substrates will also have different crystal quality due to different buffer layer schemes.

The objective is to better understand the properties of GaN device structures and to develop evaluation methods for the optimization of these materials.

2. THEORY

2.1 Introduction of X-Rays

X-rays were first discovered in 1895 by the German physicist, Roentgen and were so named "X" because it was an unknown radiation at that time. [4] They were first applied in radiography due to its penetrating ability. The denser the object, the less x-ray can pass through. In this way the point of fracture in a broken bone or the position of a crack in a metal casting could be located. X-rays are now still wildly used in medical CT and airport security.

In 1912, the phenomenon of x-ray diffraction by crystals was discovered due to its wave properties, and provided a new method for investigating the fine structure of matter. [5] In this thesis, the wave properties of X-rays will be emphasized and both diffraction and reflection phenomenon will be used to investigate GaN related structures for LEDs and HEMTs.

2.2 Electromagnetic radiation

We know today that X-rays are electromagnetic radiation of exactly the same nature as light but of very much shorter wavelength. X-ray wavelengths are in the range of 0.5~2.5Å, while the wavelength of visible light is in the range of 4000~7000Å. [6]

Electromagnetic radiation can be considered as wave motion based on classical theory. Figure 2-1 shows a monochromatic beam of x-ray travel in *x* direction. It has an electric field **E** in *y* direction and a magnetic field **B** in z direction. If the electric field is confined to *xy*-plane as wave travel along, the wave is called plane polarized. In a

nonpolarized beam, the electric field vector **E** and the magnetic field vector **B** can be random direction in *yz* plane.

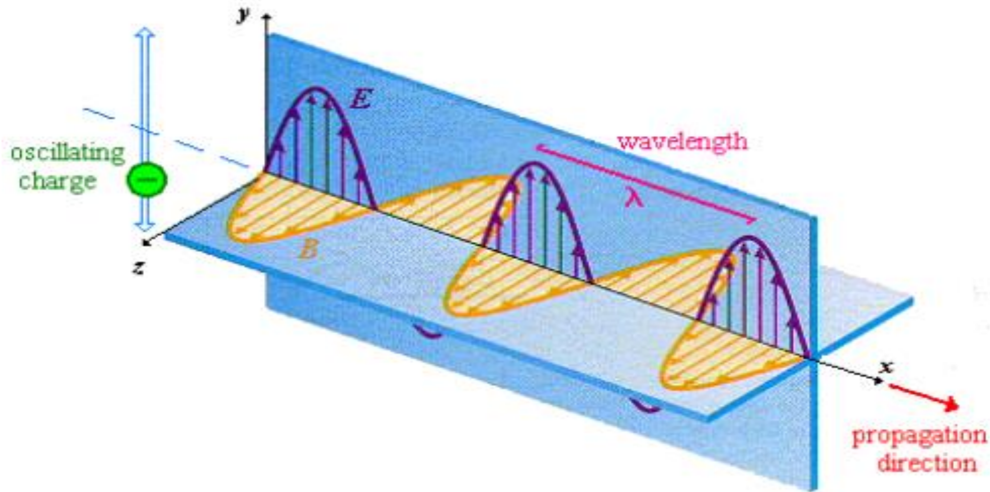

FIG 2-1. Plane polarized x-ray beam travel in *x* direction

In the plane polarized wave case, E is a function of both position *x* and time *t* and it can be expressed in one equation:

$$E = A \sin 2\pi \left(\frac{x}{\lambda} - \upsilon t\right), \tag{2-1}$$

where A = amplitude of the wave, λ = wavelength, and v = frequency. The wavelength and frequency are related by $\lambda = c/v$, where c is the velocity of light = 3.00×10^8 m/sec.

For the convenience of following calculation of x-ray scattering by electrons, atoms and unit cells, we often rewrite equation (2-1) in a different expression using Euler's formula:

$$E = E_0 e^{-i(kx-\omega t)}, \tag{2-2}$$

where $\boldsymbol{k}$ is the wave vector of magnitude $2\pi/\lambda$ and direction as the wave propagation direction, $\boldsymbol{E_0}$ is the electric field vector of magnitude A and it can assume all directions in the *yz*-plane for nonpolarized wave.

Electromagnetic radiation carries energy and the rate of flow of this energy through unit area whose normal vector is coincide with wave vector is called intensity *I,* the average value of intensity of an electromagnetic wave is proportional to the square of its amplitude, i.e., $I \propto |E_0|^2$.[8]

2.3 X-Ray Spectrum

X-rays are produced when accelerated electrons with sufficient kinetic energy collide with the target and rapidly decelerate. [9] X-rays are usually generated in x-ray tube which contains a source of electrons (most common type of laboratory x-ray source is filament tube), high accelerating voltage and a metal target. Electron beam is firstly generated by the current passing through the filament at the source. Then stable high voltage accelerates the electrons to very high velocity before it hits the target. X-rays are produced at the point of impact and radiate in all directions. The kinetic energy during this process is mostly converted to heat, that is why x-ray tube needs continuous cooling down by water flow. Only less than one percent is transferred into x-rays.

The kinetic energy is given by

$$KE = eV = \frac{1}{2}mv^2, \tag{2-3}$$

where m is the mass of the electron (9.11×10^{-28} gm) and e is the charge on the electron (1.6×10^{-19} C). V is applied voltage and v is the electron voltage before impact.

When we analyze the rays coming from of the target, plotting intensity against wavelength, it is found that x-ray consists of a mixture of different wavelengths as shown in Figure 2-2. The intensity is zero up to a certain wavelength, named short-wavelength

limit (λ_{SWL}), increases up to maximum and then decreases. When the voltage increases, the intensities of all wavelengths increase and both the short-wavelength limit and maximum position shift to shorter wavelengths. The smooth curves up to 20 kv in Figure 2-2 are called continuous radiation.

The continuous spectrum is because the electrons successively lose fractions of the total kinetic energy until it is all spent. The maximum energy of the x-ray generate when the electron lose all the energy at once in one impact and we may write

$$\lambda_{SWL} = \frac{c}{\upsilon_{max}} = \frac{hc}{eV} = \frac{12400}{V}, \quad (2\text{-}4)$$

where λ_{SWL} stands for short wavelength limit.

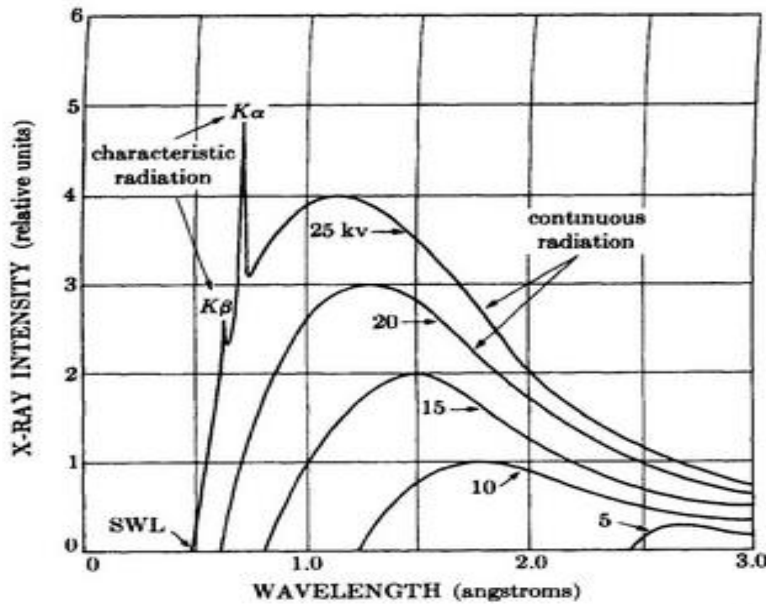

FIG 2-2 X-ray spectrum of Mo with different applied voltage

When the voltage on an x-ray tube is raised up to a certain critical value, characteristic of the target metal, sharp intensity maxima appear at certain wavelength, add on the continuous spectrum. It is called characteristic radiation.

At the critical applied voltage, the electron beam can gain enough energy to knock out the inner shell electron of the target atom and generate a hole in the inner shell (K shell), it is then filled by an electron from higher energy shell spontaneously and emit characteristic radiation with certain amount of energy. This amount of energy is the energy difference of higher energy state to K state.

Figure 2-3 shows the process of excitation and emission process of characteristic radiation, the critical voltage can be calculated as

$$eV_{crit} = W_k, \tag{2-5}$$

W_k is work required to excite and remove a K electron. The vacancy can be filled by an electron from the L-shell, produce Kα radiation, or from the M-shell, produce Kβ radiation, correspond to the two maxima in the characteristic spectrum.

The Kα radiation is a sharp line and nearly monochromatic, it can be decomposed into Kα1 and Kα2 due to slightly separated states in L shell, the energy difference is so small that the wavelength of Kα1 and Kα2 are very close (1.54056Å and 1.54439Å for Cu).

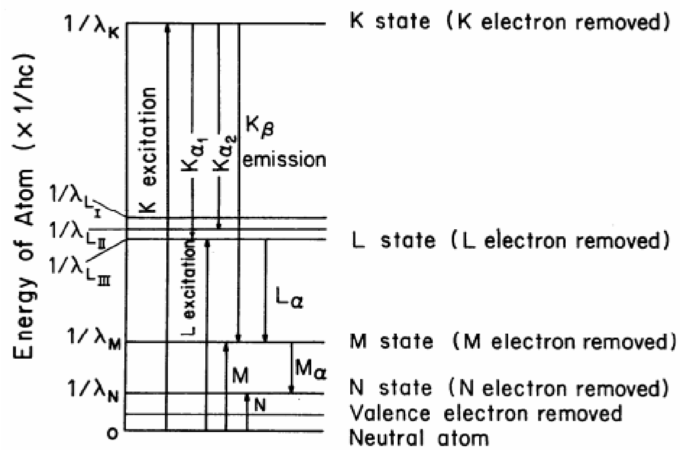

FIG. 2-3 atomic energy levels. Excitation and emission process

2.4 X-ray Scattering and the Bragg Law

After we generate the monochromatic x-ray beam of certain wavelength from the x-ray tube, we need to investigate how it will interact with matter. First, the interaction of x-rays and a single free electron is considered. Only elastic interaction is made use of in structural investigation by x-ray diffraction and this interaction is termed Thomson scattering.

Figure 2-4 illustrates the process of Thomson scattering for a single free electron of charge *e*, mass *m* and at position $\boldsymbol{R_0}$. The incoming monochromatic x-ray beam can be expressed by an electromagnetic wave as equation 2-2, (here the time effect on the field will be neglected) so it can be express simply as

$$E = E_0 e^{-iK_0 R_0}, \tag{2-6}$$

where $\boldsymbol{E_0}$ is the electric field and $\boldsymbol{K_0}$ is the incoming wave vector.

Both the incoming and exiting wave vector $\boldsymbol{K_0}$ and $\boldsymbol{K}$ have the magnitude of 2π/λ, The angle between $\boldsymbol{K}$ and the prolonged direction of $\boldsymbol{K_0}$ is the scattering angle that will be abbreviated by 2θ as is general use in x-ray diffraction.

If the amplitude of the scattered wave $\boldsymbol{E(R)}$ is considered at a distance R we may write according to Thomson [10]

$$E(R) = E_0 \frac{1}{4\pi\varepsilon_0 R} \frac{e^2}{mc^2} \sin \angle(E_0, R) e^{-iKR}, \tag{2-7}$$

where ε_0 and *c* are the vacuum permittivity and velocity of light.

The *sin* term is related on the state of polarization. Commonly laboratory x-rays are nonpolarized and E_0 can be decomposed into E_π in the scattering plane and E_σ normal to the scattering plane. In classical optics these two case are named π polarization and σ

polarization. Since the σ polarization is always perpendicular to R, the sin term is always unity. But for the π polarization, sinÐ$(E_0, R) = |cos2\theta|$. We can denote the sin term as polarization factor C and C can be written as

$$C = \begin{cases} 1 & \sigma\text{-polarization} \\ |\cos 2\theta| & \pi\text{-polarization} \end{cases}$$
.

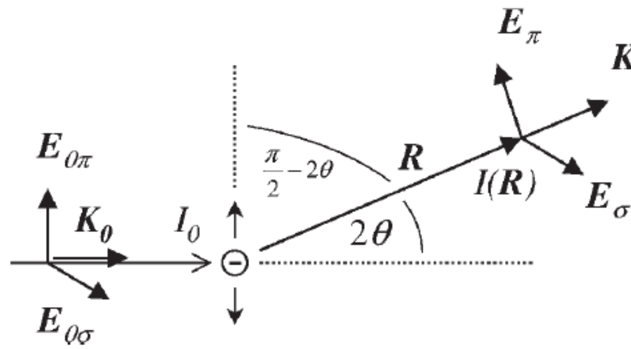

FIG. 2-4 Scattering of x-rays by a single electron

Since laboratory x-rays are often nonpolarized, meaning both polarization states will have the same probability of occurring which can be written as

$$\overline{E_\sigma^2} = \overline{E_\pi^2} = \frac{I_0}{2}, \tag{2-8}$$

and based on equation 2-7 we can calculate intensity of scattered beam at distance R as

$$I(R) = \left(\frac{1}{4\pi\varepsilon_0 R}\right)^2 \left(\frac{e^2}{mc^2}\right)^2 (E_\sigma^2 + E_\pi^2 \cos^2 2\theta), \tag{2-9}$$

and it is finally rewritten as

$$I(R) = I_0 \frac{r_e^2}{R^2} \frac{1 + \cos^2 2\theta}{2} \quad , \tag{2-10}$$

r_e is the classic radius of the electron $r_e = e^2/(4\pi\varepsilon_0 mc^2)$, the amount is 2.82×10^{-15} m. If we compare this number with laboratory setups which is of the order of 10-1m, we can neglect it. So it is almost impossible to detect that extremely small intensity.

When X-rays encounters an atom, equation 2-10 also hold for the scattering from atomic nuclei and due to larger mass of nuclei, the intensity is even smaller. So we only need to consider Z electrons in the atom. For now we just assume that Z electrons are confined to the origin of the atom and so we can substitute r_e with Zr_e in equation 2-10. Hence, we have a description of the x-ray scattering from an atom.

In the next step we need to consider what the scattering will look like if it occurs for a whole group of atoms that are arranged in a periodically ordered array like a crystal lattice. Figure 2-5 illustrates a monochromatic x-ray beam scattered by a cubic crystal. The incoming x-ray beam is parallel to the [100] direction of the crystal. In a cubic system, the atom positions can be described by the lattice vector $\mathbf{r}_{\mathbf{n_1n_2n_3}}=n_1a\mathbf{c_1}+ n_2a\mathbf{c_2}+ n_3a\mathbf{c_3}$ with c1, c2 and c3 being unit vectors of the three orthogonal directions. n_i is any integer from 0 to N_i, and *a* is the lattice constant.

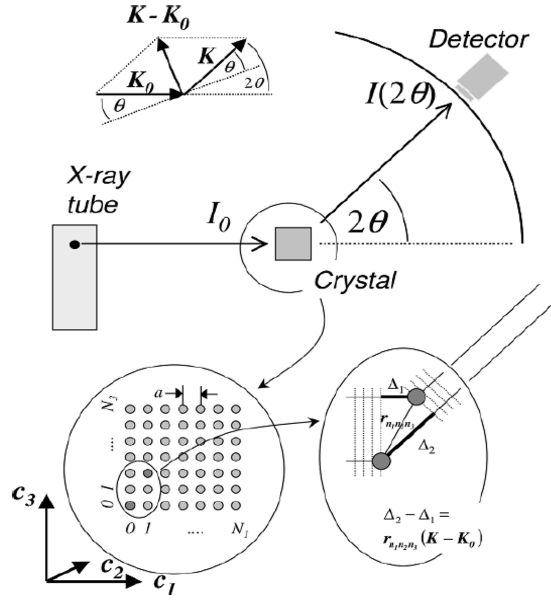

FIG. 2-5 Scattering of x-rays by a simple cubic crystal

We can take the origin of the crystal r_{000} as the reference point, and so the scattered field at point R is

$$E(R) = E_0 C \frac{Zr_e}{R} e^{-iKR}, \tag{2-11}$$

while every atoms in the crystal can be scattered by the x-rays and an atom at the point $r_{n_1n_2n_3}$ would then cause a scattering intensity to be measured at R of the strength

$$E(R) = E_0 e^{-iK_0 r_{n_1n_2n_3}} \frac{Zr_e}{\left|R - r_{n_1n_2n_3}\right|} \sin\angle(E_0, R - r_{n_1n_2n_3}) e^{-iK(R - r_{n_1n_2n_3})} \quad . \tag{2-12}$$

Because $\mathbf{r_{n_1n_2n_3}}$ (10^{-10}m) are much smaller than the distances to the point of intensity measurement $\mathbf{R\text{-}r_{n_1n_2n_3}}$ (10^{-1}m), and it can be replaced by **R** in denominator and sin term in equation 2-12.

Equation 2-12 can be rewritten as

$$E(R)=E_0\frac{Zr_e}{R}Ce^{-iKR}e^{-i(K-K_0)r_{n_1n_2n_3}}\ , \qquad (2\text{-}13)$$

and if we add up all the $N_1 \times N_2 \times N_3$ atoms in the crystal and we end up with

$$E(R)=E_0\frac{Zr_e}{R}Ce^{-iKR}\sum_{n_1n_2n_3}e^{-i(K-K_0)r_{n_1n_2n_3}}\ . \qquad (2\text{-}14)$$

We often denote (**K-K**$_0$) as scattering vector **Q** and it has a magnitude of $4\pi\sin\theta/\lambda$, and we can rewrite the summation term in equation (2-14) and the field amplitude of the scattered beam is proportional to

$$\sum_{n_1=0}^{N_1-1}\sum_{n_2=0}^{N_2-1}\sum_{n_3=0}^{N_3-1}e^{-iQ(n_1ac_1+n_2ac_2+n_3ac_3)}\ . \qquad (2\text{-}15)$$

This expression can be converted by evaluating each of the three terms by the formula of the geometric sum and we get the so-called interference function

$$\zeta(Q)=\frac{\sin^2(N_1aQc_1/2)}{\sin^2(aQc_1/2)}\cdot\frac{\sin^2(N_2aQc_2/2)}{\sin^2(aQc_2/2)}\cdot\frac{\sin^2(N_3aQc_3/2)}{\sin^2(aQc_3/2)}\ , \qquad (2\text{-}16)$$

where the course of the function $\sin^2 Nx/\sin^2 x$ is illustrated in Figure 2-6.

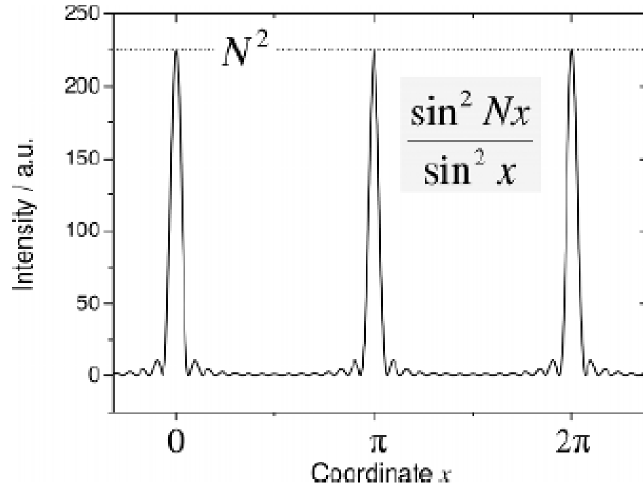

FIG. 2-6 Course of the function $\sin^2 Nx/\sin^2 x$

According to this figure we can find that only when x is integral multiples of π, the function reach its maximum of N^2. So, the necessary condition to realize the highest intensity at R according is

$$\varsigma(Q) \rightarrow max \Leftrightarrow \begin{cases} aQc_1 = 2\pi h \\ aQc_2 = 2\pi k, \\ aQc_3 = 2\pi l \end{cases} \tag{2-17}$$

where h, k, l are arbitrary integers.

The relation between lattice vector $\mathbf{r}_{\mathbf{n_1 n_2 n_3}}$ and scattering vector $\boldsymbol{Q}$ for constructive interference condition in equation (2-17) was derived by M. von Laue, and this equation is so also called the Laue condition.

We can rewrite the Laue condition and obtain

$$I(R) \rightarrow \max \Leftrightarrow \frac{|Q|}{2\pi} = \frac{\sqrt{h^2+k^2+l^2}}{a} \,. \tag{2-18}$$

Since the magnitude of Q is 4πsinθ/λ and we can finally get

$$I(R) \rightarrow \max \Leftrightarrow 2\frac{a}{\sqrt{h^2+k^2+l^2}}\sin\theta = \lambda \Leftrightarrow 2d_{hkl}\sin\theta = \lambda \,, \tag{2-19}$$

where d_{hkl} is the interplanar spacing of (hkl) plane. This equation is called Bragg equation and was applied by W.H. Bragg and W.L. Bragg in 1913 to describe the position of x-ray scattering peaks in angular space.

Both the Laue condition and the Bragg equation describe the relation between the lattice vector and the scattering vector for an x-ray reflection to occur. There is a more visualized view to derive the Bragg equation as shown in Figure (2-7).

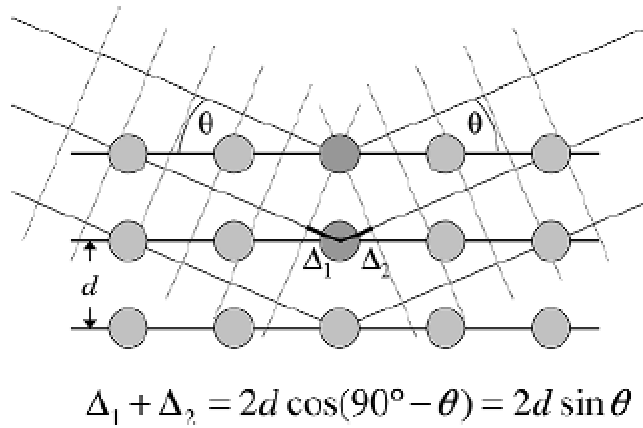

FIG. 2-7 Visualization of the Bragg equation

Constructive interference occurs when the phase difference equals integral multiples of wavelength λ and we can write

$$2d\sin\theta = n\lambda\ , \tag{2-20}$$

and this equation is valid for any lattice structure .

2.5 Intensity of Bragg Reflections

During the derivation of the Laue condition, the charge distribution is confined at the lattice point $\mathbf{r}_{\mathbf{n_1 n_2 n_3}}$. This result can be generalized by rewrite the sum in equation (2-15) to a continuous limit,

$$\int \rho_e(r) e^{-iQr} dr\ , \tag{2-21}$$

where $\rho_e(\mathbf{r})$ is the electronic charge distribution of the scattering object.

2.5.1 Atomic Form Factors

Formula 2-21 can be applied to atoms by inserting the square the electronic wave function for the charge density $\rho_e(\mathbf{r})$. We can thus define an atomic form factor *f* by

$$f = \int_{at} \rho_e(r) e^{-iQr} dr \quad \text{(2-22)}$$

In the limit of **Q**=0 the integration just runs over the charge distribution and yields the number of electrons of the atom Z.

For **Q**≠0, the atomic form factor is a function of **Q** or $\sin\theta/\lambda$ and the integration of *f* is too complicate and we won't include the calculation process here.

Figure 2-8 displays the result of the calculation. For low scattering angles f can reach values close to atomic number Z, but a steep decrease with increasing $\sin\theta/\lambda$ is clearly seen.

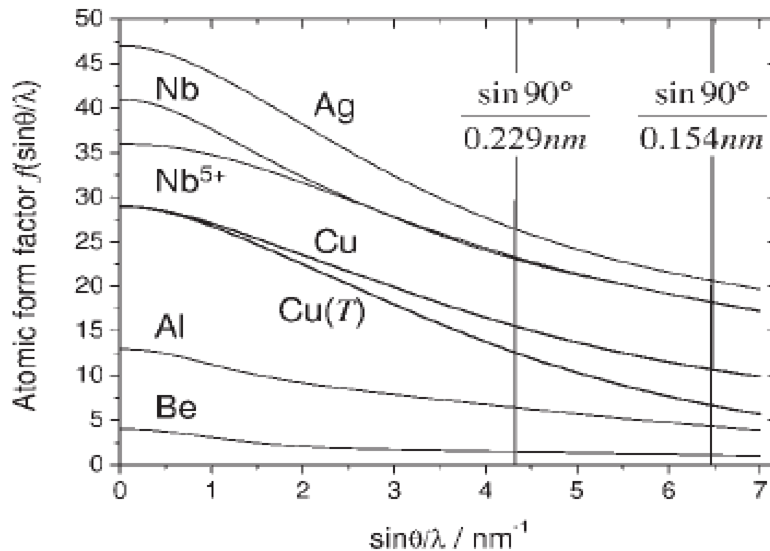

FIG. 2-8 Atomic form factors of some metallic atoms

2.5.2 Structure Factor

Formula 2-21 can also extend to a unit cell, and the quantity is then denoted as the structure factor ***F*** that is given by

$$F = \int_{uc} \rho_e(r) e^{-iQr} dr \quad , \tag{2-23}$$

We can rewrite this integration as a sum of N individual atoms in the unit cell

$$F = \sum_{n=1}^{N} \int_{at} \rho_e(r) e^{-iQ(r-r_n)} dr \ . \tag{2-24}$$

The integration over the charge distribution of individual atoms are given by atomic form factors f_n of the *n*th atom. Accordingly, the structure factor can be written as

$$F = \sum_{n=1}^{N} f_n e^{iQr_n} \ . \tag{2-25}$$

As mentioned above, the scattering intensity reaches its maximum only when the Laue condition is satisfied. Combining the equation 2-17 we can get

$$Q(x_n ac_1 + y_n ac_2 + z_n ac_3) = 2\pi(hx_n + ky_n + lz_n) \quad , \tag{2-26}$$

and the structure factor F can then be written as

$$F(hkl) = \sum_{n=1}^{N} f_n e^{2\pi i(hx_n + ky_n + lz_n)} \ . \tag{2-27}$$

The structure factor thus depends on the Miller indices of the reflection, the position of the atoms in the unit cell and the atomic scattering factor. In monoatomic lattices the atomic form factor is the same for all atoms and can be placed in front of the sum. For simple cubic structure N=1 and x=y=z=0 and thus ***F***=*f* for all hkl reflections.

For face-centered cubic (fcc), $(x_n\ y_n\ z_n)$ = (0 0 0), (0 1/2 1/2), (1/2 0 1/2), (1/2 1/2 0) and equation 2-27 yields

$$F_{fcc}(hkl) = f\left[1 + e^{i\pi(h+k)} + e^{i\pi(h+l)} + e^{i\pi(k+l)}\right] = \begin{cases} 4f---hkl, all`even/odd \\ 0----hkl, mixed \end{cases} . \quad (2\text{-}28)$$

It means that Bragg reflections are only observed for fcc lattice if all Miller indices are either even or odd.

The structure factor of the bcc lattice can be obtained in the same way and results in

$$F_{bcc}(hkl) = f\left[1 + e^{i\pi(h+k+l)}\right] = \begin{cases} 2f---h+k+l=2n \\ 0------otherwise \end{cases} . \quad (2\text{-}29)$$

For diamond structure like Si, there are 4 more atoms in the fcc-cubic with (x_n y_n z_n) = (0 0 0), (0 1/2 1/2), (1/2 0 1/2), (1/2 1/2 0), (1/4 1/4 1/4), (1/4 3/4 3/4), (3/4 3/4 1/4), (3/4 1/4 3/4) we take them into equation 2-27 and we end up with

$$F_{Si} = \begin{cases} 8f -----all`even`and`h+k+l=4n \\ 0------all`even`and`h+k+l=4n+2 \\ (4+4i)f --all`odd \\ 0------mixed \end{cases} . \quad (2\text{-}30)$$

There are accordingly less reflections to observe in the diffraction pattern of diamond-structured materials like Si than that of fcc-structured ones.

The material that we are going to characterize in the following chapter is GaN, and it can have different crystal structures as wurtzite or zinc-blende. GaN applied in semiconductors are usually wurtzite and it is a member of the hexagonal crystal system as shown in Figure 2-9.

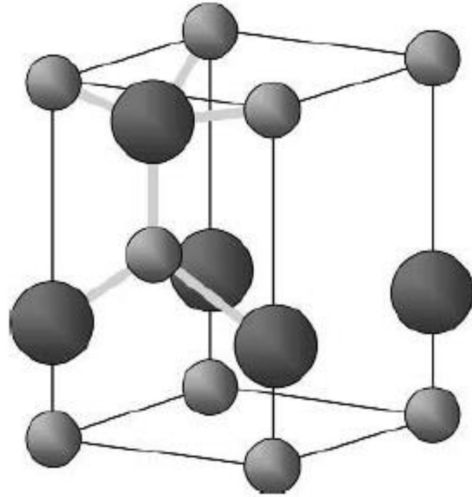

FIG. 2-9 Hexagonal wurtzite unit cell structure

There are two Ga atoms in the unit cell with position (0 0 0) and (1/3 2/3 1/2) while the two N atoms lies at (0 0 u) and (1/3 2/3 1/2+u), *u* is 3/8.

The structure factor for wurtzite structure ends up with

$$F^2_{\text{wurtzite}}(hkl) = \left(f_A^2 + f_B^2 + 2f_A f_B \cos(2\pi ul)\right)\begin{cases} 1 & h+2k=3n\pm1 \quad l \text{ even} \\ 3 & h+2k=3n\pm1 \quad l \text{ odd} \\ 4 & h+2k=3n \quad l \text{ even} \\ 0 & h+2k=3n \quad l \text{ odd} \end{cases} \quad . \tag{2-31}$$

Structure factor is of great significance because even though the Laue condition is satisfied for diffraction, the distribution of atoms in unit cell can cause destructive interference during scattering and no intensity will be detected. For illustration, no diffraction will be detected for wurtzite GaN (111) planes. The intensity for (111) plane can be calculated by equation 2-31 and it end up with 0.

2.5.3 Absorption Factor

Just like light and sound, when x-rays passing through matter, they suffer from an attenuation of intensity caused by their absorption. Intensity I_0 that enters into the sample will be exponentially damped to an amount $I_0 \exp(-2\mu l)$ after a path of $2l$. The parameter μ is called the linear attenuation coefficient and depends on the wavelength of the radiation used, the chemical composition of the sample and its density. The inverse of μ would give a penetration depth for normal incidence $\tau_{1/e} = 1/\mu$ that specifies the path length for which the intensity I_0 drops to $1/e$ of its initial value. The dimensions of the attenuation coefficient are m^{-1} or μm^{-1}. Often, the value of the mass absorption coefficient μ_m is listed in various tables that can be converted into $\mu = \rho\ \mu_m$ by multiplication with the mass density ρ.

The absorption coefficient for GaN is illustrated below in Figure 2-10[11].

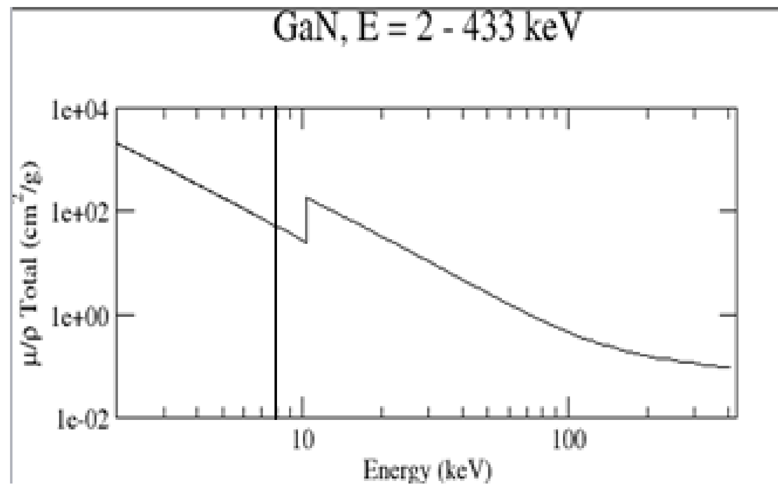

FIG. 2-10 Absorption coefficient of GaN of different energy

The energy of Cu Kα radiation can be easily calculated as hc/λ=8keV, and the absorption coefficient reads 51.94cm^2/g. Since the density of GaN ρ=6.15g/cm^3, the linear attenuation coefficient yields μ=314 cm^{-1}, and penetration depth $\tau_{1/e}$ =31.3 μm.

Figure 2-11 illustrate the absorption effect for a thin-film sample in a symmetric scan. For any x-ray beam that has traveled through a sample to become scattered into the detector the primary intensity has been reduced by the factor exp(–2μ*l*). The reduction of intensity of the total x-ray beam is the sum over all possible paths of the beam within the limits of 0 to l_{max}, it is noticed that path l can be expressed by depth variable z as $l = z/\sin\theta$ and the maximum of z is the thickness of the film t.

$$\int_0^{l_{max}} e^{-2\mu l} dl = \int_0^t \frac{1}{\sin\theta} e^{-2\mu z/\sin\theta} dz = \frac{1}{2\mu}\left(1 - e^{\frac{-2\mu t}{\sin\theta}}\right) \quad . \tag{2-32}$$

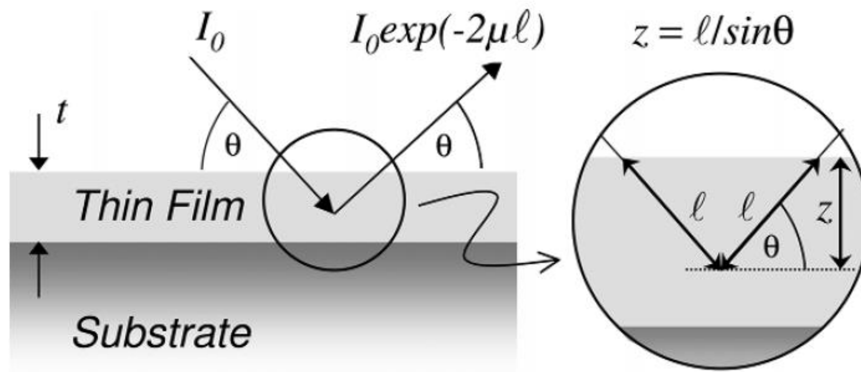

FIG. 2-11 Schematic representation of the absorption effect for a thin film sample

For infinitely thick sample, $t \to \infty$ and result yields 1/(2μ). In the following the absorption factor is denoted by the ratio of the absorption for a sample of finite thickness with respect to an infinitely thick sample

$$A = \frac{\int_0^t}{\int_0^\infty} = 1 - e^{\frac{-2\mu t}{\sin\theta}} \quad , \tag{2-33}$$

and since we already calculated the linear attenuation coefficient of GaN in this section. If we plot equation 2-33 with different thickness *t* in software Origin and we can get Figure 2-12.

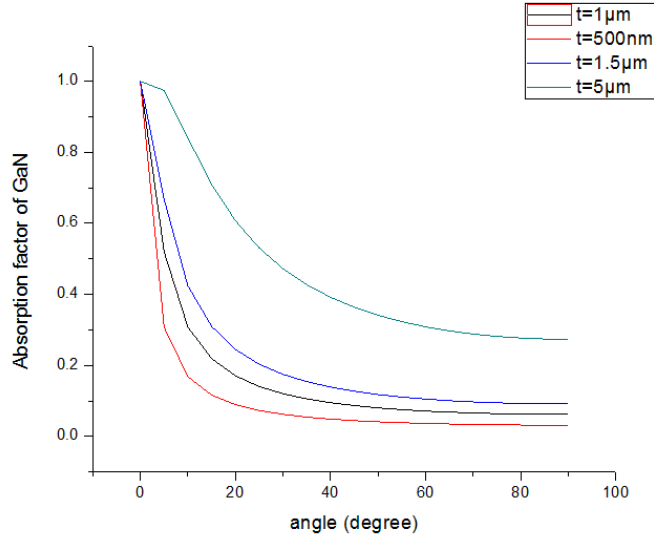

FIG. 2-12 Absorption factor *A* of GaN of different thickness plotted by Origin

It is seen from the plot that *A* approaches unity when the film is thicker. Accordingly, the absorption factor depends on the product of both angle and thickness.

2.5.4 Multiplicity

The multiplicity factor arises from the fact that in general there will be several sets of *hkl*-planes having different orientations in a crystal but with the same *d* and F (structure factor) values. For instance, in cubic system there are 8 equivalent (111) planes while 6 equivalent (200), so it is evident that the multiplicity m_h will enter the expression of a Bragg reflection intensity as a scaling factor.

2.5.5 Geometry Factor

The spreading of the Bragg peak over a circular segment of the {l_i} sphere as discussed above introduces a further θ dependency into the diffraction pattern of a θ/2θ scan. The effect is visualized in Figure 2-13 where the set of all diffracted intensity for scattering angle 2θ is symbolized by a cone of opening angle 4θ. The circumferences of the intensity rings scale with sin2θ causing a dilution of intensity by 1/sin2θ. There also arise a variety of scattering vectors Q that lie on a cone. The scattered intensity will scale with their density, which is $\sin(\pi/2-\theta) = \cos\theta$. The geometry factor is the product of both density functions and it is finally obtained as $G = \cos\theta/\sin 2\theta = 1/(2\sin\theta)$. [12]

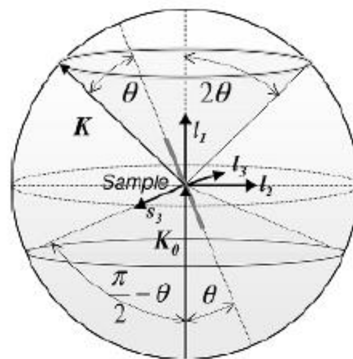

FIG. 2-13 Scattering in {l_i} frame to derive the geometry factor G

2.5.6 Preferred Orientation

It is a characteristic structural feature of thin polycrystalline films that certain crystallographic lattice planes can occur with a greater probability than others. This phenomenon is termed preferred orientation or texture and denoted as texture factor T_h. For a random orientation T_h=1. [13]

2.5.7 Diffracted Beam Intensity

When we combine all the factors mentioned above together, the intensity of Bragg diffraction ends up with

$$I_h = SCF \cdot m_h \cdot T_h \cdot G\overline{C^2}L \cdot \left|F_h\right|^2 \cdot A(t) \quad , \tag{2-34}$$

where SCF is scaling factor that lumps together all instrument settings like scan velocity, slit width, electron classic radius, wavelength of the x-ray and etc. L is the Lorentz factor induced by the integration calculation process of I_h and won't be discussed here. We often denote Lp=$G\overline{C^2}L = \frac{1+\cos^2\theta}{\sin\theta\sin 2\theta}$ as the Lorentz-polarization factor.

Equation 2-34 shows the relation between the diffraction intensity and diffraction angle. If we define the material (for example Si), texture,and thickness of layer, we can actually calculate the relative diffraction intensity at certain diffraction angle.

For illustration, if we have a random oriented Si sample with 10μm thickness, the calculated diffraction intensities are shown in Table 2-1.

Table. 2-1 Normalized diffraction intensity for random orientation Si from calculation

A	B	C	D	E	F	G	H	I
Si	bragg angle	2theta	Mh	Lp	strcture	absorption(10μm)		I
111	14.22	28.443	8	16.58	32	0.7	2971.136	100
220	23.65	47.303	8	6.24	64	0.522	1667.72736	56.13096674
400	34.57	69.131	6	3.165	64	0.4	486.144	16.36222643

Intensity values of Si measured from experiment is displayed in Figure 2-14. [14] We can see that the relative intensity from calculation of (111), (220) and (400) planes pretty match the measurement result.

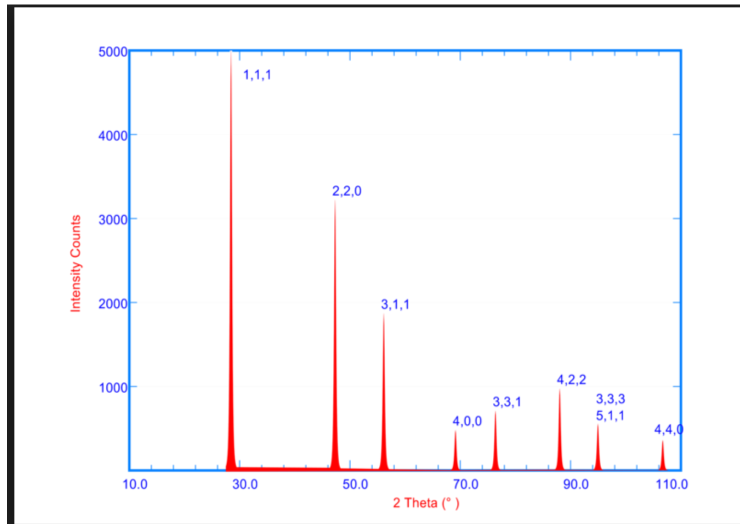

FIG. 2-14 XRD pattern of polycrystalline Si

2.6 Reciprocal Lattice

Every periodic structure has two lattices associated with it. The first is the real space lattice, and this describes the periodic structure. The second is the reciprocal lattice, and this determines how the periodic structure interacts with waves like x-ray. In the section, we will discuss how the Bragg diffraction happens in the reciprocal space.

2.6.1 Definition of Reciprocal Lattice Vector

The Laue condition 2-17 can be rewrite as $Q_L \cdot r_n =$ integral multiples of 2π describe the relation of scattering vector and lattice vector. If we denote Q_L as **K**, $\mathbf{r}_n$ as **R**, then this relation can rewritten as

$$e^{iKR} = 1 \quad . \tag{2-35}$$

Mathematically, we can describe the reciprocal lattice as the set of all vectors **K** that satisfy such reciprocal relation for all lattice point vector **R**. That is why reciprocal space is also called K space.

Just like any lattice vector in the real space can be expressed as $\mathbf{R}=\mathbf{r}_n=n_1a\mathbf{c_1}+n_2a\mathbf{c_2}+n_3a\mathbf{c_3}=n_1a_1+n_2a_2+n_3a_3$, the reciprocal lattice vector can also be expressed as $\mathbf{K}=hb_1+kb_2+lb_3$, While the $\mathbf{b_i}$ can be expressed by $\mathbf{a}_i$ as

$$b_1 = 2\pi \frac{a_2 \times a_3}{a_1 \cdot (a_2 \times a_3)}$$

$$b_2 = 2\pi \frac{a_3 \times a_1}{a_2 \cdot (a_3 \times a_1)}$$

$$b_3 = 2\pi \frac{a_1 \times a_2}{a_3 \cdot (a_1 \times a_2)} \quad . \qquad (2\text{-}36)$$

Based on these equations, we can easily derive that b_1 is perpendicular to the plane defined by a_1 and a_2 and the magnitude of b_1 will decrease with increasing a_1. In another word, the reciprocal space vector is perpendicular to its real space vector's normal plane and its magnitude is inversely proportional to the magnitude of its real space vector.

The transfer process from a 2D real lattice to reciprocal lattice is shown in Figure 2-15. We can see that b_1 is perpendicular to a_2 and b_2 is perpendicular to a_1.

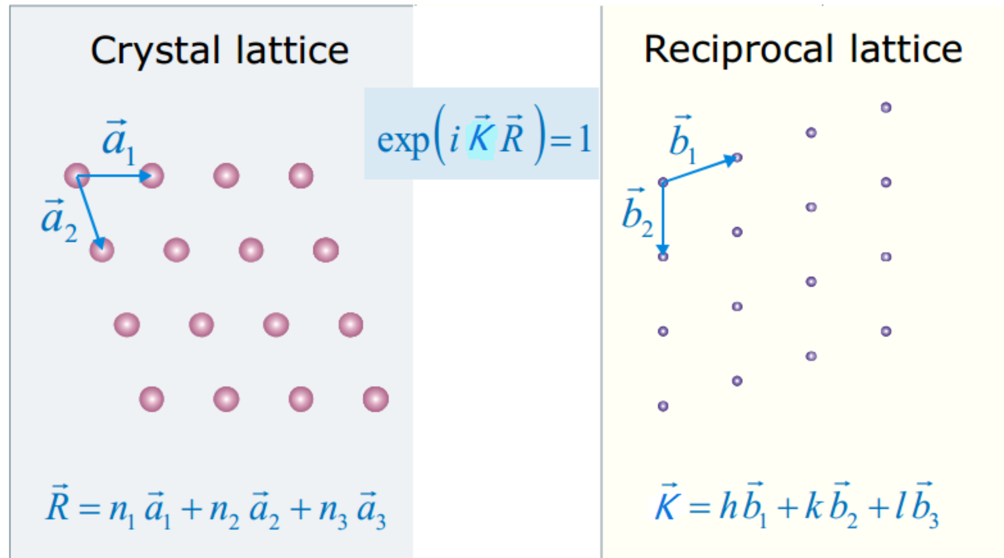

FIG. 2-15 Transfer from crystal lattice to reciprocal lattice

2.6.2 Diffraction In Reciprocal Space

Reciprocal lattice has following properties:

(1) A vector K_{hkl} draw form the origin of the reciprocal lattice to any point in it having coordinates *hkl* is perpendicular to the plane in the crystal lattice whose Miller indices are *hkl*

(2) The length of the vector K_{hkl} is equal to the reciprocal of the spacing d of (*hkl*) planes, or

$$|K_{hkl}|=|d^*_{hkl}|=\frac{2\pi}{d_{hkl}} \quad . \tag{2-37}$$

The important thing to note about these relations is that the reciprocal lattice array of points completely describes the crystal, as shown in Figure 2-16, each reciprocal lattice point is related to a set of planes in the crystal and represents the orientation and spacing of that set of planes.

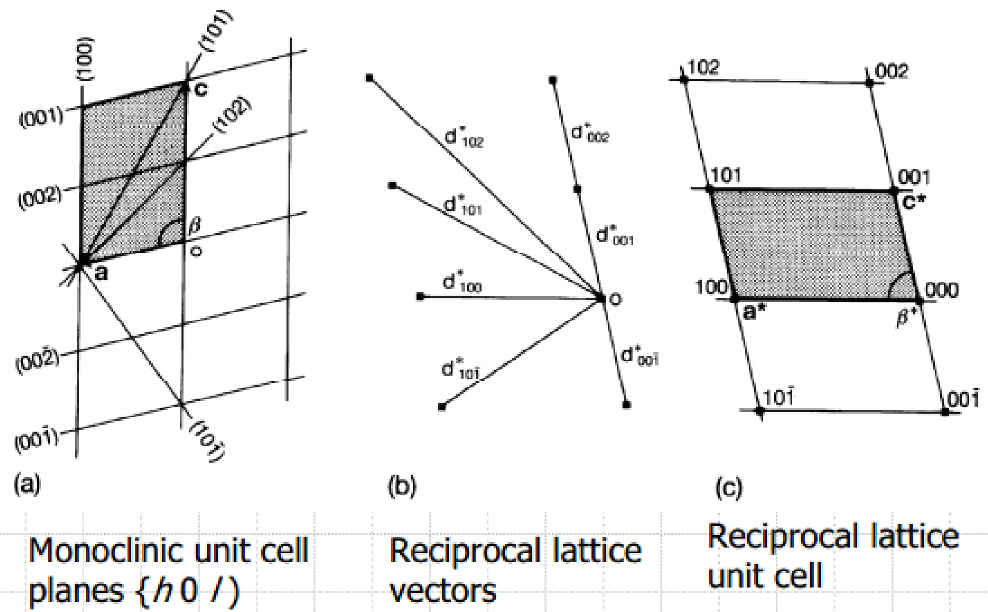

FIG. 2-16 ($h0l$) planes in real space and ($h0l$) point in reciprocal space

Since Laue condition can be written as equation 2-35, diffraction in reciprocal space can then easily expressed as $Q=K_{hkl}$, which is visualized in Figure 2-17

We can then derive the Bragg law in reciprocal space by

$$Q = K_{hkl} \Leftrightarrow \frac{4\pi}{\lambda}\sin\theta = \frac{2\pi}{d_{hkl}} \Leftrightarrow 2d_{hkl}\sin\theta = \lambda \quad . \qquad (2\text{-}38)$$

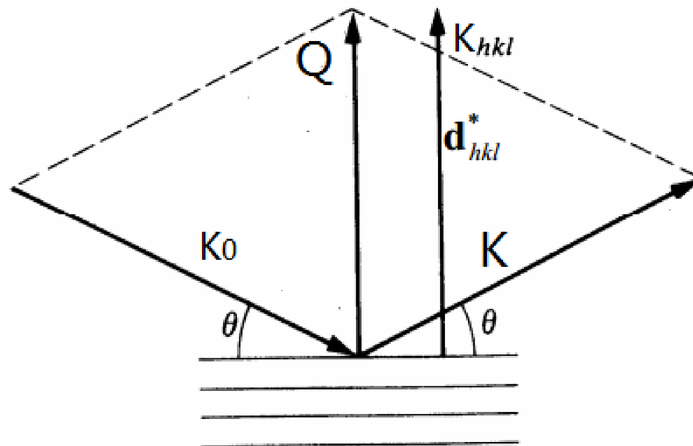

FIG. 2-17 Visualization of Laue condition in reciprocal space

2.7 Different Scan Techniques in X-Ray Diffraction Measurement

2.7.1 θ/2θ scan

θ/2θ scan is often used for measuring the Bragg reflection of a thin film. The working principle of a θ/2θ scan is visualized in Figure 2-18 in the hemisphere of the sample reference frame. The sample is positioned in the center of the instrument and the probing x-ray beam is directed to the sample surface at an angle θ. At the same angle the detector monitors the scattered radiation. The angle 2θ is defined as the angle between the extended incoming beam and the exit beam. The sample coordinate vectors s_1 and s_3 lie in the scattering plane defined by $\mathbf{K}_0$ and **K**. During the scan the angle of the incoming and exiting beam are continuously varied, but they remain equal throughout the whole scan and the scattering vector **Q** is always parallel to the substrate normal s_3. [15]

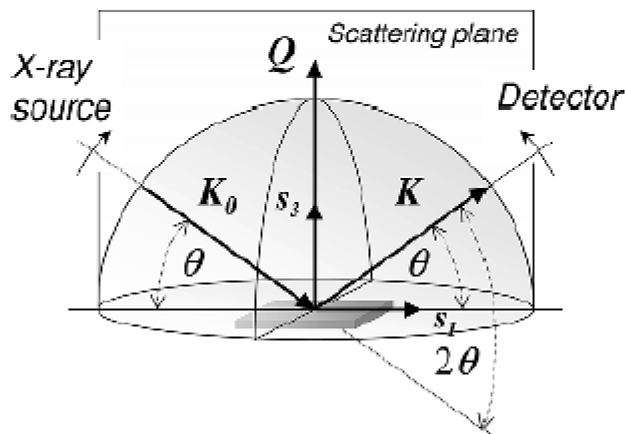

FIG. 2-18 Schematic representation of a θ/2θ scan

During the scan, only crystal planes that are parallel to the sample surface will show diffraction. Because the reciprocal vector of the other planes lie in a different direction from Q and thus can’t satisfy the Bragg law.

Figure 2-19 is a θ/2θ scan of GaN/AlGaN on sapphire form 30~45 degree. (002) planes of GaN, AlGaN and sapphire are parallel to the sample surface and diffraction peaks show up at 34.6, 34.9 and 41.5 degree respectively.

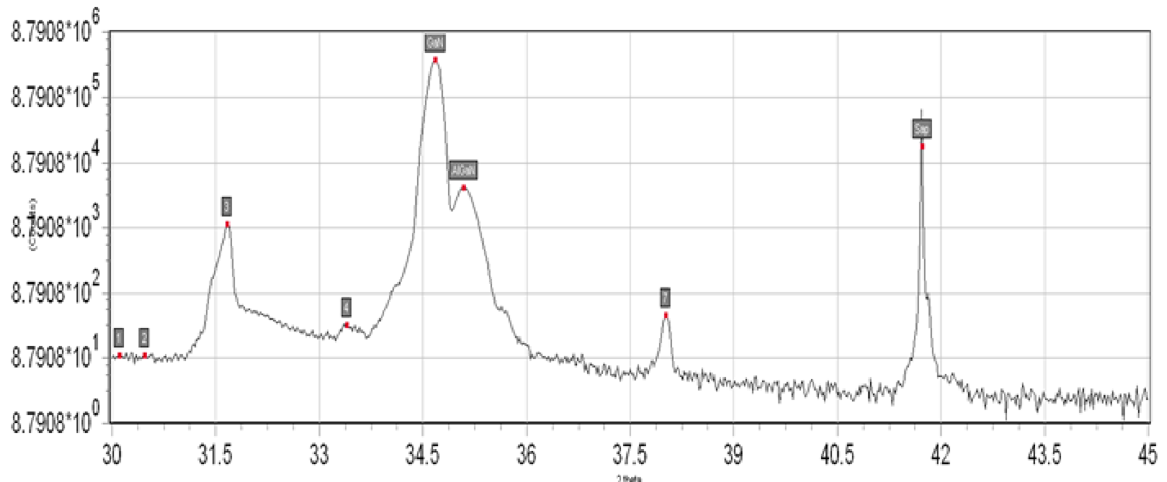

FIG. 2-19 θ/2θ scan pattern of GaN/AlGaN on sapphire

2.7.2 Omega scan/Rocking curve

A rocking curve (omega scan) produces observed intensity from planes that are not perfectly parallel. In a rocking curve scan, the detector is set at a specific Bragg angle and the sample is rock in a small angle as shown in Figure 2-20. For ω angles exceeding these limits the incoming/exiting beam would decline beneath the sample surface and no scattering information from the thin film would be collected. [16]

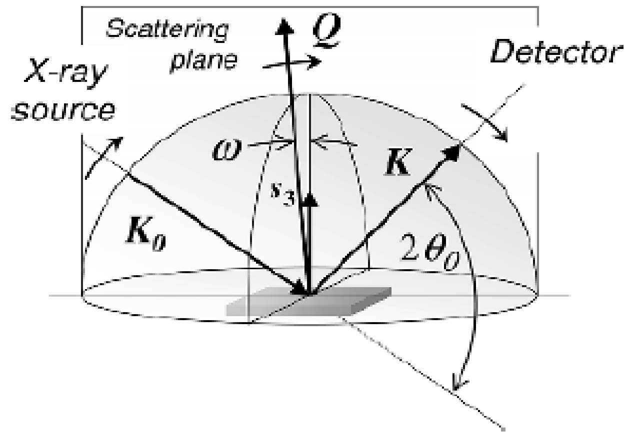

FIG. 2-20 Schematic representation of a rocking curve scan

A perfect crystal will produce a very sharp peak, observed only when the crystal is properly titled so that the crystallographic direction is parallel to the diffraction vectors. As red curve in Figure 2-21 shows, rocking curve from a perfect crystal will inevitably have some width due to instrumental broadening and the intrinsic width of the crystal material.

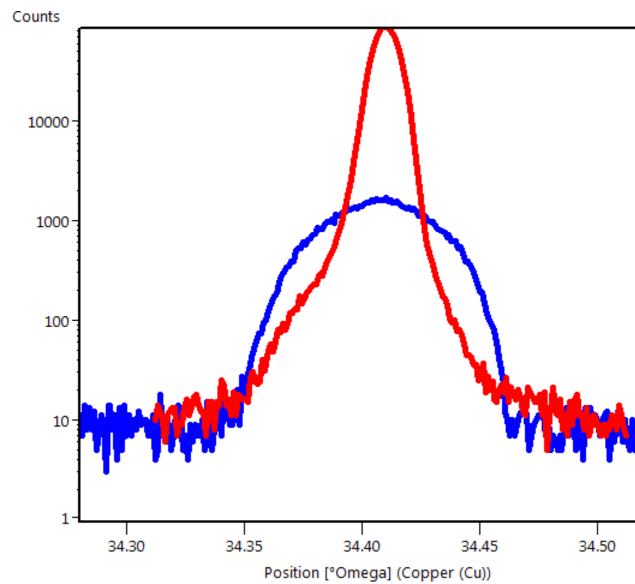

FIG. 2-21 Rocking curve of Copper with and without defects

Defects like mosaicity, dislocations and curvature shown in Figure 2-22 cause disruptions in the perfect parallelism of crystal planes. Some of the planes are tilted and the sample need to rock certain angles to fit the diffraction vector which cause the broadening of the rocking curve. [17]

We often use full width at half maximum (FWHM) to define the broadening of the peak. In high resolution rocking curve measurements, the FWHM of a perfect single crystal can be less than 100 arcsec. FWHM value of rocking curves can be a good reflection of crystalline quality, and dislocation density calculation by FWHM analysis will be discussed later.

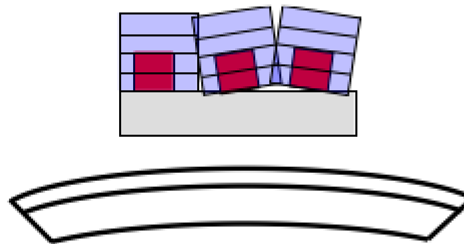

FIG. 2-22 Defects like Mosaicity and curvature

2.8 Reciprocal Space Mapping

2.8.1 Coordinates Set Up In the Reciprocal Space

It was already shown in case of a symmetric $\theta/2\theta$ scan that the scattering vector Q has only a nonzero component in the direction of the substrate normal that may be denoted by Q_z in the sample reference frame $\{s_i\}$. During a rocking curve scan, however, there also occurs a nonvanishing in-plane component Q_x for all angular positions ω except for the one point where $\omega = 0$.

Qx and Qz can be derived from Figure 2-20 as

$$Q_x = K[\cos(\theta-\omega) - \cos(\theta+\omega)]$$
$$Q_z = K[\sin(\theta-\omega) + \sin(\theta+\omega)] \quad . \qquad (2\text{-}39)$$

In section 2.2.3, we visualize the Laue condition in reciprocal space in a much simpler form and it is more convenient do analysis in Q_x Q_z coordinate than in instrumental coordinates ω and 2θ.

2.8.2 Different Scan in Reciprocal Space

Symmetric θ/2θ scan in (Q_x Q_z) plane is visualized in Figure 2-23(a), where the different configurations during the θ/2θ scan are symbolized by varying gray scales of the vectors involved. We can see that the scan will proceed along the Qz direction.

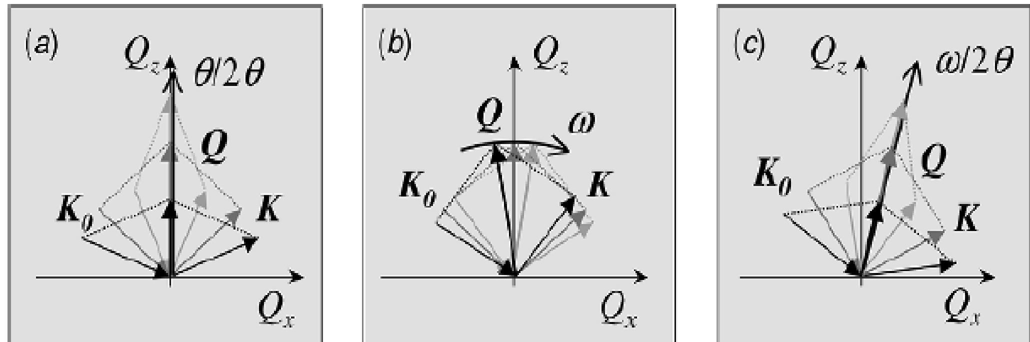

FIG. 2-23 Representation of (a) symmetric θ/2θ scan, (b) rocking curve scan and (c) asymmetric ω/2θ scan in (Q_x Q_z) plane

The rocking curve in (Q_x Q_z) plane will look different. According to Equation 2-39, the rocking curve scan will be a circular line because the magnitude of Q remain constant as shown in Figure 2-23(b).

θ/2θ in asymmetric plane is also called radial scan. The scan is a line along Q direction as shown in Figure 2-23(c).

2.8.3 Accessible Region in Reciprocal Space

The reciprocal lattice of a single atom cubic system is shown in Figure 2-24

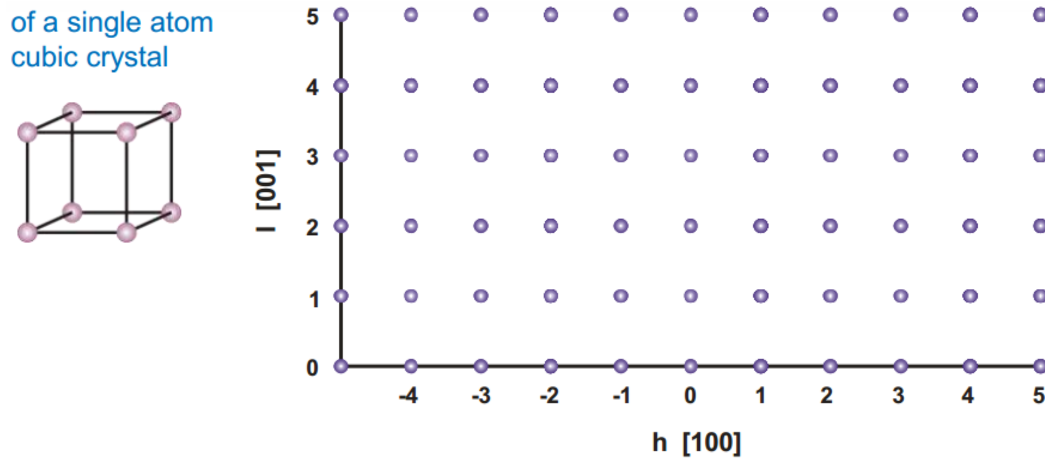

FIG 2-24 Reciprocal space of a single atom cubic crystal

We can take *h* as Q_x direction *l* as Q_z direction and based on Equation 2-39, and the accessible region for data collection can be represented by a hemisphere in Q space having $-2K \leq Q_x \leq 2K$ and $0 \leq Q_z \leq 2K$ and obeying $Q_x^2 + Q_z^2 \leq 4K^2$.

The area of reflection is divided from the areas of transmission by two other hemispheres of radius *K* that are centered at $Q_x = -K$ and *K* as shown in Figure 2-25, because incident angle and reflected angle should not be smaller than 0. The diffraction will not be detected in these areas.

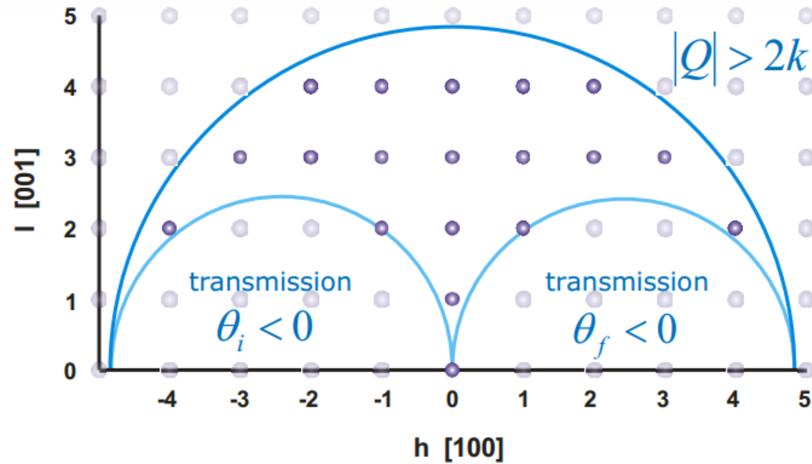

FIG. 2-25 Accessible region in reciprocal space

The accessible area includes an array of points representing the Miller indices of those Bragg reflections that can be observed.

2.8.4 Reciprocal Space Mapping Measurement

Reciprocal space mapping is performed such that the Bragg reflection under investigation is fully mapped in a confined area in Q space. This means that the reflection is not only monitored by one rocking curve crossing it, but the whole area in the vicinity of the reflection is included in the measurement. Reciprocal space maps may be obtained by joining together successive one-dimensional scans in Q space for which different procedures are possible. One way of mapping consists in performing various rocking curves with increasing scattering angle 2θ. This is shown schematically in the *Q* space representation in Figure 2-26.(a). Another technique makes use of successive radial scans (see Figure. 2-26(b)). In both cases an intensity map of the *Q* area around the Bragg

reflection is obtained. These maps deliver further structural information of epilayers to that obtained by rocking curve scans alone.

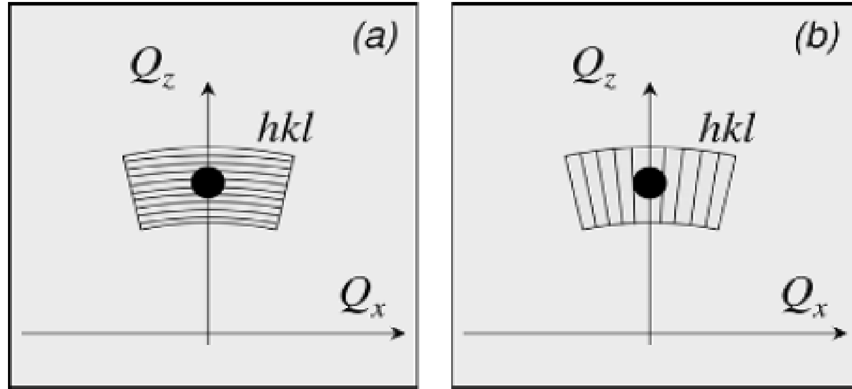

FIG. 2-26 Two different ways to measure RSM (a) subsequent rocking curve scan or (b) subsequent radial scans

2.8.5 Lattice Mismatch and Strain

One of the most important applications of RSM is analyzing the mismatch and relaxation in the epitaxial layers. Epitaxial growth is general in semiconductor device fabrication and happens when a single crystalline layer is deposited on another single crystalline substrate with the same crystal orientation and close lattice constant. The difference of lattice constant can cause lattice mismatch.

Define the lattice constant of layer as a_L and substrate a_S, then the lattice mismatch can be defined as $\Delta a = \frac{a_L - a_s}{a_s}$, for $\Delta a > 0$ the layer has larger lattice constant and during epitaxial growth, the layer will be compressed to the same lattice constant as the substrate and induce compressive strain to the film as shown in Figure 2-27.

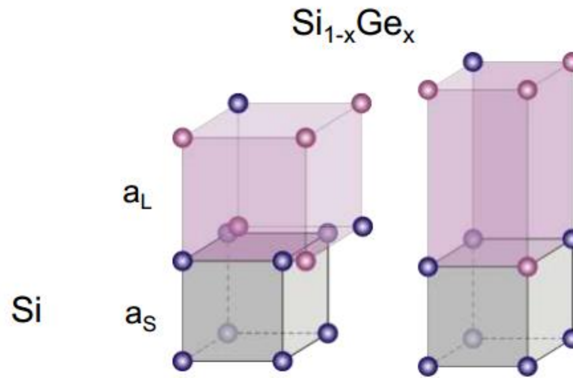

FIG. 2-27 Compressive strain induced when grow $Si_{1-x}Ge_x$ on Si

For $\Delta a < 0$, the layer has smaller lattice constant and will induce tensile strain in epitaxial growth as shown in Figure 2-28.

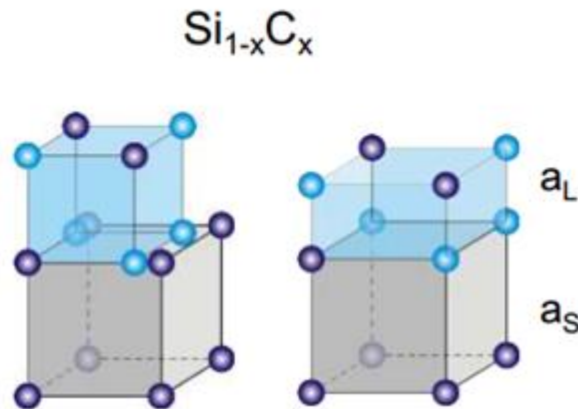

FIG. 2-28 Tensile strain induced when grow $Si_{1-x}C_x$ on Si

The strain component ε_{xx} and ε_{zz} are defined as

$$\varepsilon_{zz} = [c - c_0] / c_0 , \ \varepsilon_{xx} = [a - a_0] / a_0 \quad . \tag{2-40}$$

Based on theory of elasticity,

$$\varepsilon_{zz} = -D\varepsilon_{xx} \tag{2-41}$$

with $D = \frac{2c_{13}}{c_{33}}$, where c_{ij} are the elastic constants, for wurtzite GaN, c_{13}=106±20 Gpa and c_{33}=398±20 Gpa. We then end up with D_{GaN}=0.533.

2.8.6 RSM of Epitaxial Layers

Strain induced by lattice mismatch will accumulate during epitaxial growth. If the strain cannot be relaxed by the generation of dislocations, it will finally be released by the formation of cracks on the layer surface.

RSM is a powerful method to determine in-plane and out-plane lattice constant by convert the Qx,Qz value back to real space parameters, by the relations

$$a = \frac{\sqrt{(4/3)\cdot(h^2 + hk + k^2)}}{Q_x} \qquad c = \frac{l}{Q_z} \quad . \qquad (2\text{-}42)$$

Epitaxial layers in reciprocal space are shown in Figure 2-29 below. For a fully strained layer of $Si_{1-x}Ge_x$ on Si, the in plane lattice constant of the layer is compress to be same as the substrate and out plane lattice constant increase simultaneously. So in the reciprocal space, the reciprocal lattice point of $Si_{1-x}Ge_x$ will move right and down from its relaxed position for asymmetric planes.

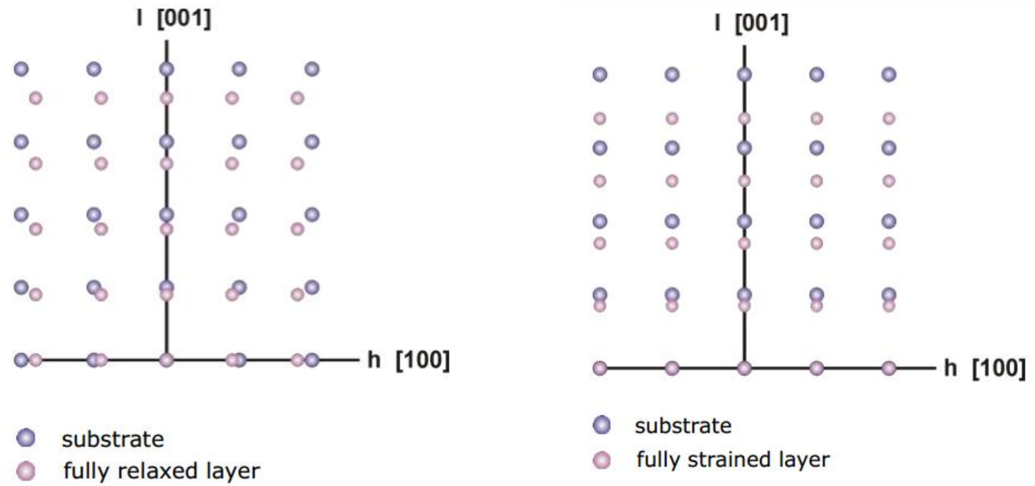

FIG. 2-29 Epitaxial layers in reciprocal space with fully relaxed (left) and fully strain (right)

The degree of relaxation is defined as

$$R = {[a(L) - a_0(S)]} \Big/ {[a_0(L) - a_0(S)]} \quad , \tag{2-43}$$

where a(L) and a_0(L) are measured and relaxed in plane lattice constant of layer, a_0(S) is relaxed in plane lattice constant of substrate.

The reflection of a fully strained layer in located on a perpendicular line, and the degree of relaxation R=0.

The reflection of a fully relaxed layer in on a line through the substrate reflection and (000), and the degree of relaxation R=1.

Reflections of partly relaxed layers are on the relaxation line (see Figure 2-30), and the relaxation line can be drawn by the equation $\tan\alpha = \tan\tau / D$, where D=0.533 for GaN.

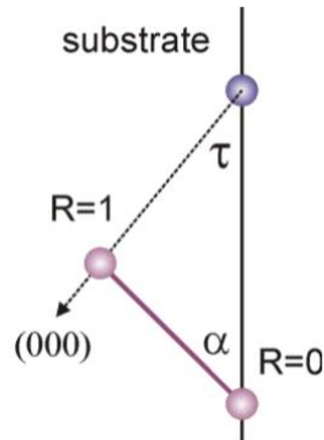

FIG. 2-30 Relaxation line

2.9 Dislocations in Epitaxial GaN Layers

During epitaxial growth of GaN, the strain caused by lattice mismatch will accumulate and then relaxed by forming dislocations. Carriers like electrons will confined at dislocations and affect the performance of device. So the characterization of dislocation density in GaN layer is of vital importance.

The most direct way to determine the dislocation density is transmission electron microscopy (TEM), but this process is destructive and time taking. A more convenient way to analyze dislocation density is using high resolution x-ray rocking curves.

Highly imperfect layers are often described as mosaic crystals which can be characterized by mean tilt and twist angles and the average size of the mosaic blocks. The tilt describes the rotation of the mosaic blocks out of the growth plane, and the twist their in-plane rotation. [17] As shown in Figure 2-31, the screw threading dislocations (TD) with Burgers vector b_s=[0001] will cause tilt of (002) plane, while the density of edge TD with

$b_e = \frac{1}{3}[11\bar{2}0]$ will distort (002) plane and twist planes perpendicular to (002) plane, like (100) plane.

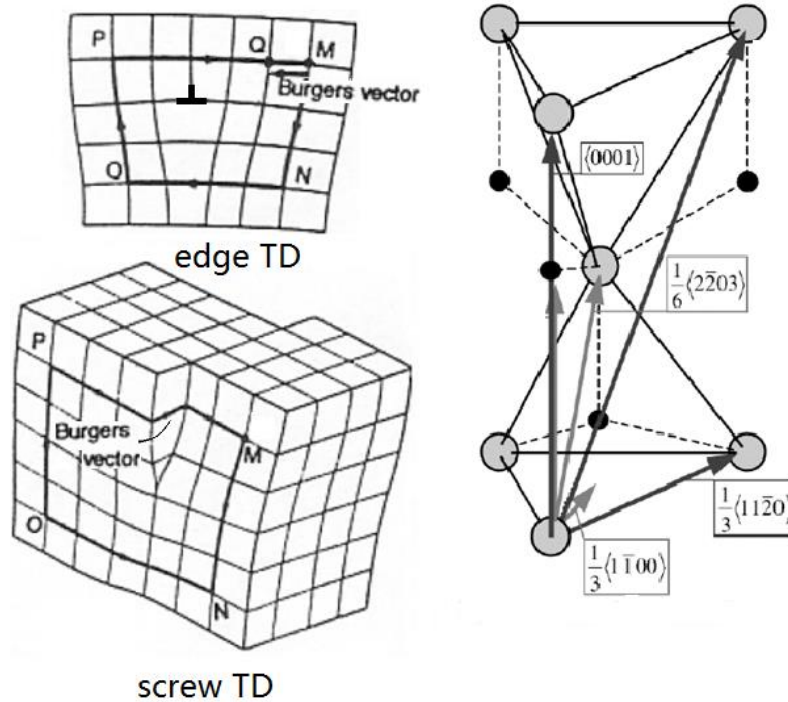

FIG. 2-31 Tilt and twist caused by different Burger's in GaN

For GaN epilayers, the mean tilt angle was shown to almost linearly depend on the rocking curve FWHM of (002) plan. While the twist depends on the rocking curve FWHM of (100) plane. [18] However, the (100) plane is in the same direction of growth and diffraction of (100) plane can't be observed. A skew symmetric diffraction geometry is applied [19]. As shown in Figure 2-32. By measuring different reflections with increasing lattice plane inclination, one can extrapolate to lattice planes with Ψ=90º

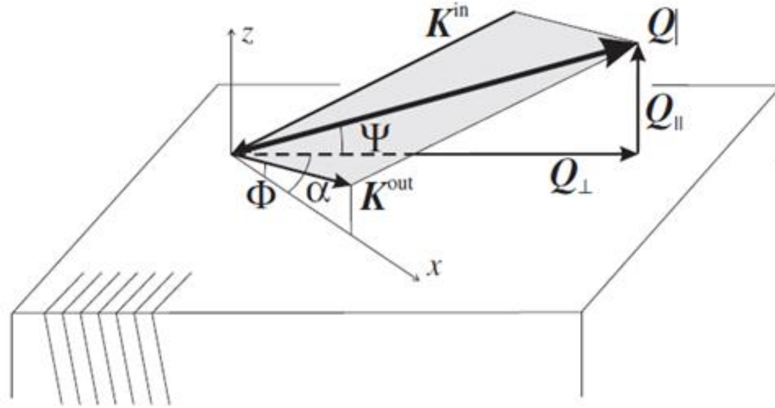

FIG 2-32 Sketch of skew geometry x-ray diffraction, Ψ is the inclination angle

After we extrapolate and get the FWHM of (100) plane $\beta_{(100)}$, we can denote twist as $\Delta\omega_e=\beta_{(100)}$. Tilt is equal to the FWHM of (002) plane, written as $\Delta\omega_s=\beta_{(002)}$

Then the edge and screw dislocation density can be calculated by

$$\rho_{edge} = \frac{\Delta\omega_e^2}{4.35 b_e^2} \qquad \rho_{screw} = \frac{\Delta\omega_s^2}{4.35 b_s^2} \quad . \tag{2-44}$$

2.10 X-Ray Reflectivity

2.10.1 Refractive Index for X-Rays

The refractive index n can be denoted as

$$n=1-\delta , \tag{2-45}$$

where $\delta = \rho_e \frac{\lambda^2 r_e}{2\pi}$, r_e is the classic radius of the electron and ρ_e is is electron density (number per nm^3), it is related to the density and the density of the material. [20]

2.10.2 Total External Reflection and Critical Angle

If refraction and reflection of x-rays under small incidence angles are considered in the formalism of geometrical optics, it turns out that below a critical angle the effect of total reflection will occur. The critical angle is denoted by α_c. The effect is similar to geometrical optics, where a light beam changes from an optically dense medium into a less dense one and which can be applied to confine a light beam in a glass fiber.

According to Snell's law of refraction, the sine of the incoming and outgoing angles is proportional to the refractive indices of the two media at the interface of which the transition occurs. The Snell's law can be written as

$$\frac{1}{n} = \frac{\cos \alpha_t}{\cos \alpha} \quad , \tag{2-46}$$

where α_t and α are the angles of transmitted and incident beam, respectively. For total external reflections, both angles may be assumed very small such that the cosine function can be approximated as $\cos x = (1 - x^2/2)$

$$\alpha_t = \sqrt{\alpha^2 - 2\delta} \quad . \tag{2-47}$$

Total reflection, i.e., $\alpha_t = 0$, will be observed for all angles of incidence for which the condition $\alpha 2 \leq 2\delta$ is fulfilled. The critical angle α_c is thus defined from this condition and it holds

$$\alpha_c = \sqrt{2\delta} \ . \tag{2-48}$$

2.10.3 Reflectivity of a Single Layer

Figure 2-33 displays a schematic beam trace figure, the phase difference Δ between the two beams is given by the relation

$$\Delta = (AB + BC)n - AD \quad . \tag{2-49}$$

While the phase shift is related via

$$\Delta = 2t \sin\theta_t \approx 2t\theta_t = 2t\sqrt{\theta^2 - \theta_c^2} \quad . \tag{2-50}$$

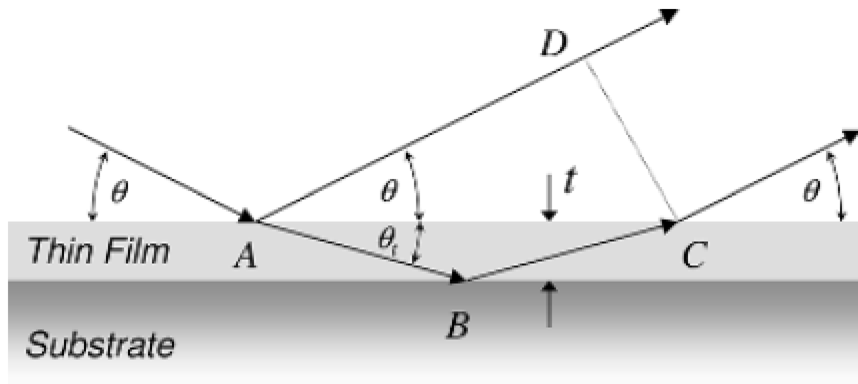

FIG. 2-33 Schematic representation of reflected and refracted beams for the derivation of their phase difference Δ

A maximum is observed whenever the phase difference is a multiple of the wavelength, $\Delta = m\lambda$. The evaluation proceeds by assigning an index m to each oscillation maximum and forming the square

$$\theta_m^2 = \theta_c^2 + \left(\frac{\lambda}{2t}\right)^2 m^2 \quad . \tag{2-51}$$

It is evident from equation 2-51 that the distance between two adjacent fringes can be written as

$$2\theta_{m+1} - 2\theta_m \approx \frac{\lambda}{t} \quad . \tag{2-52}$$

So by analyzing the fringes of XRR pattern will directly yield the film thickness *t*, while analyzing the critical angle will yield the density and composition of the material. The effect of roughness is shown in Figure 2-33, roughness will make the XRR patter steeper and increase the amplitude of high angle fringes.

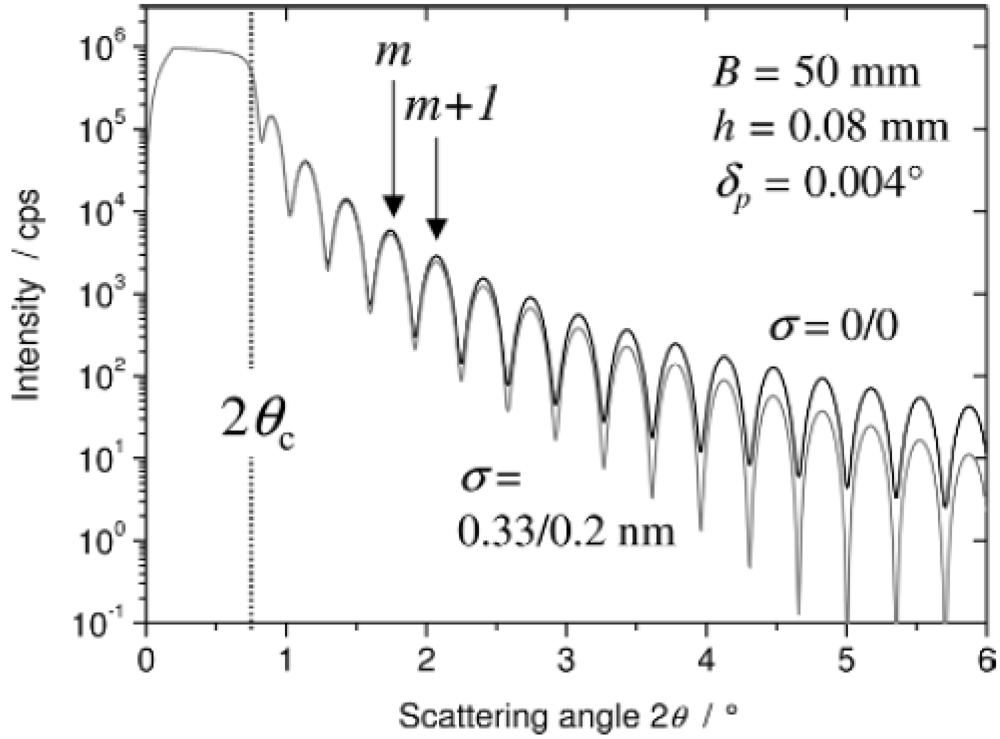

FIG. 2-34 Effect of roughness in XRR measurement

3. EXPERIMENT

3.1 Introduction of the X-Ray Diffractometer

Measurements are taken on the Bruker D8 Discover high-resolution x-ray diffractometer (HR-XRD). The diffractometer configuration in shown in Figure 3-1

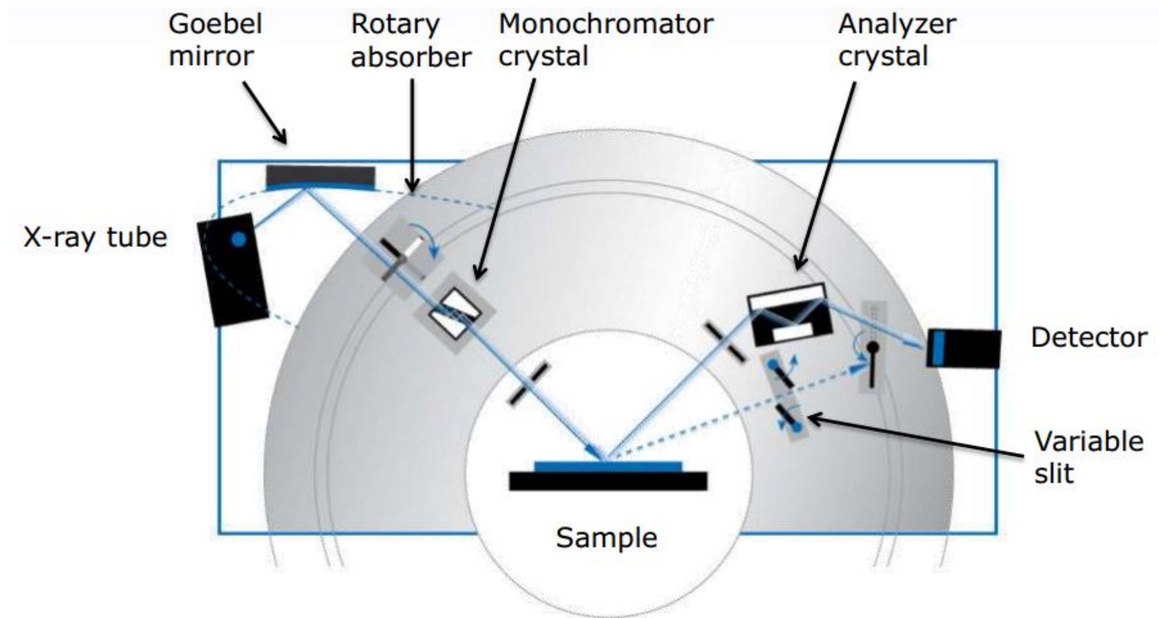

FIG. 3-1 Bruker D8 Diffractometer Configuration

The working voltage and current is set at 40kV and 40mA, and the warming up time is around 30 minutes. After the x-ray is generated in the x-ray tube, a laterally graded multilayer mirror also named Goebel mirror can reduce the divergence of the beam.

A rotary absorber is used to control the intensity of the x-ray beam, 4 absorbers are put 90 degree from each other and during alignment of instrument, the absorber is always set at the maximum value.

Before the x-ray finally reaches the sample surface, a monochromator is used for high resolution purpose. It is made from (220) single crystalline Ge, and it can eliminate the $K_{\alpha 2}$ spectrum from the x-ray and reduce the divergence of the X-ray beam to only a few arc-seconds. The length (*L*) of the X-ray beam on the sample is: L=h/$sin(\omega)$, where h is the height of X-ray beam determined by the slit and ω is the incident angle.

The receiving side optics are also applied to limit the width and divergence before it enter the detector. Analyzer crystals are often applied to limit the divergence and height of diffracted x-ray beam.

The sample is loaded to the sample holder, and a close view of experiment equipment with sample loaded in shown in Figure 3-2. The source of the x-rays comes from the right part and enters the detector on the left side.

The sample can move in seven freedoms as shown in Figure 3-2. 1~3 are three orthogonal coordinates that can adjust the position of the sample. Before measurement, the sample is always needed to be aligned in order that the x-ray beam shoot at the center of the sample.

5 and 6 are rotating coordinates of ω and 2θ respectively. These two coordinates are extremely precise and the increment of each scan step can be as low as 0.0001 °. The x-ray source is put at a fixed position. The changing of ω is obtained by rotating sample surface in coordinate 5.

4 is a rotating coordinates of inclination Ψ angle also known as Chi angle. During Chi scan, sample surface is rotating around its center and lattice planes that are inclined to sample surface can be brought to the scattering direction. Chi angle is of vital importance to find diffraction of asymmetric planes.

The sample can also rotate in the plane of its surface, shown as 7. This type scan is also known as in-plane Φ scan. Φ scan are often applied to determine the in-plane orientation and symmetry of the lattice

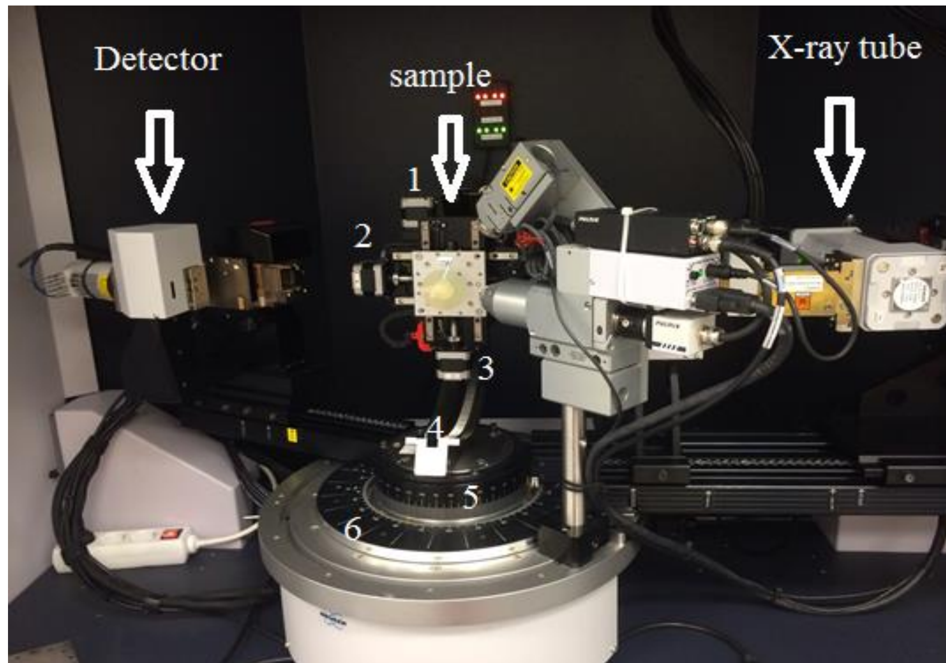

FIG. 3-2 Bruker high resolution x-ray diffractometer with sample loaded

3.2 Sample Description

The GaN samples for characterization can be divided into two groups.

The first group of GaN samples is deposited on sapphire. As shown in Figure 3-3, all of them are circular shape with 2 inch size and the transparent substrate is sapphire with c plane orientation.

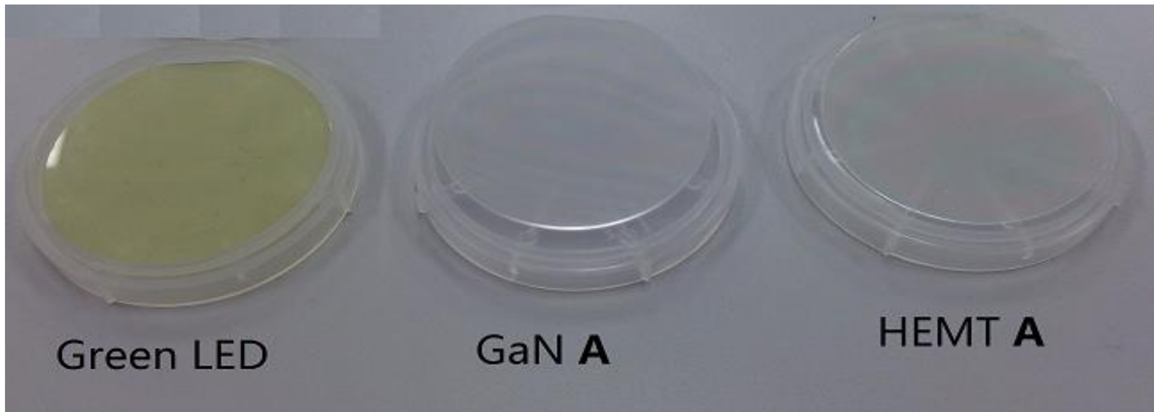

FIG. 3-3 GaN on sapphire samples

The green sample on the left is a 2 inch Green LED, it is a junction of p-GaN and n-GaN with a superlattice structure of InGaN/GaN acting as multiple quantum wells (MQW) in between. The estimated structure is shown in Figure 3-4(a).

The glass like sample in the middle is a 2 inch GaN on sapphire (denoted as GaN A). The glass like sample with darker color on the right is a 2 inch HEMT on sapphire (denoted as HEMT A) The structure of HEMT A is shown in Figure 3-4(b). 2 dimension electron gas (2DEG) is formed at the interface of GaN and AlGaN due to band structure, and 1~3 nm GaN cap is on the top.

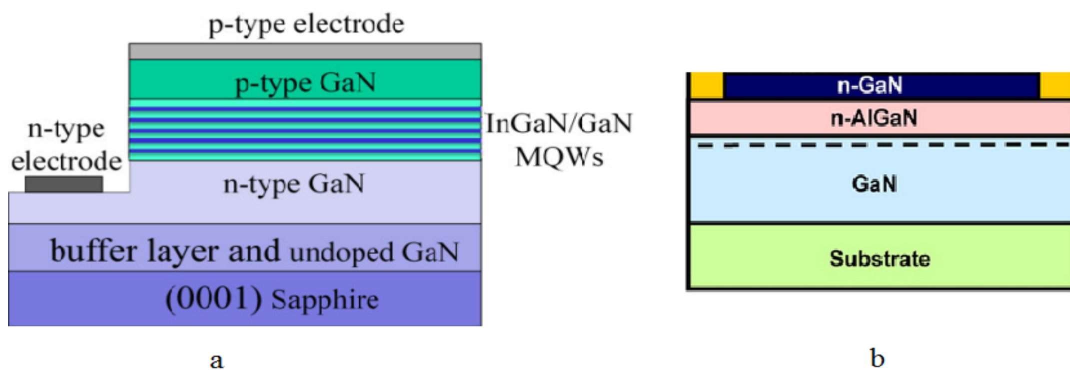

FIG 3-4 Sketch of (a) Green LED (b) HEMT on sapphire structure

The second group of GaN samples is HEMT deposited on Si. As shown in Figure 3-5, HEMT on Si all have mirror like surfaces. The small triangle shape on the left is one piece of 6 inch HEMT on Si (denoted as HEMT B). The circular shape in the middle is a 2 inch HEMT on Si (denoted as HEMT C). The large triangle shape on the right is a piece of 4 inch HEMT on Si (denoted as HEMT D).

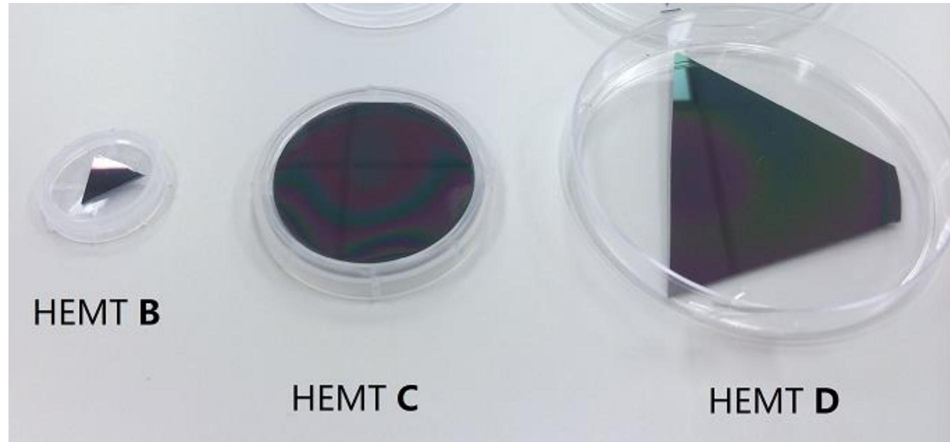

FIG. 3-5 GaN on Si samples

GaN cannot be deposited directly on Si due to wetting problems and lattice mismatch. A buffer layer made of AlN and AlGaN with different Al composition is applied. The structure of HEMT on Si share the structure shown in Figure 3-6, like HEMT A, all the HEMT on Si also have a GaN cap on the top.

FIG. 3-6 Sketch of GaN on Si with buffer layer

3.3 HR-XRD measurement

3.3.1 Symmetric θ/2θ Scan

For samples of GaN on Sapphire, θ/2θ scans are taken in the range of 30 °~ 45 °, to detect both the GaN peak around 34.6 °and sapphire peak around 42 °. For samples of GaN on Si (111), θ/2θ scans are taken in the range of 28 °~ 38 °to include the Si (111) peak around 29 °.

All the samples are aligned on the GaN peak first before we run the symmetric scan. During scan, increment is set at 0.005 °per scan type with scan speed is 0.1 sec/step.

3.3.2 Skew Geometry Rocking Curve Measurement

Planes with different inclination angles are selected for skew geometry rocking curves. Rocking curves for GaN (002), (105), (103), (102), (101) and (201) are measured at inclination angle *Chi* = 0 °, 20.32 °, 31.26 °, 42.76 °, 61.72 °, 74.7 ° respectively. (The diffraction parameters are obtained from the Software XRD Wizard). The increment of each step is 0.005 °with scan speed 1 sec/step. After measurements, FWHMs are plotted against Chi and extrapolated.

3.3.3 RSM measurement

RSM is measured for all HEMT samples and Green LED. The accessible region for GaN in reciprocal space is shown in Figure 3-7. Parameters are set to make the scan area (black area in Figure 3-7) cover enough Q space.

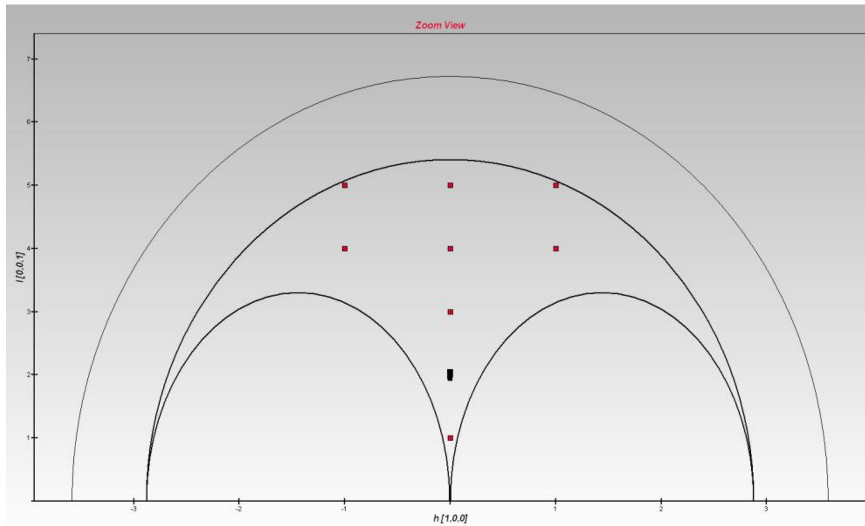

FIG 3-7 Accessible region for GaN in XRD Wizard

The dark line in Figure 3-8 represents ω/2θ scan in reciprocal space. Radial scan at different ω angle form a 2D map that cover the area around diffraction point.

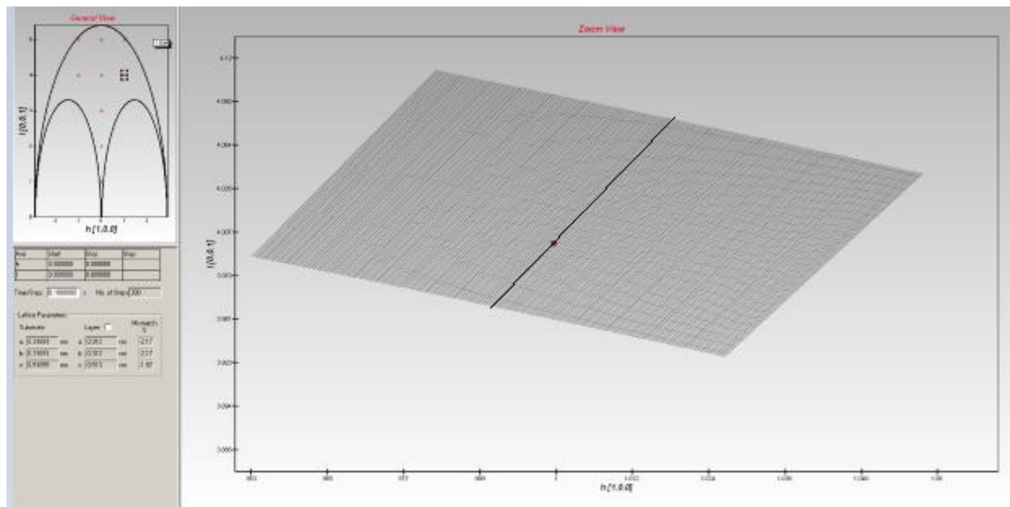

FIG.3-8 Scan area in XRD Wizard

Symmetric plane (002) and asymmetric plane (104) are selected for RSM.

3.4 XRR Measurements

XRR measurements are taken for all HEMT samples. During measurement the monochromator Ge 220 is removed, and only Geobel Mirror is chosen for the incident beam optics because high intensity of x-ray is needed. Since the incident angle ω is very small during measurement, smaller slit of 0.2 mm is inserted since the length of x-ray $L=h/sin(\omega)$

Additional slit of 1mm is also inserted in front of the detector. The range of XRR scan is from 0.1 to 6 °, increment 0.005 °per step and 0.4 sec/step.

3.5 Simulation by Software LEPTOS

1. HEMTs and Green LED composition simulation
2. XRR simulation for top AlGaN thickness and interface roughness

4. RESULTS AND DISCUSSION

4.1 Symmetric θ/2θ Scan

4.1.1 GaN on Sapphire

(1) θ/2θ Scan of GaN A is shown in Figure 4-1.

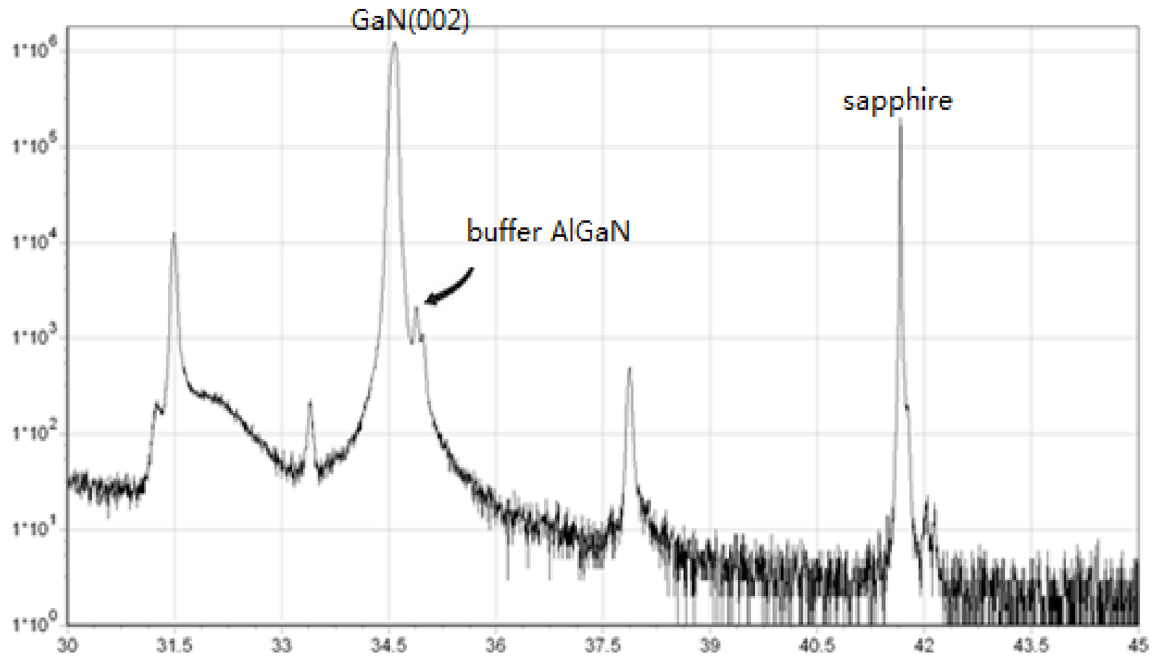

FIG. 4-1 θ/2θ Scan of GaN A

The sharp and intense peak at 41.4 °corresponds to single crystalline sapphire substrate with c plane orientation. The smooth and more intense peak at 34.6 °indicates that single crystalline wurtzite GaN with (002) orientation is epitaxial grown on the sapphire substrate. The peak around 38 °is the diffraction of the aluminum sample holder.

The single crystalline wurtzite GaN is also confirmed by in-plane Φ scan of (102) plane. As shown in Figure 4-2, diffraction occurs at 60 intervals indicate a 6-fold symmetry of the wurtzite structure.

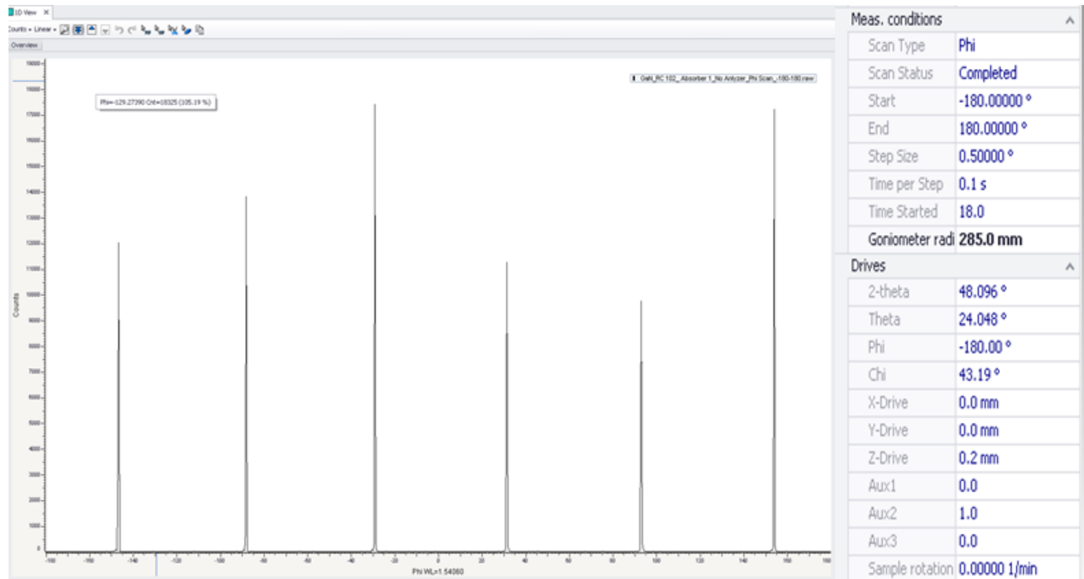

FIG. 4-2 Φ scan of (102) plane

(2) θ/2θ Scan of HEMT A is shown in Figure 4-3.

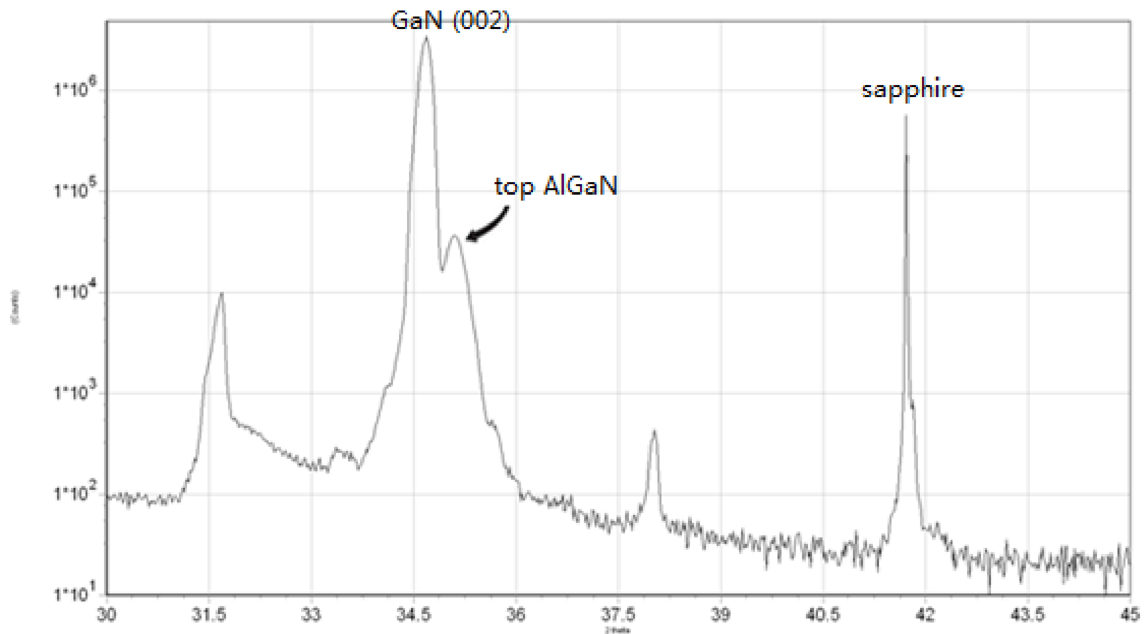

FIG. 4-3 θ/2θ Scan of HEMT A

In addition to the (002) GaN peak and c plane sapphire peak, the peak around 35 °is the (002) diffraction of the top $Al_xGa_{1-x}N$ layer in the HEMT structure. No buffer layer is observed.

Since the position of the $Al_xGa_{1-x}N$ depends on both Al composition *x* and relaxation degree during epitaxial growth. Asymmetric RSM measurement to determine the relaxation degree is necessary before we can simulate the Al composition.

(3) θ/2θ Scan of Green LED is shown in Figure 4-4.

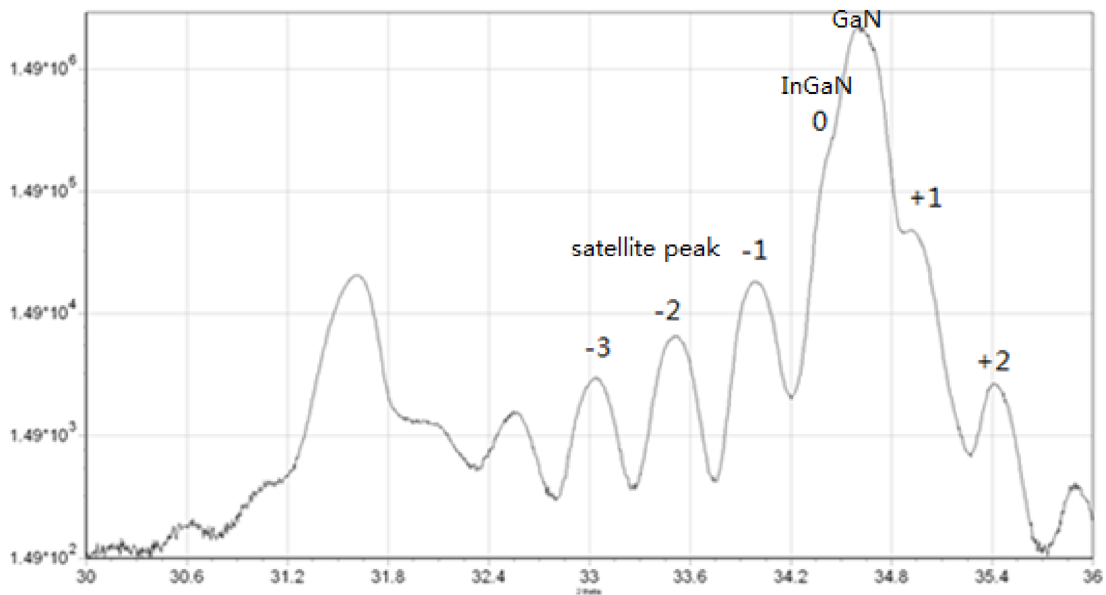

FIG. 4-4 θ/2θ Scan of Green LED

As we can see, the periodic peak distribution indicates a superlattice structure of $In_xGa_{1-x}N$/GaN. These perfect peaks are labeled from -3 to +2. The 0 order peak is not that obvious because $In_xGa_{1-x}N$ with a relative low In composition will have a close lattice constant to GaN according to Vegard's Law. Diffraction of these similar lattices is merged with each other as shown in the figure.

Since the angular position of the superlattice peaks are depend on both In composition and relaxation degree, we cannot apply Vegard's Law to calculate the In composition. Vegard's Law is based on the assumption that all the lattice are fully relaxed. In order to get the In composition, we need to obtain the degree of relaxation by RSM first.

4.1.2 GaN on Si

(1) θ/2θ Scan of HEMT B is shown in Figure 4-5.

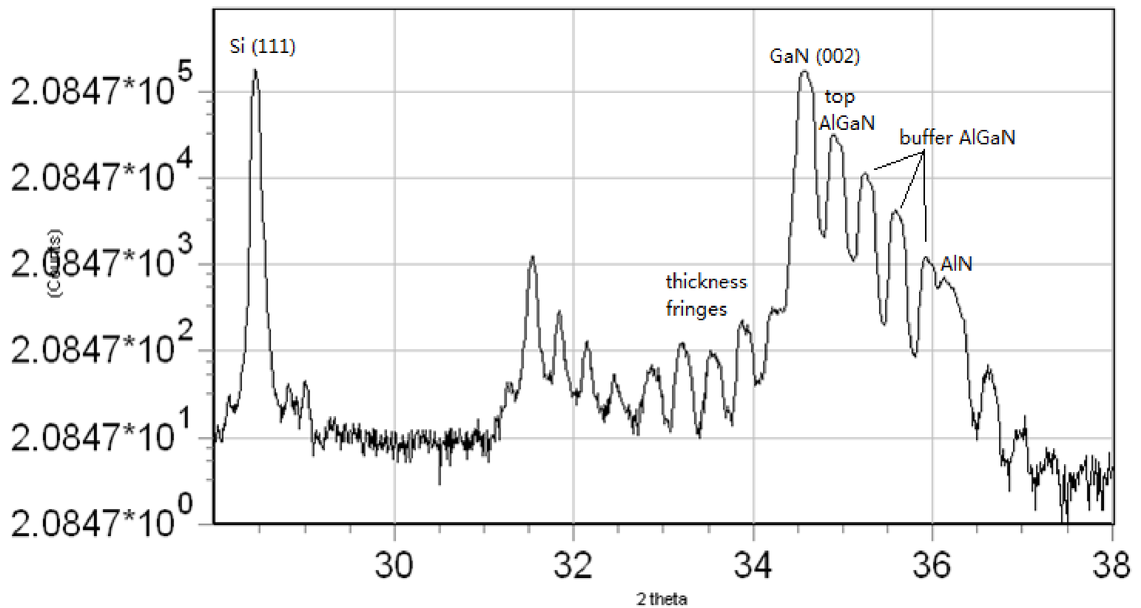

FIG. 4-5 θ/2θ Scan of HEMT B

As we can see from this figure, many small peaks with intensity of 10^3 show up due to induced buffer layer. The estimated buffer layer structure is $Al_xGa_{1-x}N$ with gradually decreased x value. The simulation of this structure will be included after the RSM measurement.

The peaks at positions less than 34 or higher than 36 correspond to thickness fringes of top AlGaN layer. We can simulate the thickness based on these information. The sharp and intense peak at 28.4 °represents the perfect single crystal Si wafer with (111) orientation.

Intense peak at 34.6 °indicates that single crystalline GaN with (002) orientation is deposited. The peak at around 36 °is the AlN (002) diffraction and the peak around 35 °is the top AlGaN layer.

(2) θ/2θ Scan of HEMT D is shown in Figure 4-6.

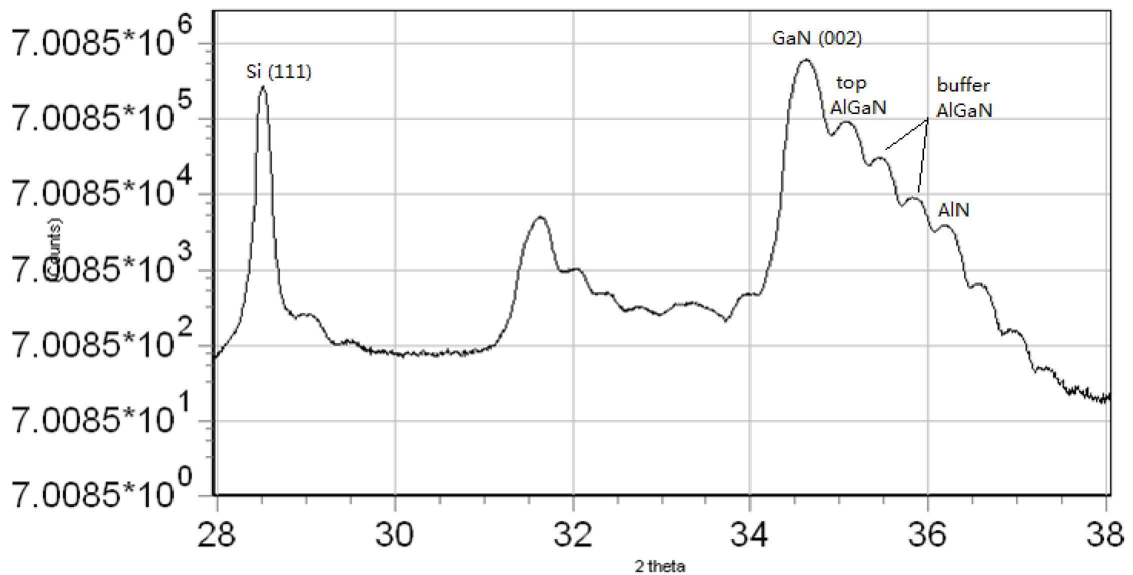

FIG. 4-6 θ/2θ Scan of HEMT D

As we can in this Figure, similar pattern is observed in HEMT B, indicating that they have similar buffer layer structure. The peaks after 36 °correspond to the thickness fringes of top AlGaN layer.

(3) θ/2θ Scan of HEMT C is shown in Figure 4-7.

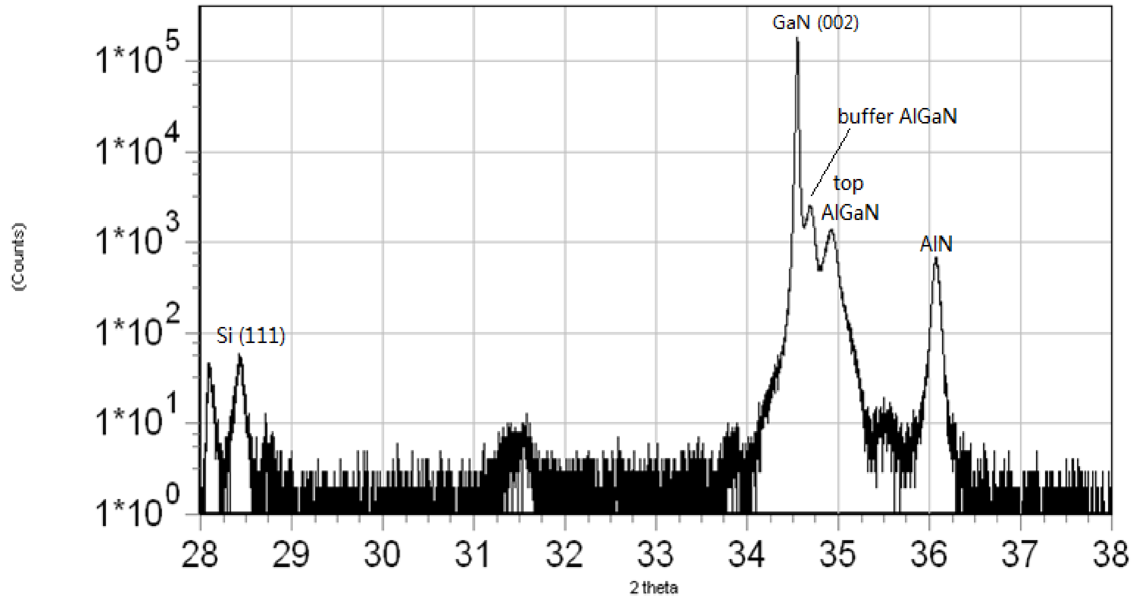

FIG. 4-7 θ/2θ Scan of HEMT C

The Si peak intensity is relatively low in this figure, since it is aligned on the GaN peak, it means the GaN (002) plane is a little tilted to the Si (111) plane. Top AlGaN layer peak is around 35 °and the peak close to 34.6 °is the AlGaN in the buffer layer. The peak at 36.1 °correspond to the AlN in the buffer layer.

4.2 Rocking Curve and Dislocation Density (DD) Calculation

6 rocking curves of 6 different Chi angle planes are measured for each sample. The rocking curve of HEMT C (002) plane is shown in Figure 4-8 and the other 35 rocking curves figure will not be illustrated here.

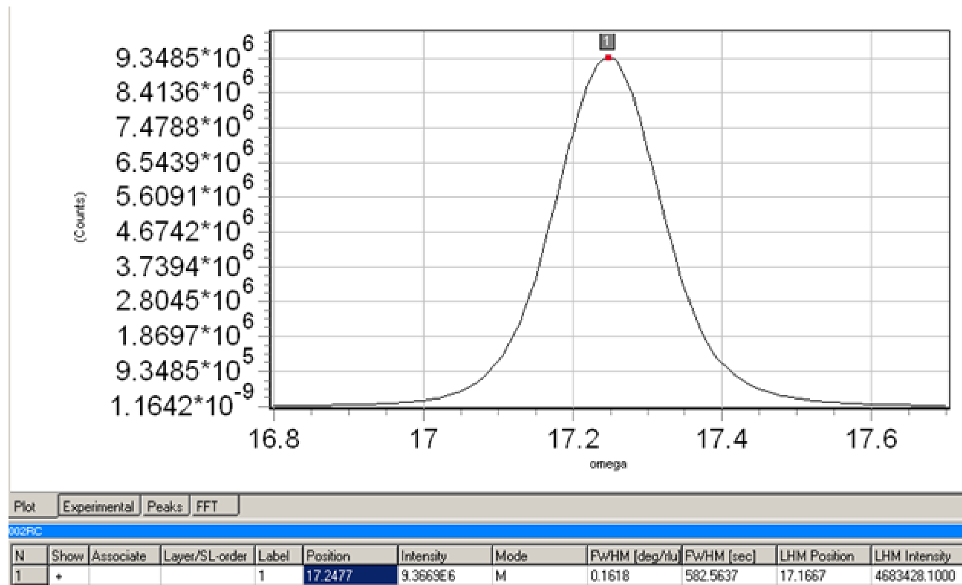

FIG. 4-8 Rocking curve of HEMT C 002 plane

36 FWHM values with different Chi angles are listed as shown in Table 4-1. The Software applied here is Origin. Figure 4-9 shows the plot of these data.

Table 4-1 FWHM values for different Chi angles

Chi degree	FWHM arcsec					
	Green led	HEMT B	HEMT D	HEMT C	GaN A	HEMT A
0	351.3	762.12	695.95	581	300.22	348.54
20.32	378.2	932.74	746.45	625	318.51	548.04
31.26	405.2	1108	882.32	609	321.23	712.8
42.76	402.5	1296.3	990.81	666.67	328.28	905.59
61.72	465.6	1339.1	995.22	688	373.71	1076.845
74.7	490	1598.44	1148.68	721	384.43	1181.58

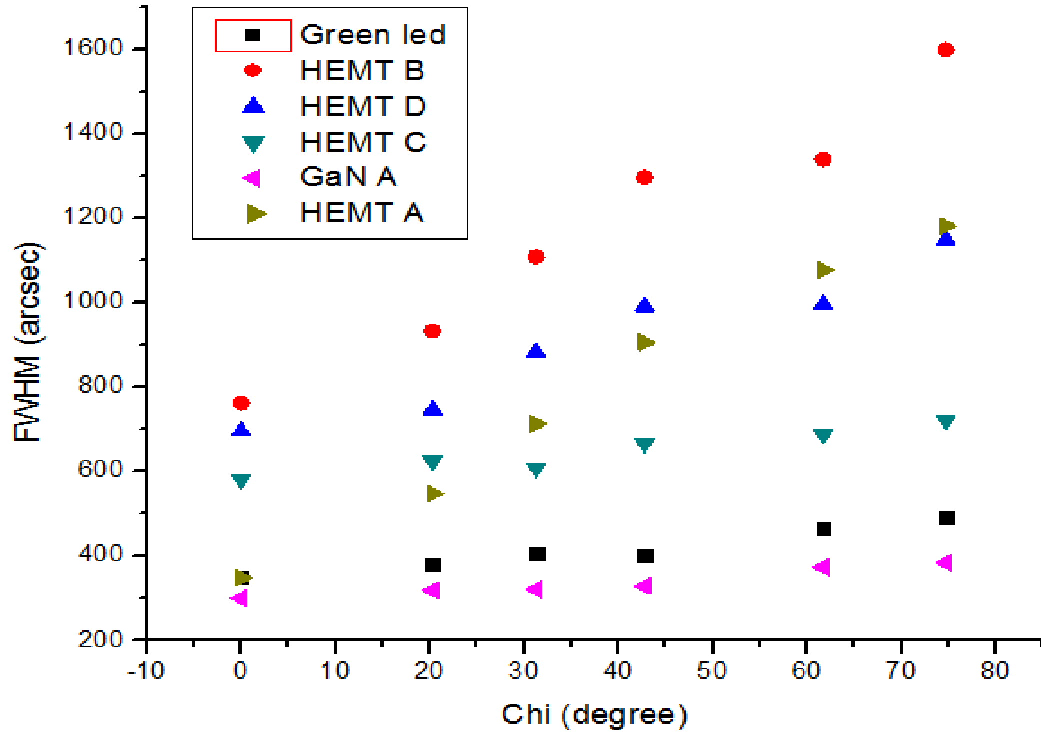

FIG. 4-9 FWHM plotted against Chi by Origin

A monotonic increase of FWHM is observed for each sample. Same trend is noticed for HEMT B and HEMT D indicating they have a similar buffer layer structure. HEMT B has the highest (002) and (201) FWHM, which means the highest screw DD and edge DD, while the best crystalline quality is obtained from GaN A.

Interestingly, HEMT A (002) FWHM is found around only 350 *arcsec* which is almost the same as Green LED. However, a much higher edge DD in HEMT A indicates a huge in plane misorientation and they are more sensible to planes with larger inclination angle.

A comparison of 2 inch HEMT A and HEMT C is made in Figure 4-10. A better rocking curve of symmetric plane is observed in HEMT A meaning a less screw DD for

HEMT on sapphire. However a much higher edge DD shows that without buffer layer, GaN on sapphire will have huge in-plane misorientation.

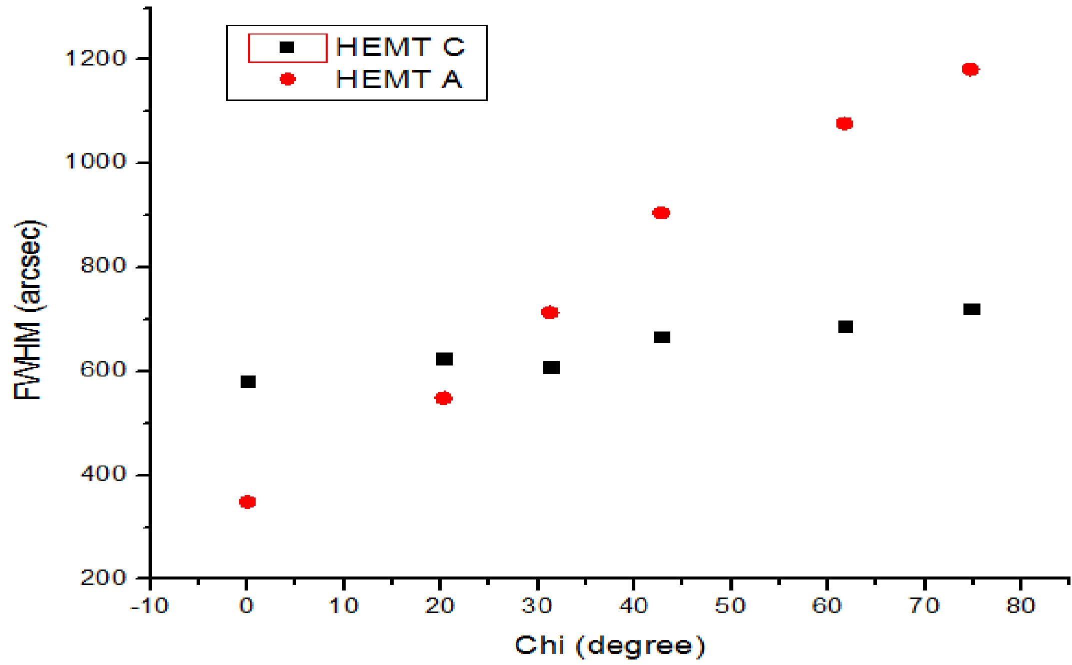

FIG. 4-10 Comparison of 2 inch HEMT on different substrate

Linear fit by Origin is applied to each sample. After extrapolating the fit line and intersect with Chi=90°, the in-plane twist is obtained. A more accurate way to get the twist value is to calculate it by adding $90\times slope$ to the tilt value. We can read the slope value from the linear fit result.

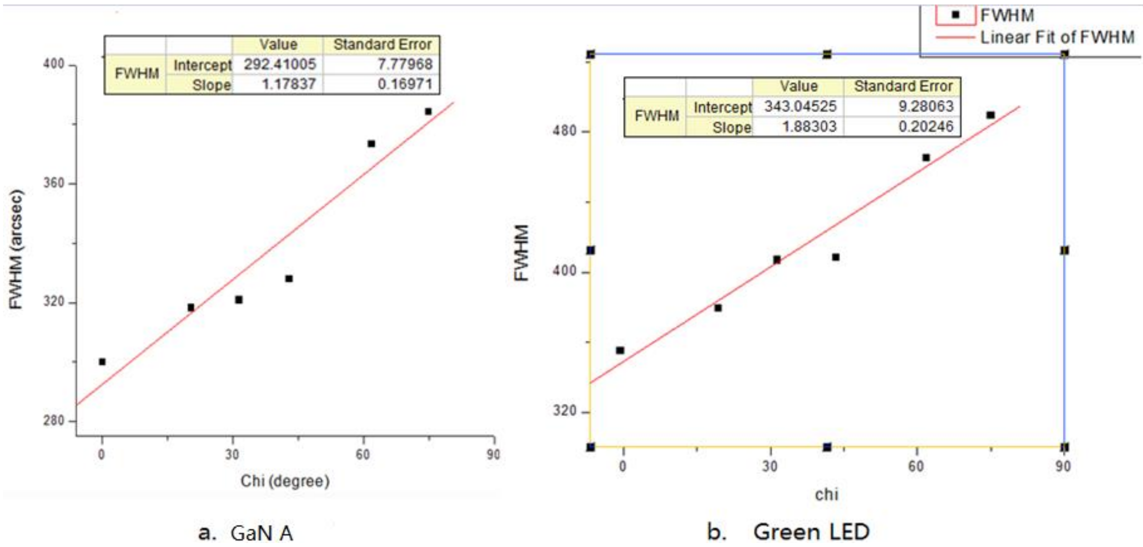

FIG. 4-11 Linear fit of: (a) GaN A (b) Green LED

As shown in Figure 4-11 (a), The fitted slope for GaN A is 1.18 and

Twist: (100) FWHM=292.4+1.18*90 = 398.6 *arcsec*

Tilt: (002) FWHM= 300.2 *arcsec*.

Based on equation 2-44,

$$\rho_{edge} = \frac{\Delta\omega_e^2}{4.35 b_e^2} = 8.44\times10^8 / cm^2$$

$$\rho_{screw} = \frac{\Delta\omega_s^2}{4.35 b_s^2} = 1.81\times10^8 / cm^2 .$$

As shown in Figure 4-11 (b), the fitted slope for Green LED is 1.88 and

Twist: (100) FWHM=351.3+1.88*90 = 520.5 *arcsec*

Tilt: (002) FWHM= 351.3 *arcsec*

ρ_e=1.44×10^9/cm^2

ρ_s=2.48×10^8/cm^2.

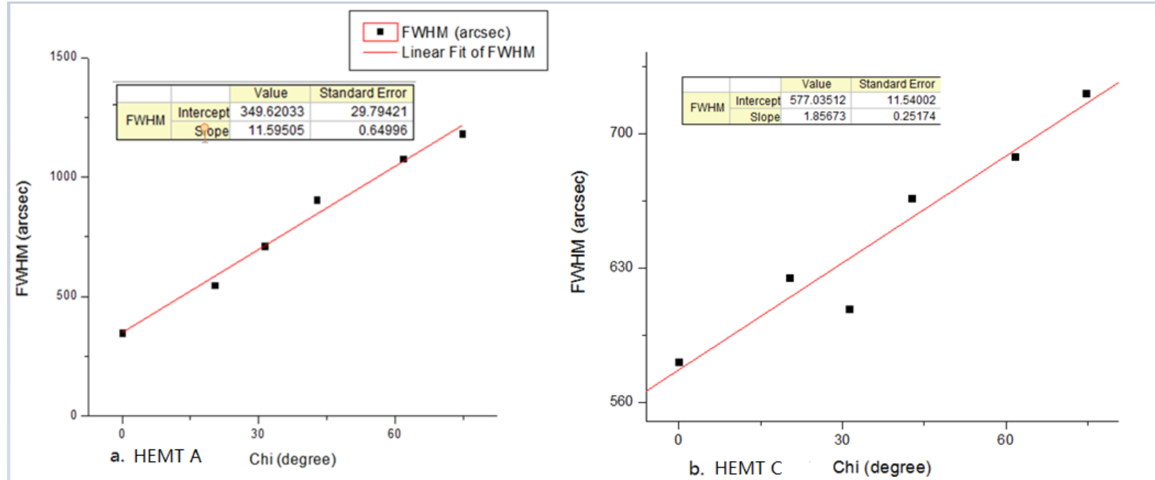

FIG. 4-12 Linear fit of : (a)HEMT A (b)HEMT C

As shown in Figure 4-12 (a), the fitted slope for HEMT A is 11.6 and

Twist: (100) FWHM=348.54+11.6*90 = 1392.54 *arcsec*

Tilt: (002) FWHM= 348.54 *arcsec*

$\rho_e=1.02\times10^{10}/cm^2$

$\rho_s=2.44\times10^{8}/cm^2$.

As shown in Figure 4-12 b, the fitted slope for HEMT C is 1.86 and

Twist: (100) FWHM=581+1.86*90 = 748.1 *arcsec*

Tilt: (002) FWHM= 581 *arcsec*

$\rho_e=2.97\times10^{9}/cm^2$

$\rho_s=6.78\times10^{8}/cm^2$.

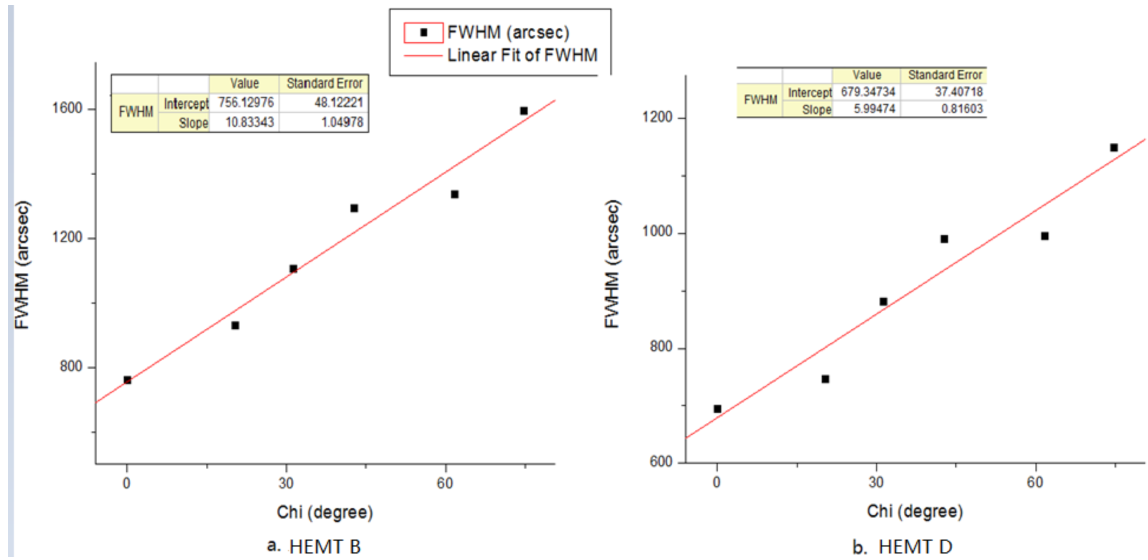

FIG. 4-13 Linear fit of (a) HEMT B (b) HEMT D

As shown in Figure 4-13 (a), the fitted slope for HEMT B is 10.83 and

Twist: (100) FWHM=762.1+10.83*90 = 1736.8 arcsec

Tilt: (002) FWHM= 762.1 arcsec

$\rho_e = 1.60 \times 10^{10}/cm^2$

$\rho_s = 1.17 \times 10^9/cm^2$.

As shown in Figure 4-13 (b), the fitted slope for HEMT D is 6.00 and

Twist: (100) FWHM=695.95+6*90 = 1236 *arcsec*

Tilt: (002) FWHM= 695.95 *arcsec*

$\rho_e = 8.12 \times 10^9/cm^2$

$\rho_s = 9.73 \times 10^8/cm^2$.

Table 4-2 combined all the data together and a ratio of $\frac{\rho_{edge}}{\rho_{screw}}$ is shown.

Table. 4-2 Concluded data of DD calculation

A	B	C	D	E	F	G	H
Plane	Chi(o)	FWHM (arcsec)					
		Greenled	HEMT B	HEMT D	HEMT C	GaN A	HEMT A
(0 0 2) tilt	0	351.3	762.12	695.95	581	300.22	348.54
(1 0 5)	20.32	378.2	932.74	746.45	625	318.51	548.04
(1 0 3)	31.26	405.2	1108	882.32	609	321.23	712.8
(1 0 2)	42.76	402.5	1296.3	990.81	666.7	328.28	905.59
(1 0 1)	61.72	465.6	1339.1	995.22	688	373.71	1076.845
(2 0 1)	74.7	490	1598.44	1148.68	721	384.43	1181.58
(1 0 0) twist	90	510	1736.8	1236	748.1	398.6	1392.54
Dscrew (/cm2)		2.48E+08	1.17E+09	9.73E+08	6.78E+08	1.81E+08	2.44E+08
Dedge (/cm2)		1.38E+09	1.6E+10	8.12E+09	2.97E+09	8.44E+08	1.03E+10
ratio		5.571505	13.72908	8.338143	4.382839	4.659978	42.19865

We can conclude form this table that

(1) Size effect: 6 inch epitaxial HEMT B has the highest DD.

(2) Buffer layer effect: A 42 times higher edge DD is observed in HEMT A and 4.4 times higher edge DD in found in HEMT C.

(3) Substrate effect: GaN A has smaller DD than HEMT C.

(4) The range of DD is from 10^8 to 10^{10} and this high of DD always coincides with a relaxation in RSM.

4.3 RSM

Figure 4-14 shows HEMT A RSM of a: (104) asymmetric plane b: (002) symmetric plane. A fully relaxed line is drawn in Figure (a) by drawing a line from origin to the diffraction peak point. The white ellipse stand for the AlGaN (104) diffraction and lie on the fully relaxed line. The relaxation degree for HEMT A is 1.

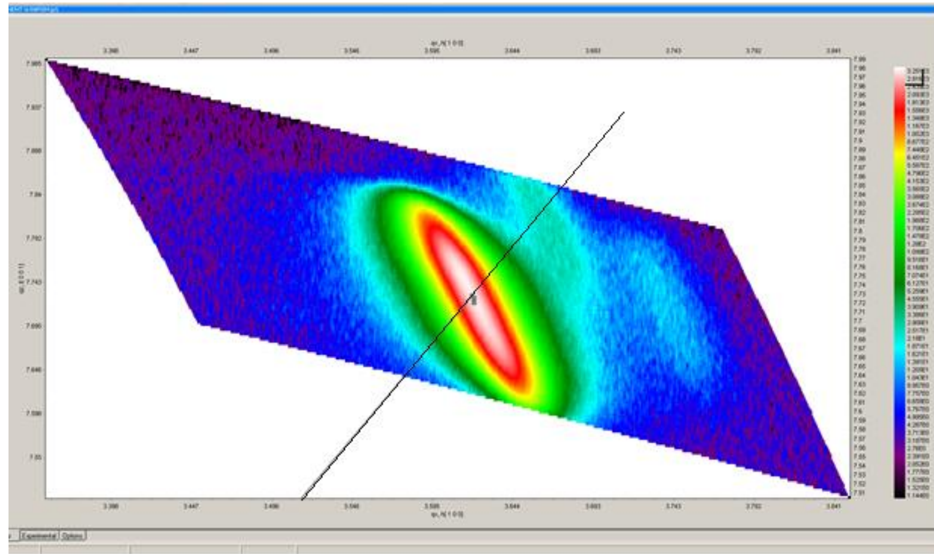

a. (104) RSM

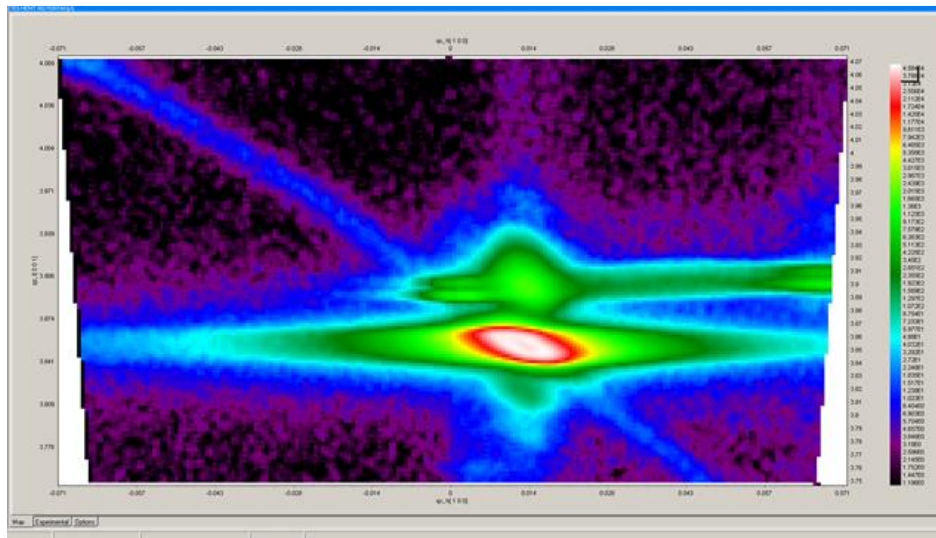

b. (002) RSM

FIG. 4-14 RSM of HEMT A (a) 104 (b) 002

Figure 4-15 shows HEMT B RSM of a: (104) asymmetric b: (002) symmetric. A fully relaxed line is drawn in figure a. As we can see, the diffraction ellipse of AlGaN with

different compositions in (002) RSM merged together in (104) RSM and form a green strip lied on the fully relaxed line. The relaxation degree for HEMT B is also 1.

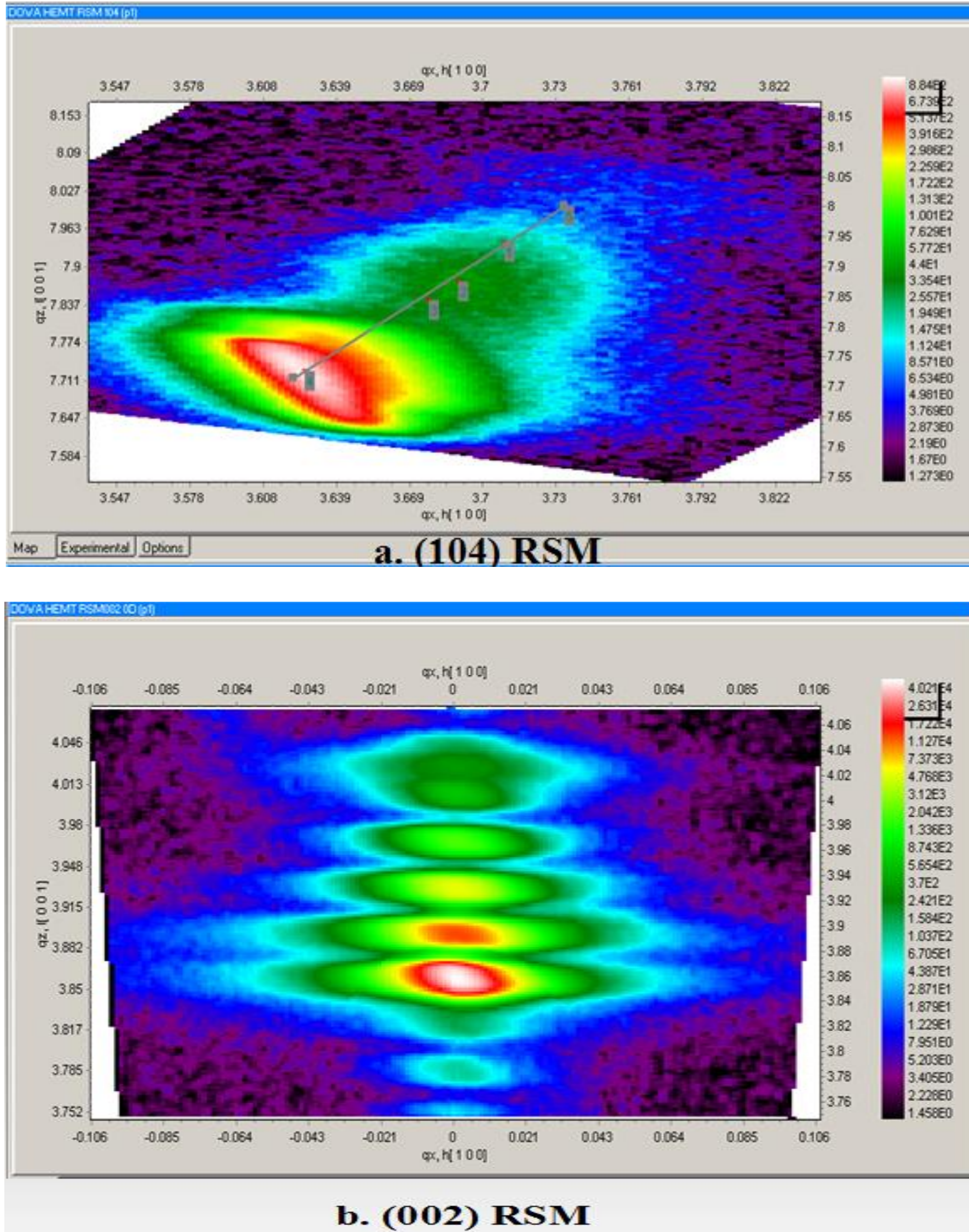

FIG 4-15 RSM of HEMT B (a) 104 (b) 002

Figure 4-16 shows HEMT C RSM of a: (104) asymmetric b: (002) symmetric. A fully relaxed line is drawn in figure a, the dark green ellipse stands for the AlGaN (104)

diffraction while the light blue ellipse stands for the AlN (104) diffraction. GaN and AlGaN layers are slightly off the fully relaxed line. The relaxation degree for HEMT C is considered as 1.

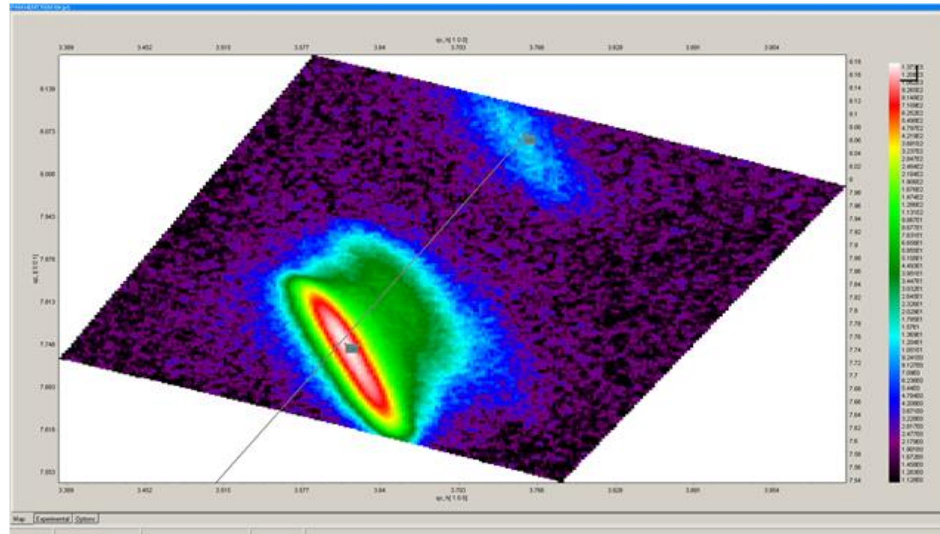

a. (104) RSM

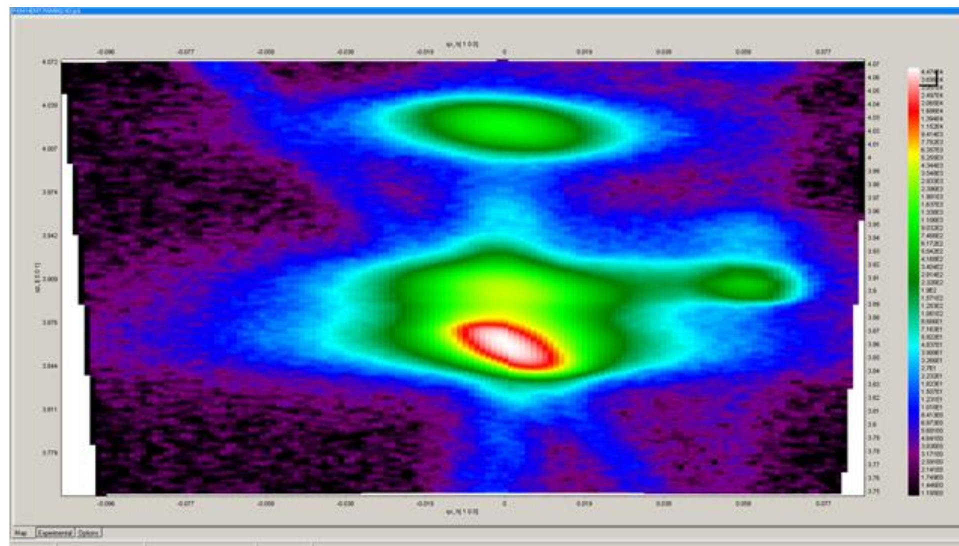

b. (002) RSM

FIG. 4-16 RSM of HEMT C (a) 104 (b) 002

Figure 4-17 shows HEMT D RSM of a: (104) asymmetric b: (002) symmetric. A fully relaxed line is drawn in figure a. As we can see, the diffraction ellipse of AlGaN with different compositions in (002) RSM merged together in (104) RSM and form a green strip lied on the fully relaxed line. The relaxation degree for HEMT D is 1.

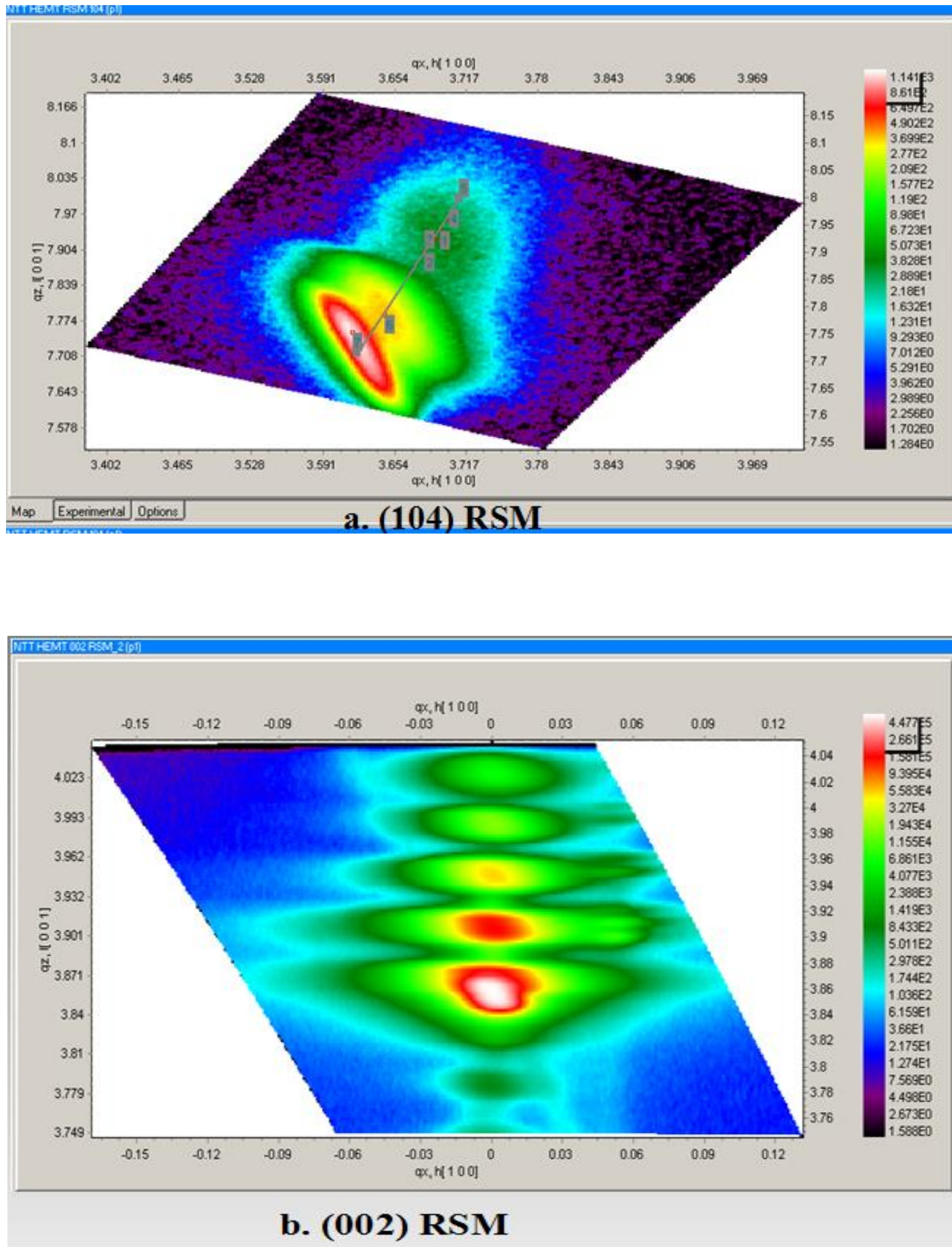

FIG 4-17 RSM of HEMT D (a) 104 (b) 002

Figure 4-18 shows Green LED RSM of a: (104) asymmetric b: (002) symmetric. Based on the geometry shown in Figure 2-30, relaxation lines are drawn by the equation $\tan\alpha = \tan\tau / D$, where D=0.533 for GaN, and D for InGaN with low *In* composition doesn't change much. The relaxation degree for Green LED is estimated as 0.9.

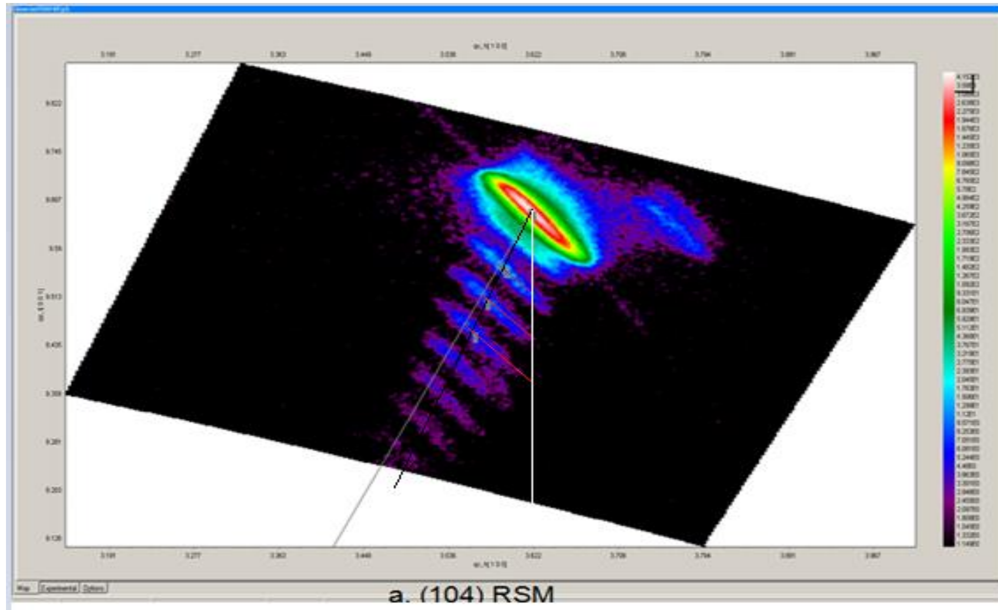

a. (104) RSM

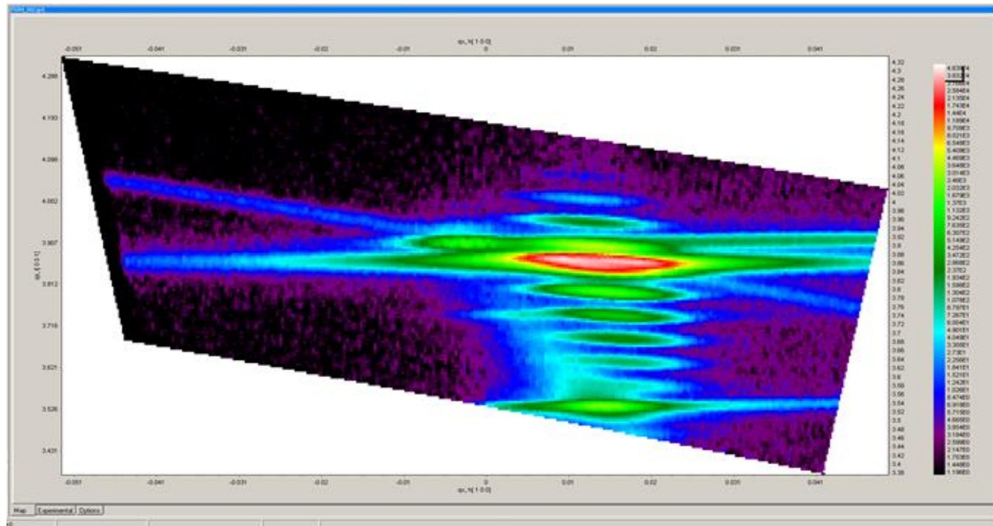

b. (002) RSM

FIG. 4-18 RSM of Green LED (a) 104 (b) 002

4.4 Composition Simulation by XRD

Simulations are run by LEPTOZ on 4 HEMT samples and Green LED. The relaxation degree is set as 1 for all 4 HEMT samples and 0.9 for Green LED.

Figure 4-19 shows the simulation result of HEMT A, a 25nm $Al_{0.33}Ga_{0.67}N$ layer is achieved. As we can see, no buffer layer is observe and GaN is directly grown on sapphire in HEMT A.

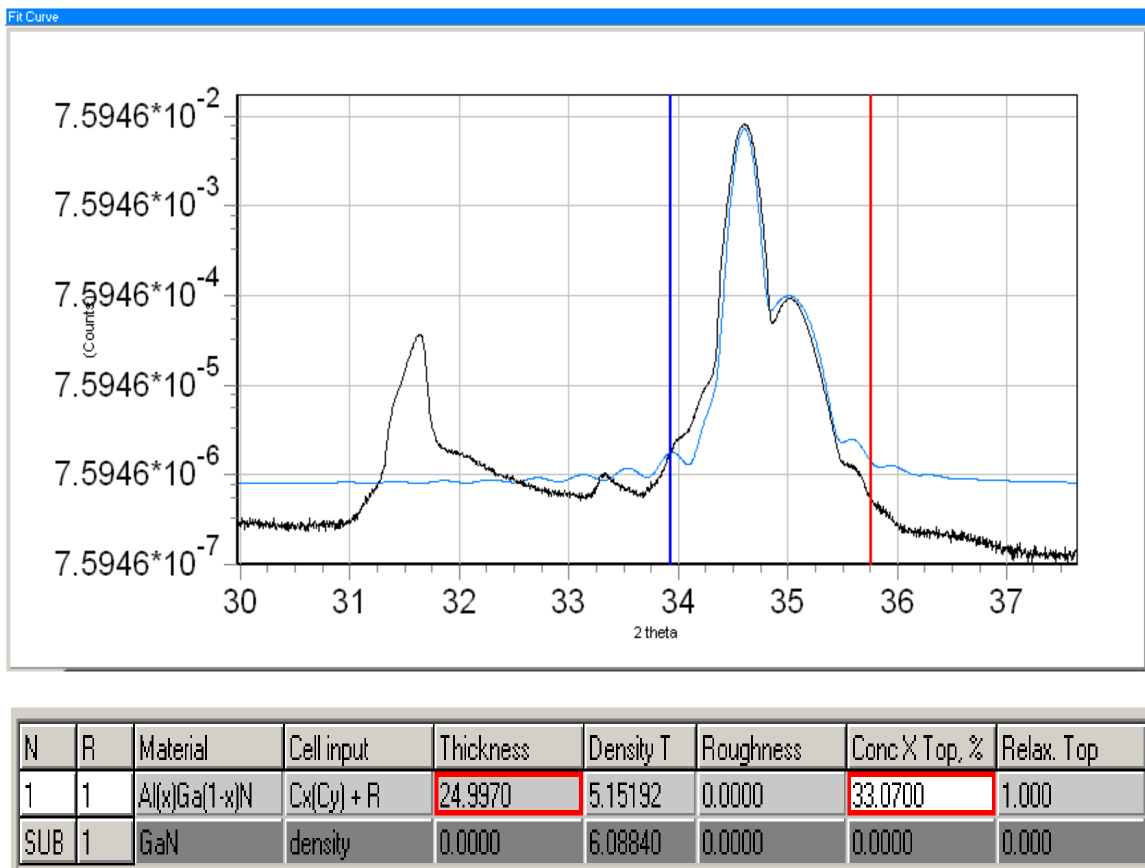

N	R	Material	Cell input	Thickness	Density T	Roughness	Conc X Top, %	Relax. Top
1	1	Al(x)Ga(1-x)N	Cx(Cy) + R	24.9970	5.15192	0.0000	33.0700	1.000
SUB	1	GaN	density	0.0000	6.08840	0.0000	0.0000	0.000

FIG. 4-19 Simulation result of HEMT A

Figure 4-20 shows the simulation result of HEMT B, $Al_{0.24}Ga_{0.76}N$ is deposited on GaN and the buffer layer consists of AlN, $Al_{0.72}Ga_{0.28}N$, $Al_{0.48}Ga_{0.52}N$. The thickness information is not reliable.

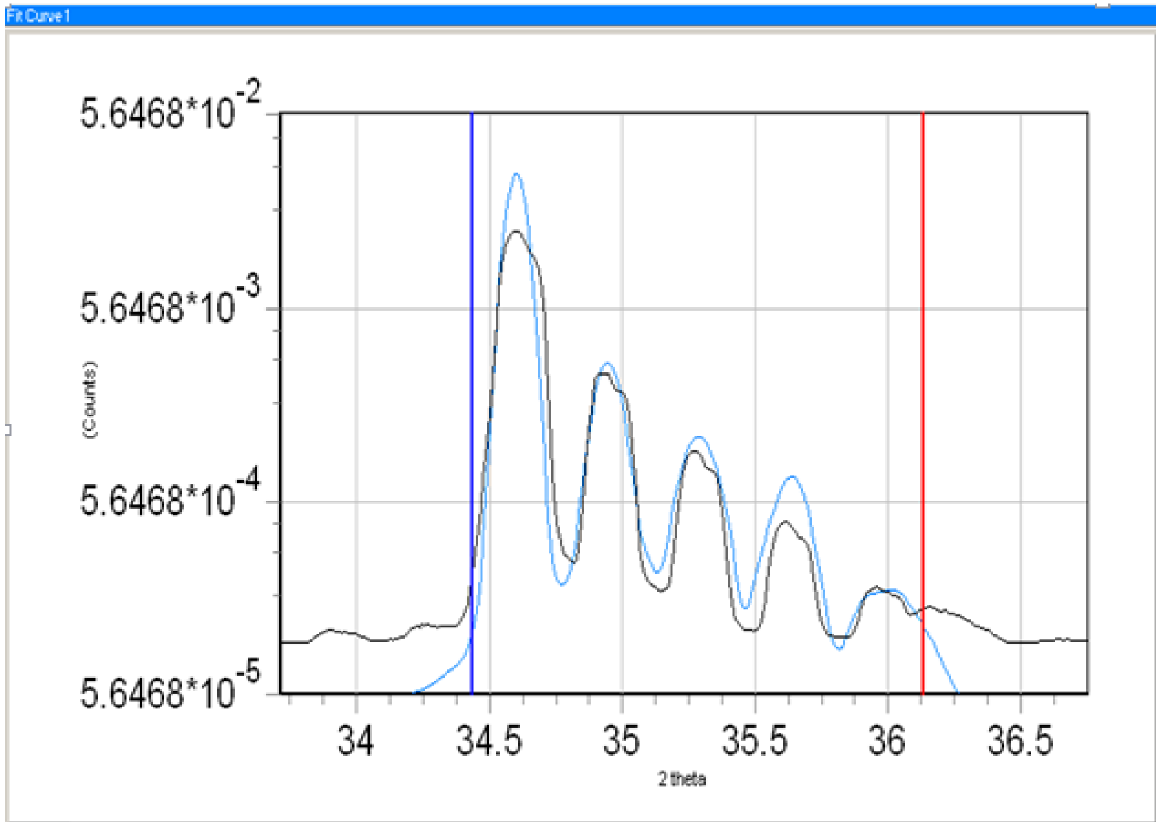

N	R	Material	Cell input	Thickness	Density T	Conc X Top, %	Density B	Relax. Bot
1	1	Al(x)Ga(1-x)N	Cx(Cy) + R	86.3551	5.40575	24.1070	5.40575	1.000
2	1	Al(x)Ga(1-x)N	Cx(Cy) + R	59.4354	4.71706	48.4260	4.71706	1.000
3	1	Al(x)Ga(1-x)N	Cx(Cy) + R	53.1446	4.05222	71.9040	4.05222	1.000
4	1	AlN	R	30.0623	3.25660	0.0000	3.25660	1.000
SUB	1	GaN	density	0.0000	6.08840	0.0000	6.08840	0.000

FIG. 4-20 Simulation result of HEMT B

Figure 4-21 shows the simulation result of HEMT C, top $Al_{0.26}Ga_{0.74}N$ layer and buffer layer made of AlN and $Al_{0.11}Ga_{0.89}N$ is achieved. The thickness information is not reliable cause the fringes are not fit.

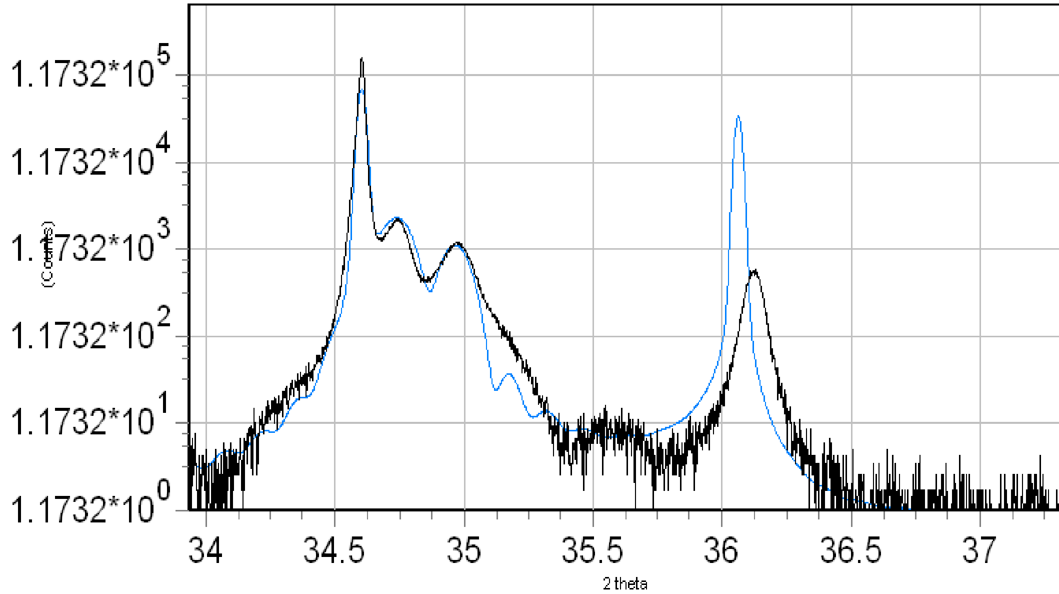

N	R	Material	Cell input	Thickness	Density T	Conc X Top, %	Relax. Top
1	1	Al(x)Ga(1-x)N	Cx(Cy) + R	65.0000	5.34520	26.2450	1.000
2	1	GaN	R	1895.4955	6.08840	0.0000	1.000
3	1	Al(x)Ga(1-x)N	Cx(Cy) + R	65.0000	5.76941	11.2640	1.000
SUB	1	AlN	density	0.0000	3.25660	0.0000	0.000

FIG. 4-21 Simulation result of HEMT C

Figure 4-22 shows the simulation result of HEMT D, $Al_{0.33}Ga_{0.67}N$ is deposited on GaN and the buffer layer consists of AlN, $Al_{0.88}Ga_{0.12}N$, $Al_{0.59}Ga_{0.41}N$. The thickness information is not reliable.

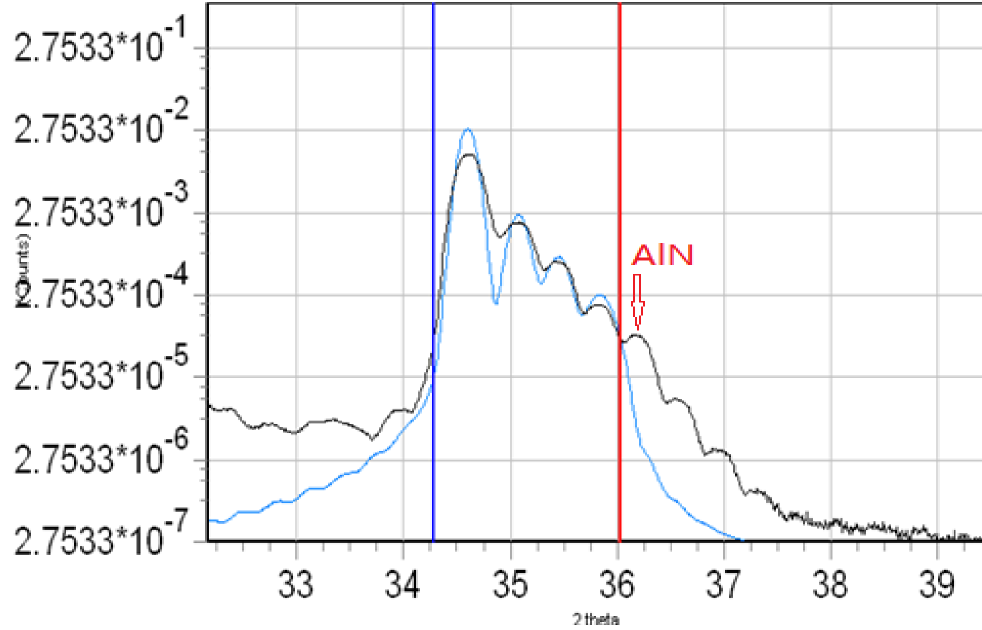

N	R	Material	Cell input	Thickness	Density T	Conc X Top, %	Relax. Top	Density B	Relax. Bot
1	1	Al(x)Ga(1-x)N	Cx(Cy) + R	97.6784	5.14888	33.1770	1.000	5.14888	1.000
2	1	Al(x)Ga(1-x)N	Cx(Cy) + R	49.9869	4.40601	59.4100	1.000	4.40601	1.000
3	1	Al(x)Ga(1-x)N	Cx(Cy) + R	34.1210	3.58888	88.2660	1.000	3.58888	1.000
SUB	1	GaN	density	0.0000	6.08840	0.0000	0.000	6.08840	0.000

FIG. 4-22 Simulation result of HEMT D

Figure 4-23 shows the simulation result of Green LED. The simulation ends up with 5 period of GaN/$In_{0.32}Ga_{0.68}N$ with thickness 16.2 and 2.5nm respectively. The simulation result is quite reliable because the bandgap of $In_{0.32}Ga_{0.68}N$ lies exactly in the range of green light wavelength. [21]

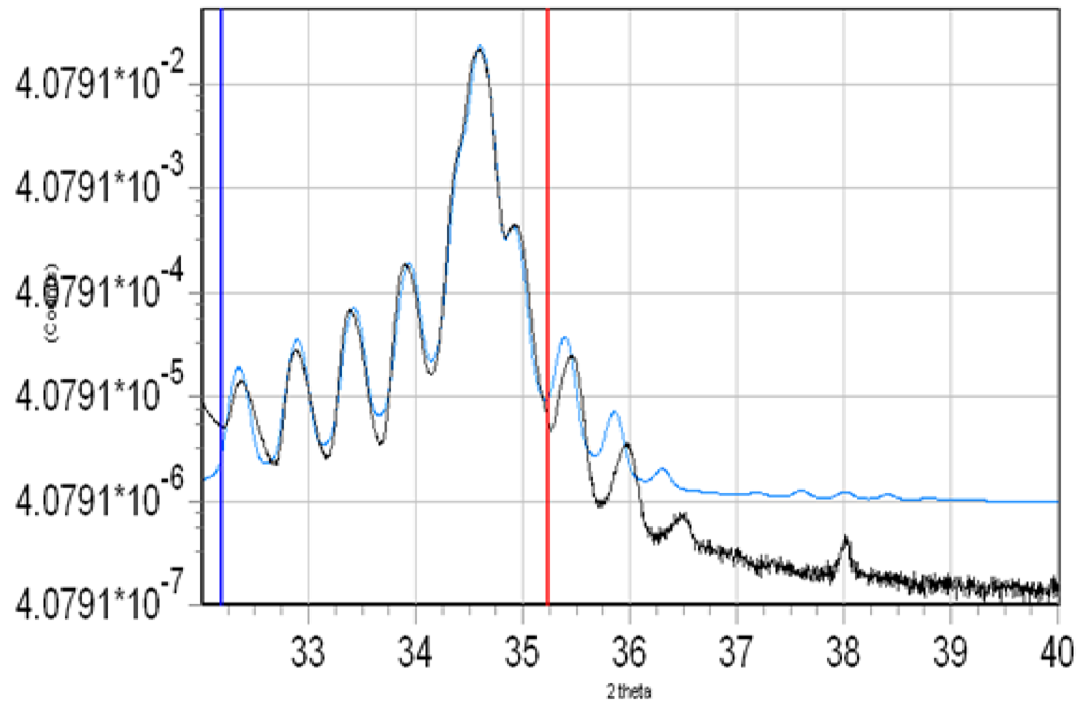

N	R	Material	Cell input	Thickness	Density T	Roughness	Conc X Top, %	Relax. Top
1	1	GaN	R	160.1784	6.08840	0.0000	0.0000	0.900
2	5	Ga(1-x)In(x)N	Cx(Cy) + R	2.4614	6.35600	0.0000	32.2250	0.900
3	5	GaN	R	16.2386	6.08840	0.0000	0.0000	0.900
SUB	1	GaN	density	0.0000	6.08840	0.0000	0.0000	0.000

FIG. 4-23 Simulation result of Green LED from -3 to +1 satellite peaks

In conclusion, by XRD simulation, only HEMT A is found with no AlN buffer layer. GaN is directly deposited on sapphire. This difference is also the main reason for extremely high in-plane misorientations, and edge dislocations found in 2 inch HEMT A as we discussed in section 4.2.

4.5 Simulation by XRR

Figure 4-24 shows the XRR simulation of HEMT A, a 34 nm $Al_{0.22}Ga_{0.78}N$ layer and a 3nm GaN cap are achieved. The roughness between the AlGaN/GaN interface is around 0.9 nm.

Figure 4-25 shows the XRR simulation of HEMT B, a 19nm $Al_{0.36}Ga_{0.64}N$ layer and a 1nm GaN cap are achieved. The roughness between the AlGaN/GaN interface is nearly 0.

Figure 4-26 shows the XRR simulation of HEMT C, a 22nm $Al_{0.34}Ga_{0.66}N$ layer and a 2nm GaN cap are achieved. The roughness between the AlGaN/GaN interface is around 0.4 nm.

Figure 4-27 shows the XRR simulation of HEMT D, a 21nm $Al_{0.3}Ga_{0.7}N$ layer and a 2nm GaN cap are achieved. The roughness between the AlGaN/GaN interface is nearly 0.

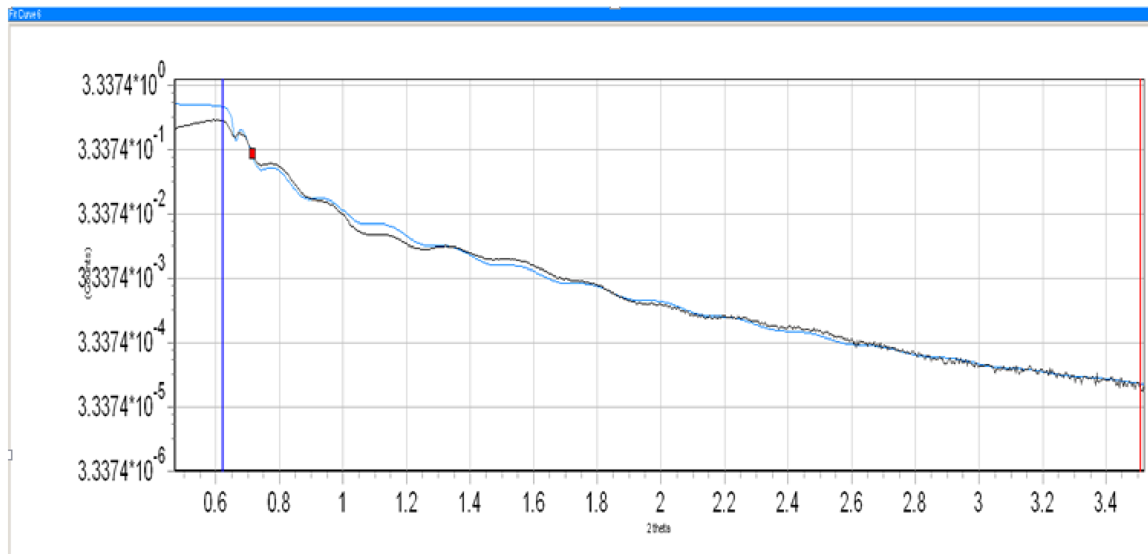

N	R	Material	Cell input	Thickness	Density T	Roughness	Conc X Top, %	Relax. Top
1	1	GaN	R	2.7878	6.08840	0.4031	0.0000	0.000
2	1	Al(x)Ga(1-x)N	density	34.3656	5.46566	0.6845	21.9910	0.000
3	1	GaN	R	209.1145	6.08840	0.8790	0.0000	0.000
SUB	1	GaN	density	0.0000	6.08840	0.8551	0.0000	0.000

FIG. 4-24 XRR Simulation result of HEMT A

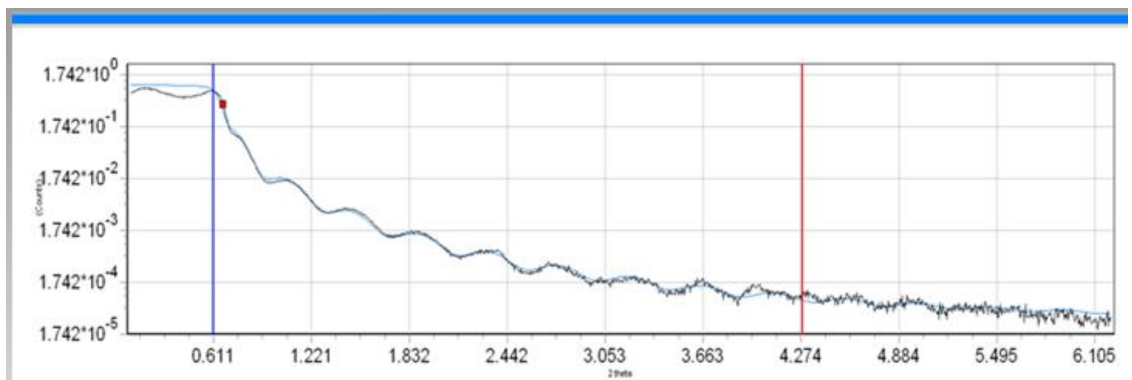

N	R	Material	Cell input	Thickness	Density T	Roughness	Conc X Top, %	Relax. Top	Density B	Conc X Bot, %
1	1	GaN	density	0.8227	6.08840	0.0000	0.0000	0.000	6.08840	0.0000
2	1	Al(x)Ga(1-x)N	Cx(Cy) + R	18.7183	5.07986	0.2916	35.6150	0.000	5.07986	35.6150
3	1	GaN	R	296.5624	6.08840	0.0000	0.0000	0.000	6.08840	0.0000
4	1	Al(x)Ga(1-x)N	density	3000.0000	4.98183	0.0000	39.0760	0.000	4.98183	39.0760
SUB	1	Si	density	0.0000	2.32910	0.0000	0.0000	0.000	2.32910	0.0000

FIG. 4-25 XRR Simulation result of HEMT B

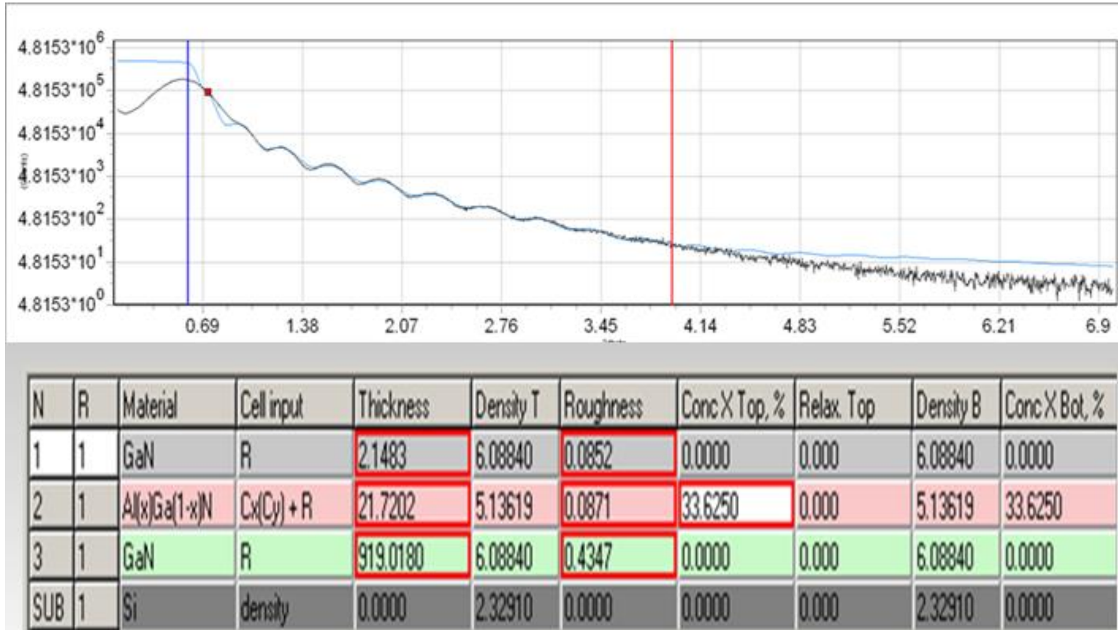

N	R	Material	Cell input	Thickness	Density T	Roughness	Conc X Top, %	Relax. Top	Density B	Conc X Bot, %
1	1	GaN	R	2.1483	6.08840	0.0852	0.0000	0.000	6.08840	0.0000
2	1	Al(x)Ga(1-x)N	Cx(Cy) + R	21.7202	5.13619	0.0871	33.6250	0.000	5.13619	33.6250
3	1	GaN	R	919.0180	6.08840	0.4347	0.0000	0.000	6.08840	0.0000
SUB	1	Si	density	0.0000	2.32910	0.0000	0.0000	0.000	2.32910	0.0000

FIG. 4-26 XRR Simulation result of HEMT C

N	R	Material	Cell input	Thickness	Density T	Roughness	Conc X Top, %	Relax. Top	Density B	Conc X Bot, %
1	1	GaN	density	1.9457	6.69606	0.2760	0.0000	0.000	6.69606	0.0000
2	1	Al(x)Ga(1-x)N	Cx(Cy) + R	20.6610	5.23633	0.3691	30.0890	0.000	5.23633	30.0890
3	1	GaN	R	141.1949	6.08840	0.0000	0.0000	0.000	6.08840	0.0000
SUB	1	Si	density	0.0000	2.32910	0.0000	0.0000	0.000	2.32910	0.0000

FIG. 4-27 XRR Simulation result of HEMT D

4.6 Comparison of XRD Simulation and XRR Simulation

The XRD simulation result of HEMT A is compared with XRR simulation, shown in Table 4-3. The top one is XRD simulation while the bottom one is XRR simulation.

Table 4-3 XRD simulation compared with XRR simulation of HEMT A

N	R	Material	Cell input	Thickness	Density T	Roughness	Conc X Top, %	Relax. Top
1	1	Al(x)Ga(1-x)N	Cx(Cy) + R	24.9970	5.15192	0.0000	33.0700	1.000
SUB	1	GaN	density	0.0000	6.08840	0.0000	0.0000	0.000

N	R	Material	Cell input	Thickness	Density T	Roughness	Conc X Top, %	Relax. Top
1	1	GaN	R	2.7878	6.08840	0.4031	0.0000	0.000
2	1	Al(x)Ga(1-x)N	density	34.3656	5.46566	0.6845	21.9910	0.000
3	1	GaN	R	209.1145	6.08840	0.8790	0.0000	0.000
SUB	1	GaN	density	0.0000	6.08840	0.8551	0.0000	0.000

As we can see here XRD and XRR simulation are not perfectly consistent with each other. Usually we take the composition result from XRD simulation and thickness result from XRR simulation. Then we end up with our final simulation results and they are illustrated by schematic drawing in next chapter.

5. SUMMARY

1. (002) single crystalline wurtzite GaN is observed in every sample.

2. 6 inch sample HEMT B has the highest threading DD.

3. GaN A with AlGaN buffer layer has the best crystal quality in GaN layer.

4. HEMT A has huge in-plane misorientation due to directly grow without buffer layer.

5. AlGaN buffer layers are characterized for the other HEMTs.

6. $In_{0.32}Ga_{0.68}N$/GaN supperlattice structure is observed in Green LED, with thickness 16.2 nm and 2.5nm.

7. Top AlGaN layers and GaN cap are characterized by XRR.

Based on the characterization result, the schematic structures of 4 different HEMTs are shown in Figure 4-28, 4-29, 4-30 and 4-31.

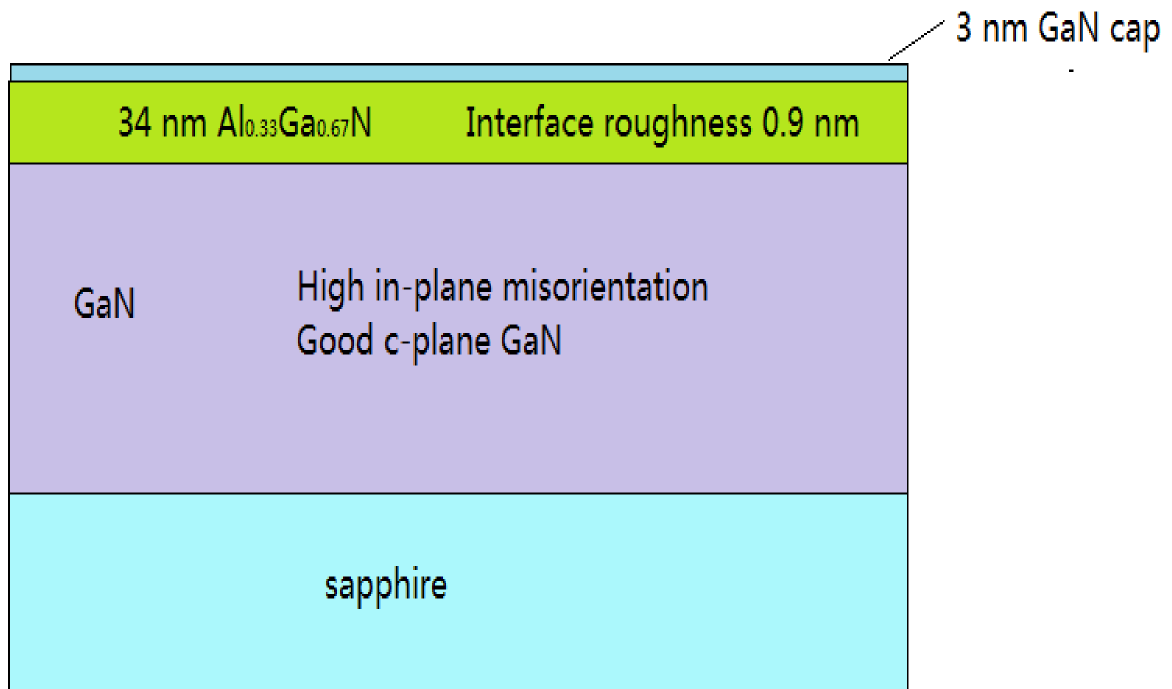

FIG. 5-1 Schematic structure of HEMT A

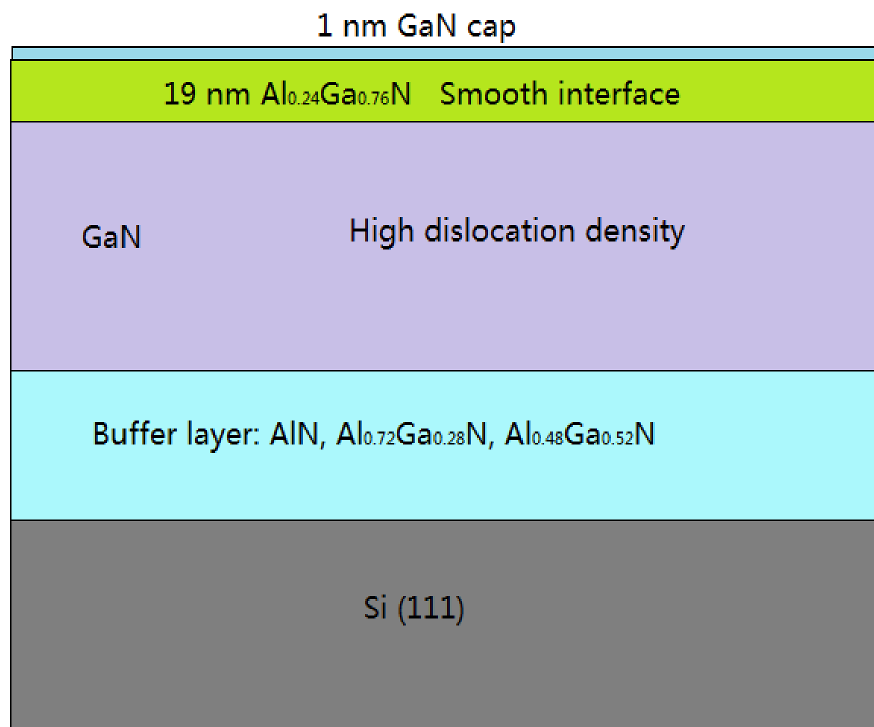

FIG. 5-2 Schematic structure of HEMT B

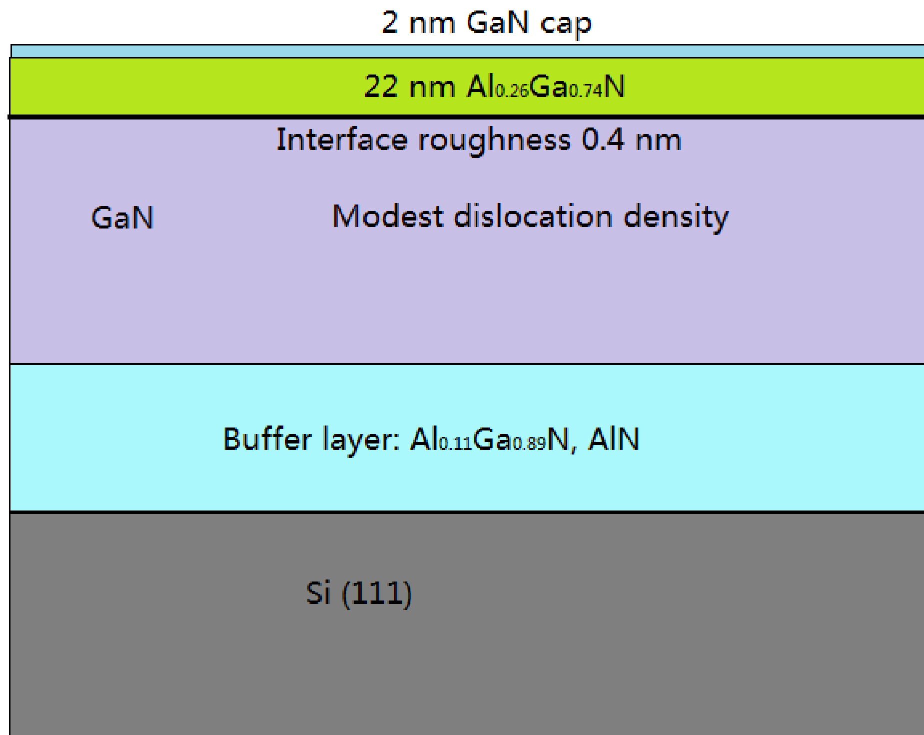

FIG. 5-3 Schematic structure of HEMT C

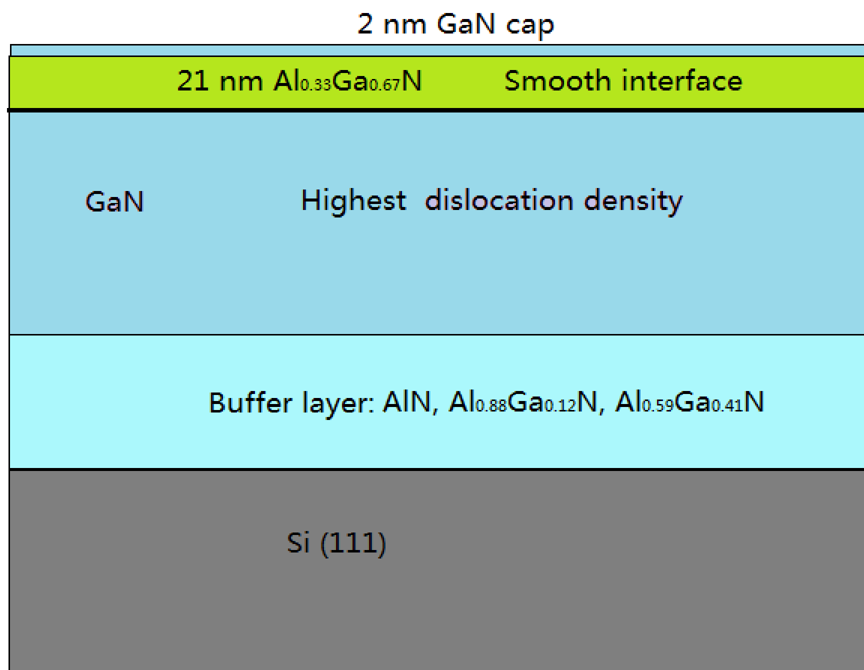

FIG. 5-4 Schematic structure of HEMT D

In this thesis, x-ray techniques are employed for structural characterization of GaN-based LEDs and HEMTs including:

1. Symmetric θ/2θ scan for buffer and MQW structures.
2. Rocking curves for threading dislocation density.
3. Reciprocal space map for strain status.
4. X-ray reflectivity for surface layer thickness and roughness.

It can be concluded that x-ray techniques can provide precise and reliable structural characterization. They are powerful tools for materials characterization and optimization for III-N-based solid-state lighting and power electronics.

Reference:

[1] G.E. Moore, Electronics, 38, 114–7, 1965.

[2] David Williams, Andrew Clark, F. Erdem Arkun and Rytis Dargis, “Perfecting GaN-On-Silicon Power Electronics,” *PEW*, October 2014.

[3] Jae Kyeong Jeong, Hyun Jin Kim, Hui-Chan Seo, Hee Jin Kim, Euijoon Yoon, Cheol Seong Hwang, and Hyeong Joon Kim, “Improvement in the Crystalline Quality of Epitaxial GaN Films Grown by MOCVD by Adopting Porous 4H-SiC Substrate,” *Electrochemical and Solid-State Letters*, 7~(4), February 2004.

[4] B.D. Cullity, Elements of X-Ray Diffractions, Addison-Wesley publishing Company, Massachusetts, 1956.

[5] Jyun-Hao Lin, Shyh-Jer Huang, and Yan-Kuin Su, “Performance Improvement of GaN-Based Metal-Semiconductor-Metal Photodiodes Grown on Si(111) Substrate by Thermal Cycle Annealing Process,” *Japanese Journal of Applied Physics*, 53, 04EH08, 2014.

[6] Hongping Zhao, “Approaches for High Internal Quantum Efficiency Green InGaN Light-emitting Diodes with Large Overlap Quantum Wells,” *Optics Express*, Vol.19, No. S4, July 2011.

[7] P. R. Hageman, S. Haffouz, V. Kirilyuk, A. Grzegorczyk, and P. K. LarsenHigh, “Quality GaN Layers on Si(111) Substrates: AlN Buffer Layer Optimisation and Insertion of a SiN Intermediate Layer,” *phys.stat.sol*.(a) 188, No.2, 523–526, 2001.

[8] Mario Birkholz, Thin Film Analysis by X-Ray Scattering, WILEY-VCH Verlag GmbH & Co. KGaA, Weinheim, Germany, 2006.

[9] Takayuki Konya, “X-Ray Thin Film Measurement Techniques: High resolution X-ray diffractometry,” *Technical articles*, 2000

[10] SH Glenzer, R Redmer, "X-Ray Thomson Scattering In High Energy Density Plasmas," *Reviews of Modern Physics*, 81(4):1625-1663, 2009.

[11] J. F. Muth, J. H. Lee, I. K. Shmagin, R. M. Kolbas, H. C. Casey, "Absorption Coefficient, Energy Gap, Exciton Binding Energy, and Recombination Lifetime of GaN Obtained From Transmission Measurements," *Appl. Phys. Lett*., 71, 2572, 1997.

[12] N.V. Safriuk, G.V. Stanchu, A.V. Kuchuk, V.P. Kladko, A.E. Belyaev, V.F. Machulin, "X-Ray Diffraction Investigation of GaN Layers on Si(111) and Al_2O_3 (0001) Substrates," *Semiconductor Physics, Quantum Electronics & Optoelectronics*, V. 16, N 3, P. 265-272, 2013.

[13] YU Xin-Xin, NI Jin-Yu, LI Zhong-Hui, KONG Cen, ZHOU Jian-Jun, DONG Xun, PAN Lei, KONG Yue-Chan, CHEN Tang-Sheng, "AlGaN/GaN HEMTs on 4-Inch Silicon Substrates in the Presence of 2.7-μm-Thick Epilayers with the Maximum Off-State Breakdown Voltage of 500V," *CHIN. PHYS. LETT*, Vol. 31, No. 3, 2014.

[14] J. H. Hubbell and S. M. Seltzer, "Tables of X-Ray Mass Attenuation Coefficients and Mass Energy-Absorption Coefficients from 1 keV to 20 MeV for Elements Z = 1 to 92 and 48 Additional Substances of Dosimetric Interest," Radiation Physics Division, PML, NIST, 1989.

[15] Toru Mitsunaga, "X-Ray Thin-Film Measurement Techniques: Out-of-plane Diffraction Measurements," *Technical articles*, 2000.

[16] Shintaro Kobayashi, "X-Ray Thin-Film Measurement Techniques: In-plane XRD Measurement," *Technical articles*, 2000.

[17] J.E. Ayers, "The Measurement of Threading Dislocation Densities in Semiconductor Crystals by X-Ray Diffraction," *Journal of Crystal Growth*, 135, 1994.

[18] V. M. Kaganer, O. Brandt, A. Trampert, and K. H. Ploog, “X-Ray Diffraction Peak Profiles from Threading Dislocations in GaN Epitaxial Films,” *Phys. Rev. B*, Volume 72, Issue 4, July 2005.

[19] H. Heinke, V. Kirchner, S. Einfeldt, and D. Hommel, “X-Ray Diffraction Analysis of the Defect Structure in Epitaxial GaN,” *APPLIED PHYSICS LETTERS*, VOLUME 77, NUMBER 14, OCTOBER 2000.

[20] Miho Yasaka, X-Ray Thin-Film Measurement Techniques: X-ray reflectivity measurement, *Technical articles*, 2000.

[21] Takashi MUKAI, Motokazu YAMADA and Shuji NAKAMURA, “Characteristics of InGaN-Based UV/Blue/Green/Amber/Red Light-Emitting Diodes,” *Japan. J. Appl. Phys*, Vol. 38, 1999.